INAUGURAL – DISSERTATION

zur

Erlangung der Doktorwürde

der

Naturwissenschaftlich-Mathematischen

Gesamtfakultät

der

Ruprecht – Karls – Universität

Heidelberg

vorgelegt von

Diplom Hydrologe Steffen Holzkämper

aus Sinsheim

Tag der mündlichen Prüfung: 27. Februar 2004

Dating and Interpretation

of Secondary Carbonate Deposits

from the Last Interglacial

Gutachter: Prof. Dr. Augusto Mangini
Prof. Dr. Werner Aeschbach–Hertig

Zusammenfassung

In der vorliegenden Arbeit wurde das Alter von Kalksintern mittels der U/Th Datierungsmethode bestimmt und paläoklimatologisch interpretiert. Die Untersuchung von Höhlensintern der *Spannagel Höhle* (*Zillertaler Alpen*, Österreich) ergab, dass die letzte Warmzeit bereits vor ca. 135.000 Jahren (135 ka) begann. Die Unterbrechung des Sinterwachstums vor ca. 130 ka lässt eine kurzzeitige kühlere Phase vermuten, bevor vor 126 ka die eigentliche Warmzeit, das Eem, einsetzte. Nach zwei weiteren kürzeren Wachstumsunterbrechungen und einem Rückgang der Wachstumsrate der Höhlensinter ab ca. 118 ka endete das Sinterwachstum vollständig vor 116 ka. Dieser Zeitpunkt markiert das Ende der letzten Warmzeit. Demzufolge dauerte das klassische Eem ca. 10 ka, also in etwa so lange, wie unsere jetzige Warmzeit, das Holozän, bereits andauert. Ein weiterer Höhlensinter aus der *Spannagel–Höhle* entstand während verschiedener Warmzeiten der vergangenen 250 ka. Die Wachstumsphasen können nur teilweise mit hoher solaren Einstrahlung bei 60°N erklärt werden, die von vielen Paläo–Klimatologen als der Hauptantrieb für Warmzeiten angesehen wird. Eine bessere Übereinstimmung erzielt der Vergleich der Wachstumsphasen mit der aus Tiefseesedimenten rekonstruierten Magnetfeldstärke von Sonne und Erde, welche möglicherweise einen Einfluss auf die Wolkenbildung haben. Frequenzanalysen weisen darauf hin, dass die Zyklen der Sonnen–Aktivität einen Einfluss auf das Klima des Eem hatten, denn Zyklen mit ähnlicher Frequenz konnten im $\delta^{18}O$–Profil eines Stalagmiten nachgewiesen werden. Längere Periodizitäten, die im Isotopenprofil eines Flowstones nachgewiesen wurden, weisen auf einen Zusammenhang zwischen der Strömung des Nord–Atlantik und dem mitteleuropäischen Klima hin. Die sogenannten *DANSGAARD/OESCHGER–Zyklen* mit der Periodizität von 1470 Jahren hinterließen nicht nur in atlantischen Tiefseesedimenten und im Grönländischen Eis ihre Spuren, sondern auch in den $\delta^{18}O$ und $\delta^{13}C$ Profilen alpiner Höhlensinter. Stalagmiten aus dem Oman ergaben Aufschluss über Dauer und Verlauf des letzten Interglazial in niederen Breiten. Das Sinterwachstum setzte bei ~130 ka ein und endete vor ~116 ka. Während dieser Zeit hat sich die *ITCZ* so weit nach Norden verschoben, dass monsunale Niederschläge weite Teile der Arabischen Halbinsel erreichen konnten. Die Hauptwachstumsphase von 130 bis 124 ka stimmt mit dem Zeit–Interval hoher Insolation im Sommer überein, d.h. die solare Einstrahlung hatte großen Einfluss auf die Intensität des Sommermonsun. Dies beweist auch das Alter von Sintern, die durch Quellaustritte an der bronzezeitlichen Fundstelle *Jebel al–Buhais* in den Vereinigten Arabischen Emiraten entstanden. Die Quelle war dann aktiv, wenn die solare Einstrahlung besonders schwach, d.h. die Monsunaktivität gering war. So konnten Zyklone, die sich über dem Südindischen Ozean bildeten, ungehindert von der sonst vorherrschenden Südwestwindströmung auf die arabische Halbinsel vordringen und für Niederschläge sorgen. Die Datierung mehrerer Stalagmiten aus der *Djara–Höhle* nahe der *Farafra–Oase* in Ägypten ergab Alter >450 ka, zwei der Stalagmiten wurden auf ca. 400 ka datiert. Damals herrschte die ausgeprägte MIS 11 Warmzeit, die schon von anderen Klimaarchiven als die wärmste und ausgeprägteste der vergangenen ca. 500 ka bekannt ist.

Abstract

The age of secondary carbonate deposits has been determined via U/Th dating. According to the investigation of speleothems from the high Alpine *Spannagel Cave* (*Zillertal Alps*, Austria), a first warming occurred 135,000 years (135 kyr) ago. Sinter growth was interrupted from 130 kyr to 126 kyr, suggesting, that a cooler period preceded the start of the classical Eemian. Two additional growth interruptions within the Eemian suggest an unstable progression of the Last Interglacial, which terminated at 116 kyr. Thus, the classical Eemian lasted for about 10 kyr, which is the duration the Holocene has already reached. Another speleothem from *Spannagel Cave* formed during several warm periods of the past 250 kyr. The timing of the growth phases can only partly be explained by northern summer insolation maxima, which are thought to be the main trigger for climatic shifts by most paleoclimate researchers. A better correspondence is achieved by comparing the growth phases with the flux of Galactic Cosmic Rays reconstructed from deep sea sediments. These are probably affecting the condensation processes in clouds and accordingly, the Earth's energy budget and latent heat transport processes. Spectral analyses that were applied on the stable isotope profiles taken along the growth axis of a stalagmite from *Spannagel Cave* suggest, that the solar activity influenced Eemian climate, as the detected periodicities are similar to some well–known solar cycles. The existence of cycles with a periodicity of ~1470 years (*DANSGAARD/OESCHGER–cycles*) in both a stable isotope profile of a *Spannagel* flowstone and North–Atlantic sediments probably indicates, that the climate of Central Europe and the North–Atlantic circulation pattern are a coupled system. Stalagmites from Oman provided information about the timing and progression of the Last Interglacial in lower latitudes. Sinter growth commenced ~135 kyr ago and continued until ~116 kyr. During this period, the ITCZ has moved further to the North, so that the South Asian Monsoon could reach large parts of the Arabian Peninsula. The main growth phase lasted from 130 to 124 kyr, which coincides with the period of high summer insolation, suggesting, that solar insolation has a major impact on monsoonal strength. This finding is corroborated by the determined ages of sinter, which formed at a well close to the neolithic excavation site *Jebel al–Buhais* in the United Arab Emirates. The sinter formed during periods, when solar summer insolation was low, i.e. the summer monsoon was weak. Hence, southern ocean cyclones could reach the Arabian Peninsula, as they were not blocked by the south–western winds, that prevailed during times of strong summer monsoon. The dating of several stalagmites from *Djara Cave* (Egypt) yielded ages >450 kyr; only two stalagmites were dated at ~400 kyr, when the MIS 11 Interglacial prevailed. This interglacial has already been described by other paleoclimatic archives to be the warmest and longest of the past 500 kyr.

Table of Contents

1 Introduction

The ongoing discussion about anthropogenic influences on Earth's climate has led to an increasing number of climatological investigations. One way of assessing such influence is the application of climate models, which simulate the effects of the augmented impact of human activities on greenhouse gas concentrations and the Earth's surface properties. Additionally, the reconstruction of the past climate by the investigation of climate archives allows us to decipher any unprecedented anomalies, which can be attributed to human activities. Thus, paleoclimatic research can support and validate climate modelling rather than being an alternative, and the common aim is to understand past and to predict future climate.

A variety of climate archives has been investigated over the past decades. Deep sea sediments, corals, tree–rings, lake sediments, ice cores, and speleothems have been used as proxy records to reconstruct past climate. One major setback in reconstructing past climate results from the lack of absolute time scales. Most climate archives are dated by the comparison with the orbitally tuned *SPECMAP* curve, which is a record of stacked marine sediment cores. Therein the influence of the *MILANKOVITCH* curve is seen as the basic force to trigger climatic shifts. However, an increasing number of climate archives contradict the theory of orbital forcing as the only trigger. "Termination II", the transition from the penultimate glaciation to the Last Interglacial, represents a suitable example of the discrepancy between orbitally tuned time scales and absolutely dated climate archives, because the Last Interglacial was extraordinarily warm, and because the timing at about 135.000 years (135 kyr) enables us to date this event with reasonable accuracy.

This has been the main motivation to take a closer look at the Last Interglacial, hence the aim is to define an exact time scale for the beginning and termination of the Last Interglacial, and to improve our knowledge about the progression of the Eemian. A further step may be to decide whether the Eemian can be used as a template to the Holocene, or if each interglacial has to be treated as an unprecedented case. Therefore, it is interesting to view the other three interglacials of the past 400 kyr, labelled Marine Isotope Stages (MIS) 7, 9, and 11, and to give a rough frame for their timing and duration. This would enable us to compare the Eemian to the other interglacials (including the Holocene) in respect to their duration, climatic stability, and strength.

In chapter 2, an overview over the applied dating method, the mass spectrometric U–series dating technique, is given, as well as some basic features of utilizing secondary carbonate deposits as archives of the paleoclimate. Chapter 3 deals with the interglacials of the past 400 kyr, especially with the Last Interglacial / Eemian. A brief summary of climate forcing concepts and problems regarding the timing and progression of past warm periods is presented. The main part of this study is treated in chapter 4, with the results of the investigated speleothems and similar deposits from the high Alpine *Spannagel Cave* and from

the area influenced by the South Asian and African Monsoon. Both timing and duration of growth periods and stable isotope profiles are discussed. In chapter 5, the main conclusions that were drawn from this investigation are presented. All data that were produced and interpreted in this work (TIMS data and stable isotope data) are listed in the Appendix.

This investigation is carried out within the framework of the "Deutsches Klimaforschungs-Programm" (***DEKLIM***), which was founded by the *German Federal Ministry for Education and Research*. Different working groups worked in close collaboration in order to compare their results in a multi–proxy approach, reaching from palynological researchers, dating specialists to climate modellers. The main part of this study was conducted in cooperation with Prof. Dr. C. SPÖTL (University of Innsbruck), who carried out the sampling of the speleothems, studied the cave environment, and analyzed stable isotope profiles of speleothems from *Spannagel Cave*. The stalagmites from Egypt recording the African Monsoon were sampled in an expedition in January 2003, which was organized and led by Prof. Dr. H.J. PACHUR (FU Berlin); additionally, he provided another stalagmite (*FAR1*) from *Djara Cave*. Prof. Dr. Dr. H.-P. UERPMANN (University of Tübingen) conducted the archaeological excavation in the United Arab Emirates and helped with sampling and interpreting the calcareous sinter from *Jebel al–Buhais*. The physicist Dr. M. MUDELSEE (Boston University) is a specialist in time series analysis and performed the spectral analyses, which became an important part of this study. Dr. D. FLEITMANN (University of Bern) contributed the extraordinary stalagmites *H13* and *T1* from *Hoti Cave* and *Kahf Tahry* in northern Oman and analyzed parts of them for stable isotopes. They serve as high resolution archives of the Asian Monsoon during the Last Interglacial.

The wide variety of the different locations where the samples have been taken from is a basic concept of this work, enabling us to overcome the problem of sinter to be a representative of local climate solely.

2 Basics

2.1 U–series dating methods

U–series dating methods are by far the most reliable and precise methods for dating speleothems younger than 500 kyr (*Richards and Dorale*, 2003). The methods are based on the extreme fractionation of the parent U isotopes (^{238}U, ^{235}U, ^{234}U) from their long–lived daughters ^{231}Pa and ^{230}Th in the hydrosphere as a consequence of their widely different geochemical behavior. The return to secular equilibrium then allows quantification of time.

2.1.1 U and Th geochemistry

Typical U concentrations of the continental crust range from 0.1 µg/g (basalt) to 6 µg/g (granite). Mean values in limestone formations are about 2 µg/g, but may reach up to 100 µg/g in speleothems. Th concentrations in limestones are about 0 to 2.4 µg/g and up to ~10 µg/g in speleothems (*Ivanovich and Harmon*, 1992). The half–lives of the parent isotopes in the ^{238}U and ^{235}U radioactive decay–series are much longer than those of the intermediate daughters (table 2.1). Thus, the parent and daughter nuclides in undisturbed, naturally occurring materials with an age of several million years will be in a state of secular equilibrium.

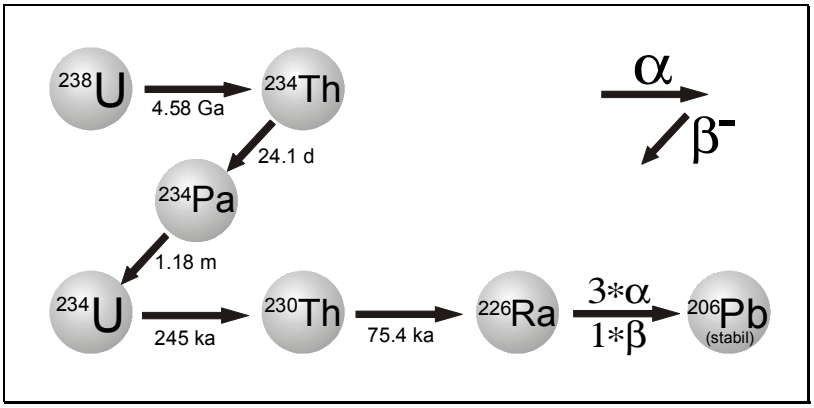

Fig. 2.1: Decay chain of ^{238}U subdivided into alpha– and beta–decay with respective half–lives (from *Neff,* 2001).

However, when a sedimentary deposit is formed, various geochemical processes occur which cause isotopic and elemental fractionation, initiating a state of disequilibrium between parent and daughter nuclides (*Ivanovich and Harmon*, 1992). A fractionation of the isotopes can occur as a result of radioactive decay of ^{238}U to ^{234}U, resulting in ^{234}U to sit more loosely in the crystal lattice of a mineral in comparison to its parent isotope (α–recoil effects (*Ivanovich and Harmon*, 1992)). Thus, ^{234}U is more mobile during weathering of the host rock than ^{238}U,

and the ($^{234}U/^{238}U$) activity ratio in groundwaters will generally be greater than one. Another fractionation process occurs between U and Th isotopes, as U is much more soluble and mobile in aqueous solutions than Th. In groundwaters, U occurs dominantly in the U^{6+} form as uranyl–ions ($(UO_2)^{2+}$), but can also be present in the much less mobile U^{4+} form in reducing environments. Th is invariably insoluble under natural conditions and therefore readily adsorbed on particles or transported in minerals. An important feature of both U and Th in the hydrosphere is their ability to form complexes with other ions (organic and inorganic), influencing their mobility and solubility (*Richards and Dorale*, 2003).
As a consequence of its insolubility ^{230}Th will be absent during the precipitation of secondary carbonates, like speleothems and travertines, and any ^{230}Th determined when a sinter is dated should be a product of the radioactive decay of ^{238}U and ^{234}U. Thus, by determining ^{230}Th and the $^{234}U/^{238}U$ ratio, the age of a sample can be calculated (see below).
Apart from its necessity for the age calculation, the initial $^{234}U/^{238}U$ activity ratio may provide information about the hydrological conditions under which the carbonate was deposited. Elevated ratios, for example, may be related to accumulation of ^{234}U in damaged sites during a period of reduced leaching, either as a result of lower soil pCO_2 or reduced soil moisture excess (*Richards and Dorale*, 2003).

2.1.2 U/Th dating method

As mentioned above, the decay–series in secondary deposits precipitated from U–bearing solutions will be in a state of disequilibrium, and – in an ideal case – no Th isotopes will be co–precipitated during sedimentary deposition. Given that no diagenetic changes or other migratory mechanisms occur after the initial formation of the deposit, the age of the original event can be calculated by determining the amount of daughter isotopes (^{234}U, ^{230}Th) relative to the parent isotope ^{238}U.

Table 2.1: Half–lives and decay constants of isotopes used for U–series age determination (*Cheng et al.*, 2000).

Isotope	$T_{½}$ [Myr]	Decay constant λ [1/yr]
^{238}U	4468.3	$1.55125 * 10^{-10}$
^{235}U	704	$9.8485 * 10^{-10}$
^{234}U	0.2446	$2.826288 * 10^{-6}$
^{232}Th	14010	$0.49475 * 10^{-10}$
^{230}Th	0.075381	$9.157711 * 10^{-6}$

The age t of a sample can be calculated iteratively by the following equation:

$$[2.1] \qquad \left[\frac{^{230}Th}{^{234}U}\right] = \frac{1-e^{-\lambda_{230}t}}{\left[\frac{^{234}U}{^{238}U}\right]} + \left(1-\frac{1}{\left[\frac{^{234}U}{^{238}U}\right]}\right)\frac{\lambda_{230}}{\lambda_{230}-\lambda_{234}}\left(1-e^{-(\lambda_{230}-\lambda_{234})t}\right)$$

where λ_i is the decay constant of the respective isotope, and the squared brackets indicate activity ratios (A = dN/dt = – λN, with N = number of nuclides). The equation can be illustrated graphically as shown in fig. 2.2.

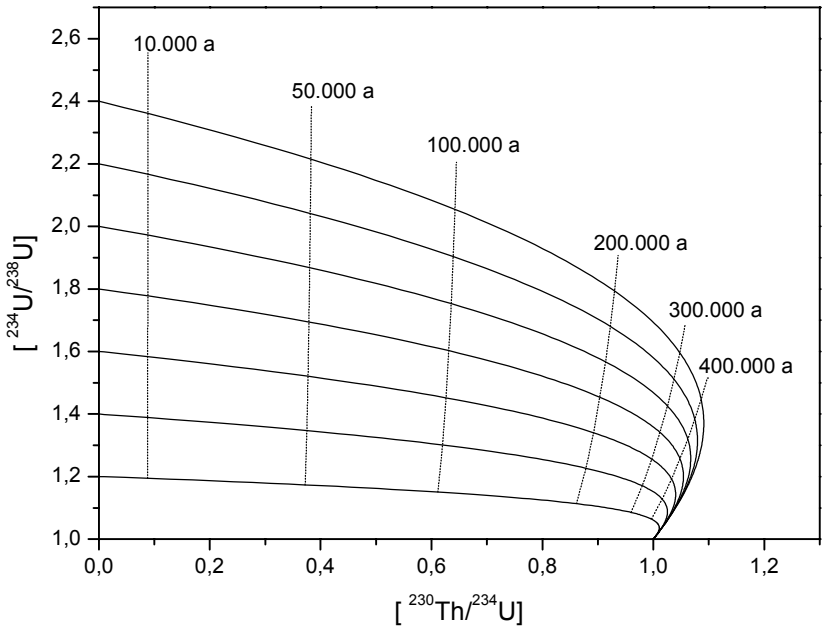

Fig. 2.2: Variation of $^{234}U/^{238}U$ and $^{230}Th/^{234}U$ activity ratios with time in a closed system with no initial ^{230}Th. The vertical lines are so–called isochrons, the near horizontal lines show the development of the activity ratios with time for different initial $^{234}U/^{238}U$ activity ratios.

The $^{234}U/^{238}U$ activity ratio can also be given in delta notation in ‰:

$$[2.2] \qquad \delta^{234}U = \frac{\left[\frac{^{234}U}{^{238}U}\right]_{mes} - \left[\frac{^{234}U}{^{238}U}\right]_{eq}}{\left[\frac{^{234}U}{^{238}U}\right]_{eq}} * 1000 = \left(\left[\frac{^{234}U}{^{238}U}\right]_{mes} - 1\right) * 1000 \quad [permil]$$

2.1.3 Correction for detrital contamination

As indicated in fig. 2.2, one basic assumption in the U–series dating technique is that all ^{230}Th present in a sample is formed *in situ* by radioactive decay of co–precipitated U. However, this assumption is not always fulfilled, so that initial ^{230}Th (detrital contamination by clay minerals or biogeneous material) has to be corrected for. There are various approaches available to account for detrital contamination, but the uncertainty of the final estimate is greater than would be expected for pure material (*Richards and Dorale*, 2003). Fortunately, for the samples presented in this work, the detrital correction was of minor importance, so that major uncertainties as a result of initial ^{230}Th did not arise. However, all calculated ages have been corrected for initial ^{230}Th, using ^{232}Th as an index of contamination. Owing to the generally great age of the detrital material (several millions of years), the activity ratios of all isotopes of the ^{238}U–decay series are assumed to be in secular equilibrium. Numerous measurements of ^{232}Th and ^{238}U of the Earth's upper crust yielded a mean mass ratio of (^{232}Th/^{238}U) ≈ 3.8 ± 1.0 (*Wedepohl*, 1995). Thus, the concentrations of non–authigenic ^{238}U, ^{234}U, and ^{230}Th can be calculated and corrected for, using the following equations:

[2.3] $$c\left(^{238}U_{detr}\right) = \frac{c\left(^{232}Th_{mes}\right)}{3.8}$$

From the detrital ^{238}U concentration c(^{238}U$_{detr}$) the activity [^{238}U$_{detr}$] can be calculated by:

[2.4] $$\left[^{238}U_{detr}\right] = c\left(^{238}U_{detr}\right) * 0.7478$$

where 0.7478 is the factor for calculating the specific activity of ^{238}U [dpm/g] from a concentration [µg/g]. Because it is assumed that ^{238}U$_{detr}$, ^{234}U$_{detr}$, and ^{230}Th$_{detr}$ are in secular equilibrium, the activities [X]$_{carb.}$ corrected for detrital contamination are:

[2.5] $$[^{238}U]_{carb.} = [^{238}U]_{mes.} - [^{238}U]_{detr.}$$

[2.6] $$[^{234}U]_{carb.} = [^{234}U]_{mes.} - [^{238}U]_{detr.}$$

[2.7] $$[^{230}Th]_{carb.} = [^{230}Th]_{mes.} - [^{238}U]_{detr.}$$

2.1.4 Sample preparation

For the mass spectrometric measurements, chemical separations of U and Th isotopes are required in order to remove unwanted interferences in the mass spectrum of U–series elements and to provide optimal ionization efficiency. The sample preparation has generally been performed as described in *Ivanovich and Harmon* (1992):
After surface purification by a brief leaching in suprapure 0.1 N HNO_3, the dried carbonate samples were weighted (between 0.05 g and 1.5 g, depending on expected U concentration) and dissolved in 1 N HNO_3. No insoluble remains were present for all samples, so that no

further treatment like filtration, centrifugation or HF decomposition was necessary. Defined amounts of U– and Th–spikes were added to determine U and Th concentrations. The solution was then chemically separated and purified utilizing DOWEX 1x8 ion exchange columns, which were loaded and purged successively with suprapure 7 N HCl and 7 N HNO_3. The resulting U– and Th–bearing HNO_3 solution was finally reduced to a droplet and transferred to rhenium filaments for the mass spectrometric analysis.

2.1.5 TIMS

The U/Th measurements were performed on a solid source thermal ionization mass spectrometer (TIMS) (Finnigan MAT 262 RPQ) with a double filament technique. After chemical sample preparation, the U– and Th–bearing droplet was put on a rhenium filament and thermally evaporated. A second filament sitting at a distance of about 1 mm from the loaded filament in the mass spectrometer provides a high temperature (~1700 °C) allowing a precise control of the ionization process. Due to their different specific evaporation and ionization temperatures, U isotopes were measured first, at temperatures between ~1680 and 1720 °C. Afterwards the temperature was increased to ~1730 to 1750 °C to analyze Th isotopes. The respective ions are accelerated by high voltage (~10 kV) and focused by an electromagnetic lens system. A strong magnetic field of about 1 Tesla separates the ions according to their mass/charge ratio. The abundance of each mass is then determined by its corresponding ion current, captured by Faraday cups (for high ion currents) or an Ion Counting Multiplier (ICM). For better mass separation, a Retarding Potential Quadrupol (RPQ) is used for Th measurements, effectively prohibiting interferences of similar masses. Details on TIMS measurements have been previously described (*Frank*, 1997, *Neff*, 2001).

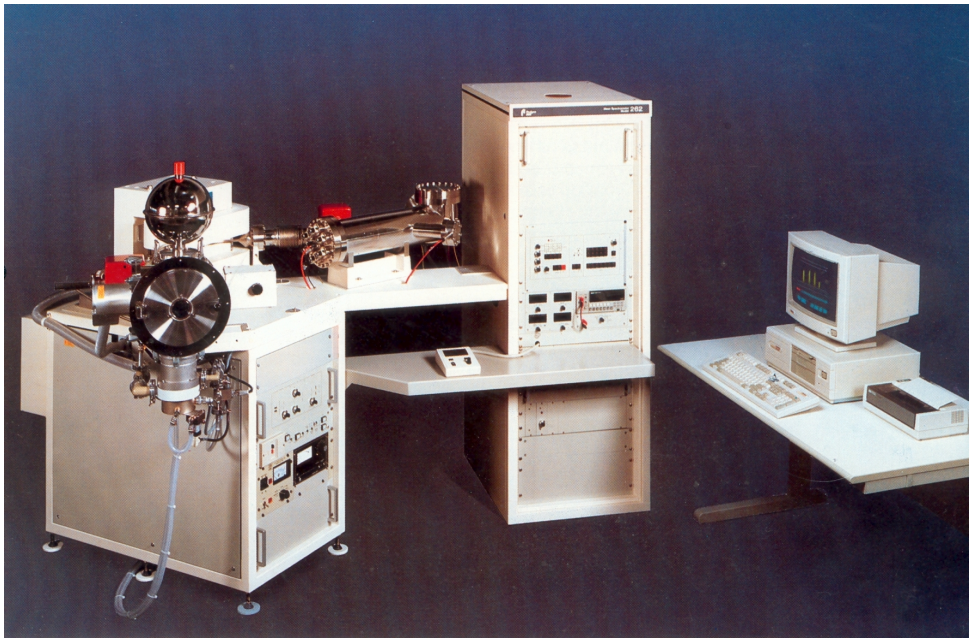

Fig. 2.3: Thermal Ionization Mass Spectrometer (Finnigan MAT 262 RPQ).

Due to better ionization efficiency, the U–series isotopes were measured in their oxidized forms UO and ThO, so that the relative abundance of the oxygen isotopes ^{16}O (99.756 %), ^{17}O (0.039 %), and ^{18}O (0.205 %) had to be corrected for. The detailed correction equations are described in *Neff* (2001).

2.1.6 Utilized standards and spikes

Regularly measured standards provided control on the reproducibility of isotope ratios, which were used for the age determination (*Frank et al.*, 2000). The reproducibility results from the standard deviation σ of the mean value $\bar{x}$ of single standard measurements x_1, x_2, ..., x_n.

[2.8] $$\sigma = \sqrt{\frac{\sum x_i^{\,2}}{n} - \left(\frac{\sum x_i}{n}\right)^2}$$

The utilized U–standard (*112A*) with a ^{238}U concentration of 4.3916 ± 0.0027 µg/g, is reproducible with a precision of 0.25 %. Fig. 2.4 shows the $^{234}U/^{238}U$ isotope ratios of *112A* measured between 1995 and 2003. The reproducibility of the Th–standard (*HDAKT1*) with a ^{232}Th concentration of 2.8331 ± 0.0022 ng/g is 0.6 % (fig. 2.5). However, due to the partially much greater U and Th concentrations of the measured samples, the reproducibility is markedly higher than those of the U– and Th–standards (e.g. that of the *Spannagel* samples), thus the standard reproducibility may rather give an upper limit. An exact value can not be given, as there was no standard available with similar concentrations as the measured samples.

To determine U and Th concentrations of the samples, a $^{233}U/^{236}U$ double spike was added prior to each measurement. Its ^{233}U concentration is 0.41468 ± 0.0015 ng/g, the $^{234}U/^{238}U$ isotope ratio is $5.2839 * 10^{-5} \pm 2.5291 * 10^{-8}$. An additionally injected Th spike with a ^{229}Th concentration of 0.1775 ± 0.0003 ng/g allowed for the samples' Th concentrations to be calculated.

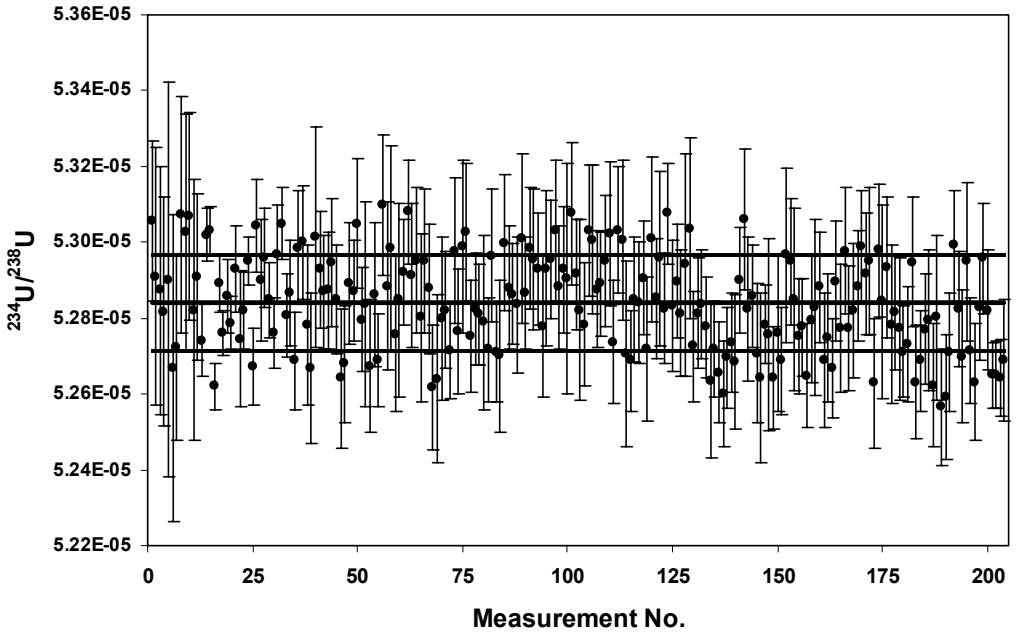

Fig. 2.4: U–standard measurements from 1995 to 2003. The horizontal bar represents the mean $^{234}U/^{238}U$ value of *112A*, the two dotted lines indicate the 1σ range.

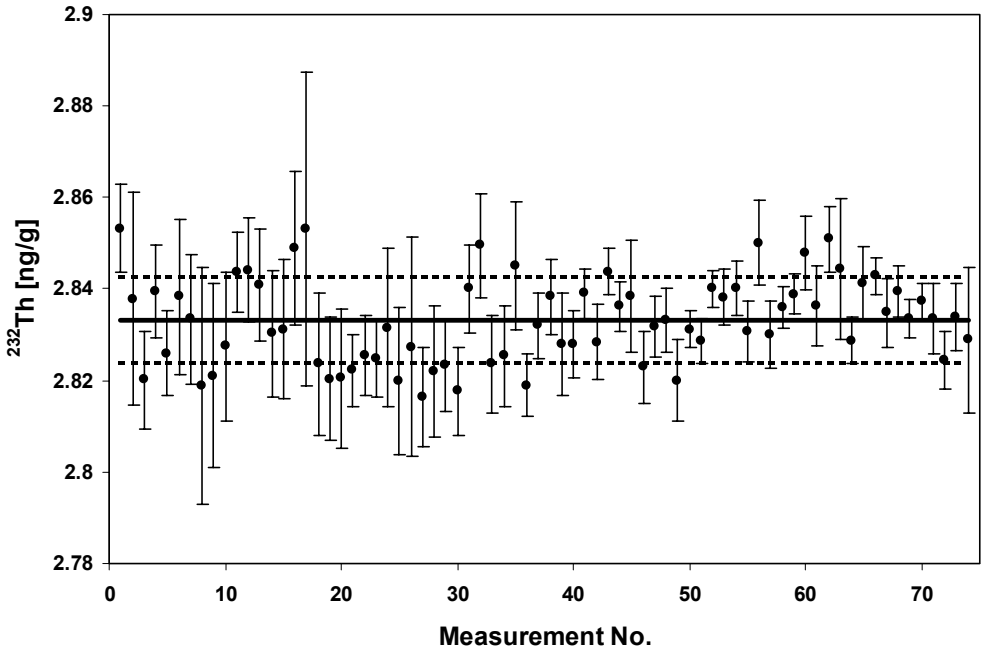

Fig. 2.5: Th–standard measurements from 1995 to 2003. The horizontal bar represents the mean ^{232}Th concentration of *HDAKT1*, the two dotted lines indicate the 1σ range.

2.2 Sinter formation

The word “sinter” is used here as an umbrella term for all secondary carbonates precipitated from supersaturated solutions. It includes all minerals precipitated from groundwater flowing or dripping in cave environments (i.e. “speleothems”, such as stalagmites, stalactites, flowstones, columns, helictites, …) as well as travertines and tufa, with the latter two more referring to superficial deposits precipitated from mineral or hydrothermal springs. Travertine and tufa are commonly produced by physiological and microbiological carbonate deposition taking place in groundwater with elevated carbon dioxide concentrations. However, these terms are used rather inconsistently in literature.

The basic requirement for the formation of calcareous sinter is the presence of carbonate ($CaCO_3$) in the host rock. 20 % of the Earth’s continental surface are underlain by carbonates (*Schwarcz*, 1986). Additionally, deposition of secondary carbonates relies on sufficient water and soil CO_2 supply to enable dissolution and transport of reactants from the interstitial host rock to the place of sinter formation (e.g. caves, …).

The saturation state with respect to carbonate is controlled by the CO_2 flux into or out of the water. Where the solution is undersaturated/aggressive, i.e. Saturation Index $SI < 0$ (with $SI = \log(K_{IAP}/K_{eq})$, K_{IAP} = Ion Activity Product, K_{eq} = Ion Activity in equilibrium with a mineral), dissolution of carbonate occurs (*Ford and Williams*, 1989). From a supersaturated solution ($SI > 0$) calcite and/or aragonite can precipitate. The predominant mineral is calcite, but aragonite and gypsum are also common. Aragonite is metastable under normal air pressure and is formed mostly biogenically or from Mg–rich solutions. In caves it is indicative of evaporative processes (*Richards and Dorale*, 2003).

The dissolution of CO_2 in water and the formation of carbonic acid is described by the following chemical reactions:

[2.9] $$CO_2 + H_2O \leftrightarrow H_2CO_3$$

[2.10] $$H_2CO_3 + H_2O \leftrightarrow H_3O^+ + HCO_3^-$$

[2.11] $$HCO_3^- + H_2O \leftrightarrow H_3O^+ + CO_3^{2-}$$

On its way through the fissures and crevices, the resulting acid solution can dissolve the carbonate host rock:

[2.12] $$CaCO_{3\,(solid)} + HCO_3^- + H_3O^+ \leftrightarrow Ca^{2+} + 2\,HCO_3^- + H_2O$$

The chemical equation describing the equilibrium of carbonate dissolution and precipitation can be summarized as:

[2.13] $$Ca^{2+} + 2\,HCO_3^- \leftrightarrow CaCO_3 \downarrow + H_2O + CO_{2\,(gaseous)} \uparrow$$

Hence, supersaturation with respect to carbonate may either be the result of (i) CO_2–degassing from the solution, (ii) of evaporation, or (iii) of an increase of the Ca^{2+}–activity by breakdown of complexing ligands or dissociation of Ca–complexes (*Ivanovich and Harmon*, 1992). For

speleothems, the main cause for calcite precipitation is CO_2–degassing, but evaporation may also occur near cave entrances or during drought periods.

CO_2–degassing from a solution occurs upon emergence into the lower pCO_2 of a cave or free atmosphere, if water was previously equilibrated with CO_2 in the interstitial percolation zone, where pCO_2 is elevated. The origin for such elevated pCO_2 may be manifold, but the most common cause is vegetation above the cave serving as CO_2–source, as the roots of plants add CO_2 to the interstitial soil atmosphere. Mixing ratios from 355 ppm (~ free atmosphere) to 115,000 ppm can be reached by respiration and biotic oxidation of biomass (*Atkinson*, 1977). As an alternative CO_2–source the oxidation of sulphides from the host rock, e.g. pyrite (FeS_2), may serve, where the resulting sulfuric acid can dissolve the carbonate host rock and CO_2 is released (*Atkinson*, 1983) (described in more detail on page 29).

Other processes have also been described, where speleothems formed in spite of the absence of vegetation above the cave and where no additional CO_2 is involved. It has been suggested that either warming of the water after entering the cave, or while percolating through the rocks above it might cause calcite supersaturation (*Dreybrodt*, 1982), or that water dissolving several Ca–bearing minerals (e.g. gypsum or dolomite) might precipitate calcite as the least soluble by the common–ion effect (*Atkinson*, 1983).

An overview over the most common shapes of speleothem deposits is given in fig. 2.6.

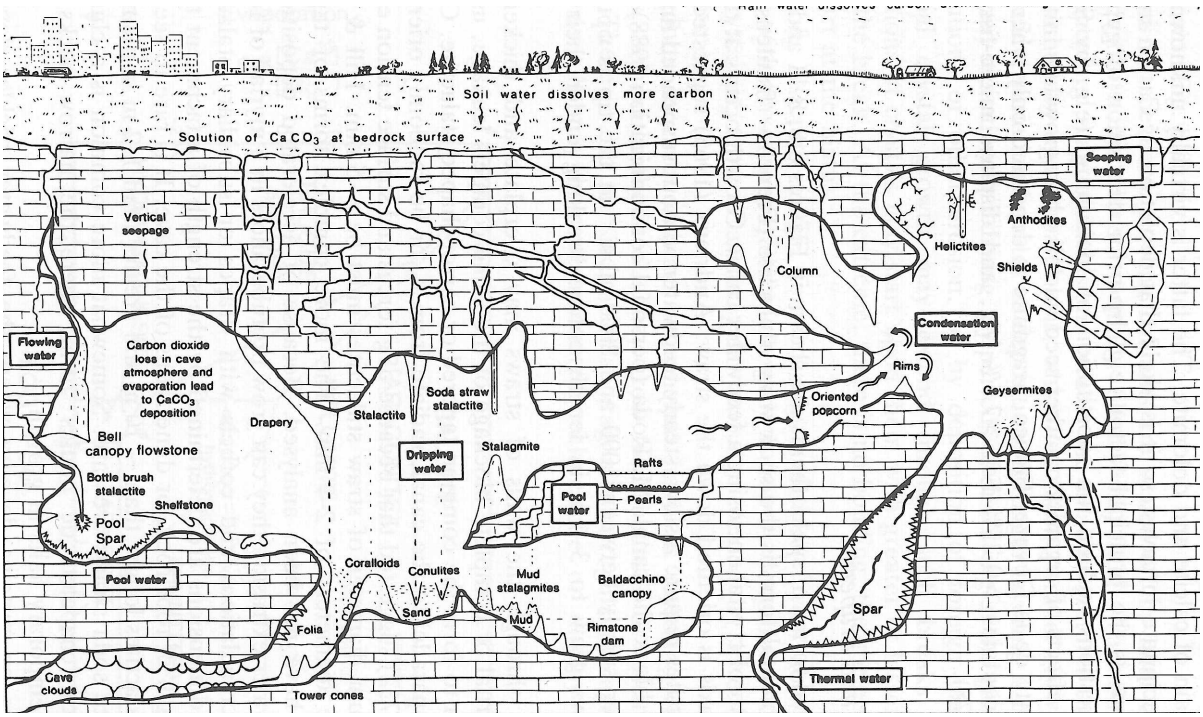

Fig. 2.6: Model for types of calcite and aragonite deposits in caves (*Hill and Forti*, 1986).

2.3 Calcareous sinter as paleoclimate archives

The potential of calcareous sinter as paleoclimate archives has increasingly being recognized over the past decades. A wide variety of parameters can be investigated from speleothems and similar deposits. Frequency distributions were one of the first reconstructions utilized, but they suffered from biased sampling strategies as well as low resolution at times of abrupt climatic change. The most important parameters of climate reconstruction that can be analyzed in carbonate deposits are listed in table 2.2.

Table 2.2: Overview over the most important parameters in sinter used for climate reconstruction, with the variable the parameter is indicative for, the achievable temporal resolution, the mostly utilized instrument / method the parameter is determined with, and some important references.

Parameter	Indication	Resolution	Instrument	Reference
Abundance	Sea level Temperature	variable	TIMS, ICPMS	(*Bard et al.*, 2002, *Richards et al.*, 1994, *Spötl et al.*, 2002)
Growth rate	Temperature Precipitation	variable	TIMS, ICPMS	(*Linge et al.*, 2001)
$\delta^{18}O$	Temperature Precipitation Hydrology	high	(Laser Ablation) Mass Spectrometer	(*McDermott et al.*, 2001, *Spötl and Mangini*, 2002)
$\delta^{13}C$	Vegetation Temperature Hydrology	high	Mass Spectrometer Laser Ablation	(*Baker et al.*, 1997)
Fluid Inclusions	Precipitation Temperature Hydrology	low / intermediate	Vacuum crushing cell / Mass Spectrometer	(*Dennis et al.*, 2001, *Harmon et al.*, 1979)
$\Delta^{14}C$	Solar activity Reservoir effects	high	AMS	(*Beck et al.*, 2001, *Neff et al.*, 2001)
Trace elements	Hydrology Vegetation Temperature	high	SIMS	(*Fairchild et al.*, 2000, *Roberts et al.*, 1998)
Pollen	Vegetation / Temperature & Precipitation	low	Counting	(*Genty et al.*, 2001)
Organic acids	Annual growth rates	high	Luminescence Spectrometer	(*Shopov et al.*, 1994)

Former investigations had suffered from large instrumental errors and poor temporal resolution. But improved technologies enabled researchers to perform high resolution

investigations. The number of available methods to determine the parameters listed in table 2.2 have increased rapidly and at the same time the precision and required sample size has been improved.

One major disadvantage of speleothems and other terrestrial carbonate deposits is that they are only significant for mainly local climate. Thus, a single deposit may or may not represent general (global, hemispheric,…) climatic conditions. This disadvantage in comparison to marine records can be compensated for by viewing at a large number of widely spread locations of terrestrial archives. An exception is the investigation of submerged speleothems, which serve as sea level indicators, when a cave's altitude lies within the range of past sea level fluctuations. E.g., submerged speleothems from the *Bahamas* are indicative for sea levels below the present value (*Richards et al.*, 1994). However, there have to be made corrections for tectonic movements, and interruptions of speleothem growth may also be caused by reasons other than sea level rise, such as local aridity or the absence of drip water.

In this work growth phases and stable isotope profiles ($^{18}O/^{16}O$ ratios and $^{13}C/^{12}C$ ratios) are utilized for climate reconstruction. Growth phases and enhanced growth rates are, in the viewed cases, indicative for warm climate (further explained in chapter 4), as sinter growth proofs the presence of liquid water at the time of formation, and as the production rate of CO_2 in the soil above a cave or at the place of carbonate dissolution increases with temperature and humidity (*Schwarcz*, 1986). Stable isotope ratios in carbonate deposits are influenced by several parameters and therefore provide a great potential for climatic interpretations.

$^{18}O/^{16}O$, $^{2}H/^{1}H$, and $^{13}C/^{12}C$ ratios (R) are usually expressed in δ notation, i.e. the deviation of the isotopic ratio of the sample relative to that of a standard:

$$\delta = \frac{R_{sample} - R_{standard}}{R_{standard}} \qquad [2.15]$$

$\delta^{18}O$, $\delta^{13}C$ and δD are expressed in permil versus the Vienna Standard Mean Ocean Water (VSMOW) (mainly used for meteoric water) or Vienna Pee Dee Belemnite (VPDB) (mainly used for carbonates). The conversion of $\delta^{18}O$ values given against one of those standards into the other one is given by:

$$\delta^{18}O_{VSMOW} = 1.03086 * \delta^{18}O_{VPDB} + 30.86 \qquad [2.16]$$

$$\delta^{18}O_{VPDB} = 0.97006 * \delta^{18}O_{VSMOW} - 29.94 \qquad [2.17]$$

(*Mook*, 1994)

The $\delta^{18}O$ values of the precipitated calcite are mainly controlled by two factors: (i) the isotopic composition of the water the deposit is fed by (i.e. precipitation and groundwater), and (ii) the conditions under which calcite is precipitated from the solution.

For the latter effect, two kinds of isotope fractionation may occur: (i) equilibrium fractionation or (ii) kinetic/disequilibrium fractionation. If equilibrium conditions prevail and provided that the isotopic composition of the groundwater can be estimated, the temperature at the time of growth can be calculated from calcite $\delta^{18}O$ (fig. 2.7). If the humidity in a cave or at the deposition site is high (close to 100 %) and ventilation is low, equilibrium conditions

may prevail, because no evaporation occurs. Additionally, the difference between pCO_2 of the drip water and ambient air (cave atmosphere) must be sufficiently low, so that CO_2–degassing from the solution happens slowly. Then, the thermodynamic fractionation between ^{18}O and ^{16}O on precipitation of calcite is about –0.24 ‰/°C at 10 °C (*Friedman et al.*, 1977) and increases slightly with lower temperatures. If kinetic fractionation occurred, a quantitative derivation of temperature from $\delta^{18}O$ values is impossible. Kinetic fractionation results from irreversible physical or chemical processes, such as evaporation of water with immediate withdrawal of the vapor from further contact with the water and the absorption and diffusion of gases.

The differentiation between equilibrium and kinetic fractionation conditions can be made by viewing the correlation between $\delta^{13}C$ and $\delta^{18}O$ values along single growth layers of a stalagmite or sinter (*Hendy*, 1971). Under equilibrium conditions, the $\delta^{13}C$ values may rise with increasing distance from the growth axis of a stalagmite, whereas the $\delta^{18}O$ values may remain constant. This is due to reservoir effects, because carbon (HCO_3^-) is limited in the solution, from which $CaCO_3$ is progressively precipitated, whereas the oxygen reservoir remains almost unchanged. Concomitant increasing of both $\delta^{13}C$ and $\delta^{18}O$ values is indicative for kinetic fractionation, because evaporation of water or CO_2 affects both isotopes.

However, $\delta^{18}O$ values of precipitated calcite also depend on the $\delta^{18}O$ of the source the groundwater is fed by (i.e. precipitation). Various parameters cause changes of the stable isotope composition of precipitation (*Mook*, 1994): the *ocean temperature effect* reflects the temperature dependent fractionation between liquid and vapor phase at the source of the atmospheric moisture. The *rainwater composition effect* relates to the fate of the air mass on its route from the site of evaporation to the site of rainfall (including the amount of precipitation, the location of the site with respect to the distance from a coast, its altitude, its latitude, and the season during which the precipitation falls), and the *ice volume effect*, which influences the isotopic composition of the oceans, the main sources of cloud humidity. All these effects are known, but bear uncertainties when it comes to the task of an exact quantification of their influence on the isotopic composition of precipitation. In most cases, the meteoric–dependent isotopic shifts will be greater than those of the thermodynamic fractionation mentioned above (*Lauritzen and Lundberg*, 1999). This makes an exact calculation of sinter growth temperatures difficult or even impossible.

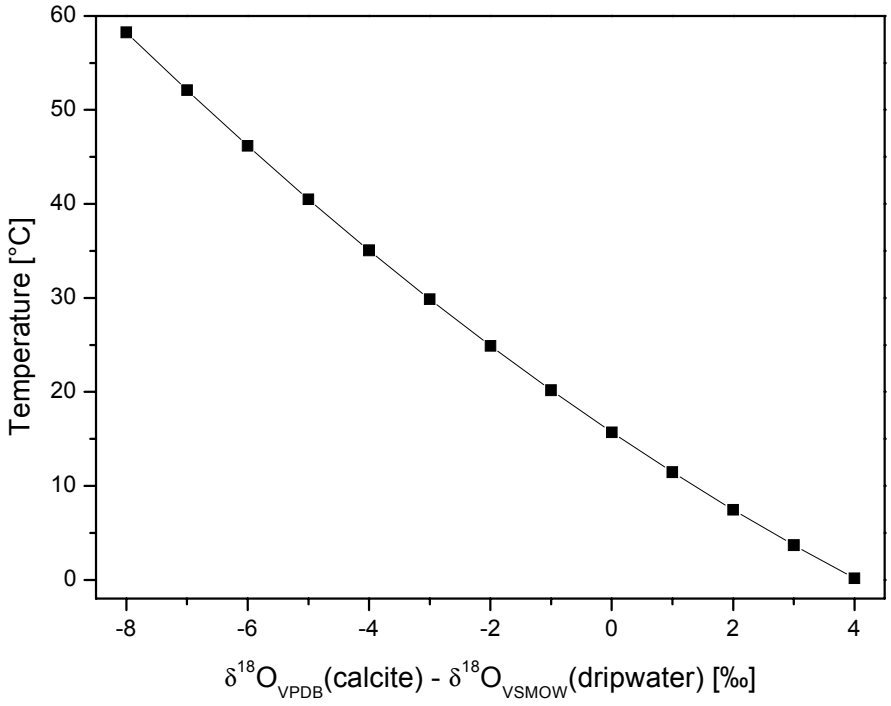

Fig. 2.7: Temperature dependence of $\delta^{18}O$ for the transition from drip water to calcite (*O´Neil et al.*, 1969).

The problem of estimating past patterns of precipitation $\delta^{18}O$ from calcite $\delta^{18}O$ values can be circumvented by measuring the isotopic composition of relict drip water that is preserved within fluid inclusions trapped in the host calcite at the time of growth. Up to 0.3 wt. % of a speleothem can consist of fluid inclusions, common values range between 0.001 % and 0.1 % (*Richards and Dorale*, 2003). Due to such low concentrations, the achievable resolution of fluid inclusion analyses is comparably low, as large calcite samples have to be recovered to get water amounts large enough for being analyzed by mass spectrometry.

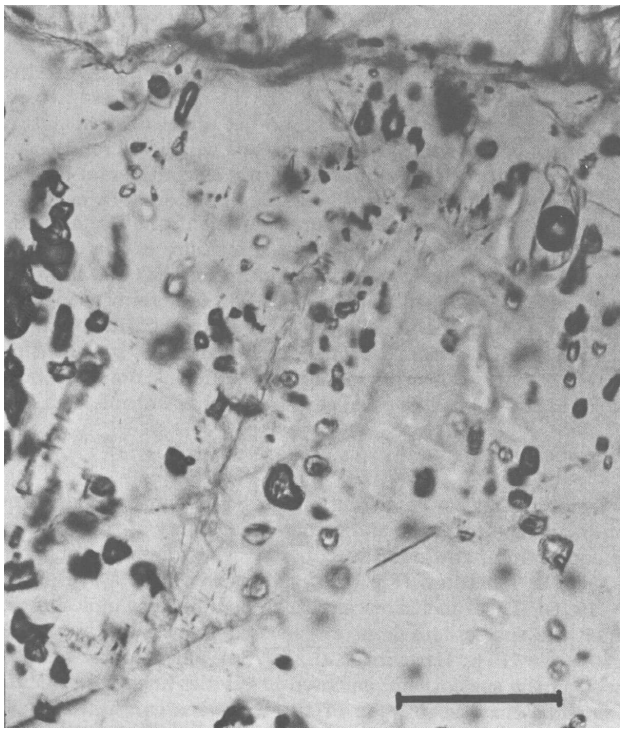

Fig. 2.8: Photograph of fluid inclusions in a stalagmite. The scale bar represents 0.1 mm. (*Schwarcz*, 1986)

Even more complex than $\delta^{18}O$ is the interpretation of $\delta^{13}C$ values of secondary carbonates, as they depend on various factors: Three sources contribute to the dissolved carbon in seepage waters and the resulting precipitated carbonates: (i) the limestone host rock where the solution is percolating through, (ii) atmospheric CO_2, and (iii) decaying organic matter and root respiration in the soil zone. The $\delta^{13}C$ value of the precipitating carbonate will therefore depend on the $\delta^{13}C$ values and the relative contribution of each source, as well as on numerous other factors, such as kinetical fractionation processes, the saturation state of the solution with respect to $CaCO_3$, the rate of precipitation, and the exchange of the solution with the gaseous phase (*Richards and Dorale*, 2003). All these factors are more or less influenced by the prevailing temperature and amount of precipitation at the deposition site. Thus, the derived information from $\delta^{13}C$ values of a deposit is an indirect measure of climatic settings.

The main information that have frequently been derived from $\delta^{13}C$ profiles are changes in vegetation. Both vegetation density and the metabolism type of the plants influence the $\delta^{13}C$ values of precipitated carbonates. CO_2 respired from C_3 plants (with the photosynthetic *Calvin Cycle*) results in carbonate values ranging from –14 ‰ to –6 ‰, whereas those of C_4 plant types (photosynthetic *Hatch–Slack* pathway) vary between –6 ‰ and +2 ‰ (*Dreybrodt*, 1980). C_4 plant types are typically adapted to conditions of extreme aridity and warmth, so that shifts in the $\delta^{13}C$ values can be related to changes of vegetation type and climate conditions. Additionally, changing vegetation density and soil respiration rates also control pedogenic carbonate $\delta^{13}C$ values. Hence, caution is needed before interpreting $\delta^{13}C$ signals within carbonate deposits in terms of paleovegetation and paleoclimate.

3 The climate of the past 400 kyr – an overview

3.1 Paleoclimate records of the past 400 kyr

The Quaternary can be divided into glacial and interglacial intervals, which refer to a general state of global climate (*Kukla*, 2002). The labels of classical Quaternary stages derived from geomorphologic records (*Weichsel*, *Würm, Eemian, Sangamon*, *Holsteinian*, …) are increasingly being replaced by units defined in continuous deposits, such as glacier ice, deep–sea sediments, lake sediments, and soil sequences. Marine Isotope Stages (MIS) are meanwhile the most commonly used units, reflecting the total global volume of land–based ice. One major advance of the last few decades in paleoclimatology has been the attempt to correlate various climatic records and to compare their implications with respect to timing and significance (*Sanchez-Goni et al.*, 1999, *Shackleton et al.*, 2003, *Spötl and Mangini*, 2002, *Winograd et al.*, 1997). However, the mechanism causing switches of the Earth's environment between warm interglacial and colder glacial modes remains unclear.

It is widely accepted that the main force that drove the glacial cycles is high latitude Northern Hemisphere summer insolation with its major climatic feedback associated with the waxing and waning of the northern continental ice sheets (*Milankovitch*, 1941). The frequency and amplitude of the *MILANKOVITCH cycles* result from the precession of the equinoxes, changes in the eccentricity of the Earth's orbit, and changes in the Sun's elevation above the horizon (tilt), which vary with a periodicity of 23 and 19 kyr/cycle, 413 and 100 kyr/cycle, and 41 kyr/cycle, respectively (fig. 3.1).

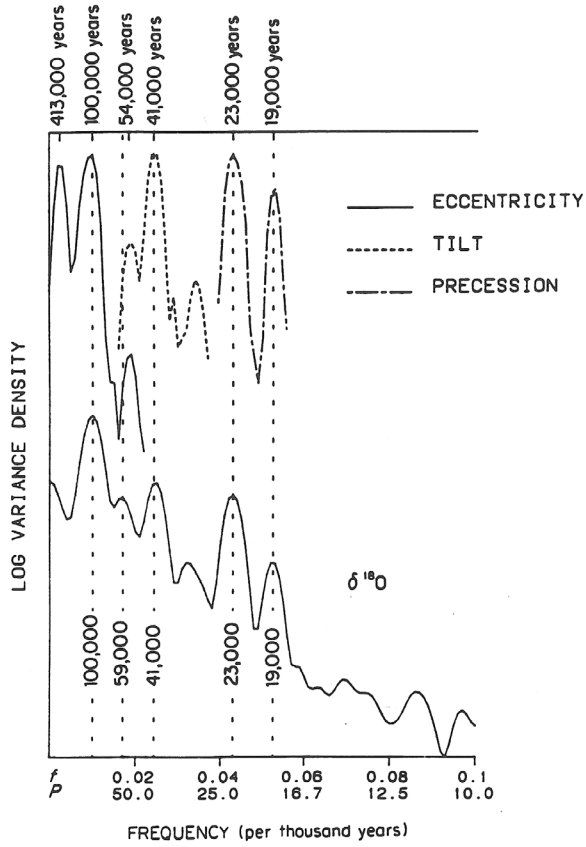

Fig. 3.1: Variance spectra for marine oxygen isotopes of the last 700 kyr (lower curve) compared with the orbital elements of seasonality. (from *Broecker*, 1993)

Some of these orbital cycles can be recovered in the climate of the past 400 to 800 kyr, which were dominated by a 100 kyr cyclicity (fig. 3.2). The 100 kyr cycles were first discovered by a joint application of magnetostratigraphy and changes in the $\delta^{18}O$ in fossil planktonic *foraminifera* in ocean sediments, representing changes in total Northern Hemisphere ice volume (*Shackleton and Opdyke*, 1973). Based on the subdivision of marine sediment cores into isotope stages by C. EMILIANI in 1955, which depends on U–series dated sediments, a revised chronology was set up, locking the phase of the observed cycles to an orbital template (*Imbrie et al.*, 1984). It was presupposed that the variations of proxy paleoclimate records are the result of changes in insolation. This orbitally tuned *SPECMAP* time scale is sufficient for explaining long term climatic processes and slowly reacting ice sheet melting and sea level changes. It is the best chronostratigraphic time scale available for the last several million years and therefore the reference for all long marine and terrestrial paleo–records. However, it does not explain short term shifts, and absolute dates have shown that the insolation alone is not sufficient to explain important features of past climate. Additionally, the predominance of a 100 kyr periodicity, when most of the insolation forcing occurs in the precession and obliquity bands, has not been sufficiently explained.

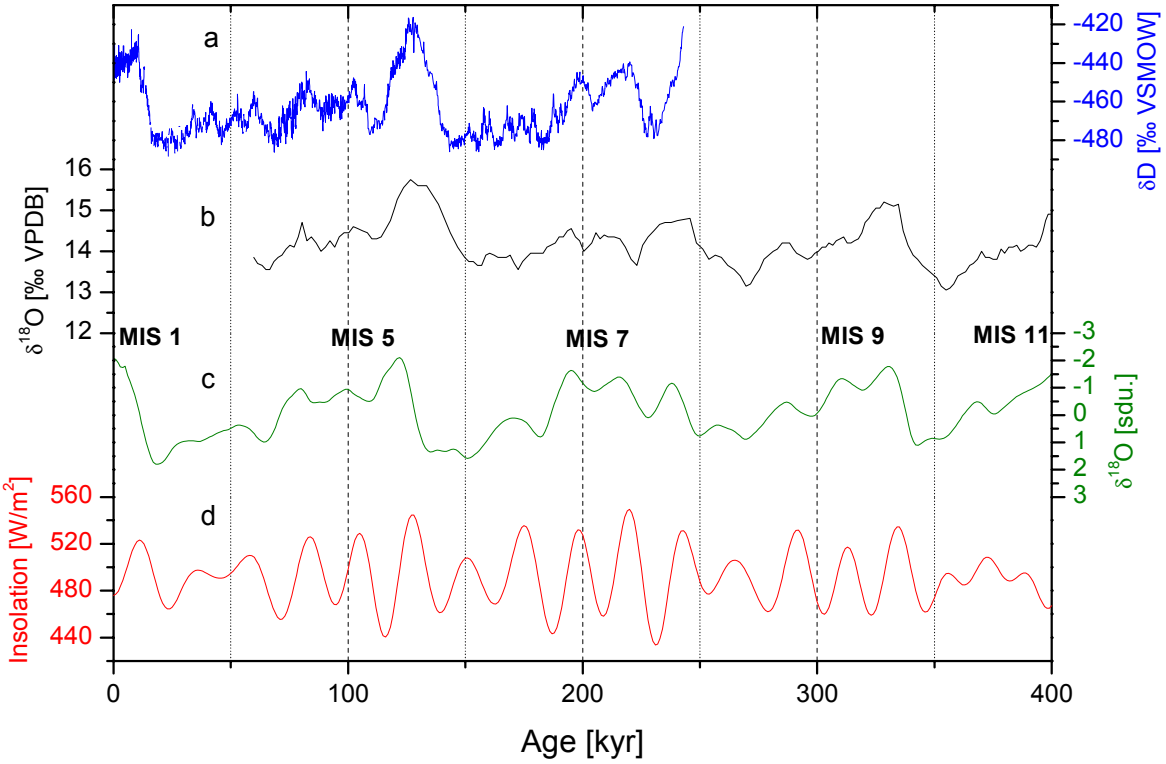

Fig. 3.2: Comparison of terrestrial and marine climate archives and insolation with associated Marine Isotope Stages (MIS). **a:** Deuterium in *Vostok* ice core (*Petit et al.*, 1999); **b:** $\delta^{18}O$ from *Devils Hole* calcite vein (Nevada, USA) (*Winograd et al.*, 1992); **c:** $\delta^{18}O$–*SPECMAP* curve *(Imbrie et al., 1984)*; **d:** June insolation at 60°N.

The analysis of the U–series dates of the *Devils Hole* $\delta^{18}O$ paleotemperature record indicates that the last four interglaciations range from 20 kyr to 26 kyr in duration (*Winograd et al.*, 1997). Additional evidence for an ~19 kyr duration comes from *Vostok* ice core and from U–

series dated sea–level highstands (*Stirling et al.*, 1995). These independently dated records contradict the estimated duration of 11 kyr to 13 kyr derived from the *SPECMAP* chronology. Furthermore, there are significant phase offsets of several thousand years between the different climate records (see chapter 3.2).

Orbital cycles are not the only force initiating climatic shifts. E.g., Greenland ice cores and North Atlantic sediments reveal the presence of regular abrupt climate changes appearing during the last glacial period, the so–called *DANSGAARD/OESCHGER* (*D/O)–cycles*. The duration of each cycle is 1.5 kyr, with an astonishing continuity throughout the ~20 detected cycles (fig. 3.3). This suggests that these events were paced either by internal ice sheet processes, or by variations in solar energy output, acting in a highly regular pattern (*Bond et al.*, 2001).

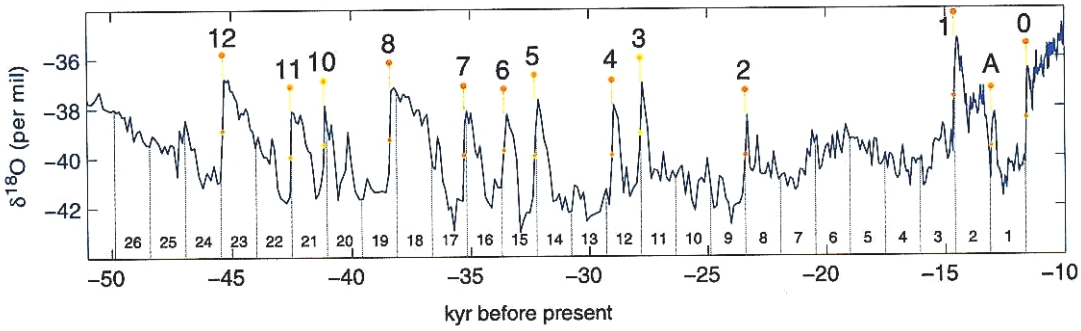

Fig. 3.3: The GISP2 climate record for the period 50 kyr to 10 kyr. *DANSGAARD/OESCHGER* warming events are numbered and marked by red dots. The distance between two subsequent vertical lines is 1.5 kyr. (*Rahmstorf*, 2003)

It is supposed, that the *D/O–Events* are the result of state changes in the thermohaline ocean circulation of the Atlantic, namely a shift in the latitude of *North Atlantic Deep Water* (*NADW*) formation (*Rahmstorf*, 2003). Such shifts can be triggered by small cyclic variations in the freshwater budget of the Nordic Seas. However, the origin and cause driving these short term oscillation are still being discussed.

It has become clear that the climate system is sensitive to long– and short term forcing mechanisms and that it responds in a highly non–linear way with large and often abrupt changes (*Rahmstorf*, 2002). Once understanding the driving forces and feedbacks of the climate and once knowing the exact lengths and progressions of former interglacials, the expected duration and stability of the Holocene in comparison to previous interglacials could be forecasted and anthropogenic influences could be estimated more precisely. Hence, a common aim of most paleoclimate investigations is to predict the future development of the recent interglacial, the Holocene.

Therefore, a closer look at the Last Interglacial seems appropriate. Though the long *Holsteinian* warm stage (MIS 11), about 400 kyr ago, represents an even closer analog of the current orbit, the Last Interglacial is preferred, because the relative lack of paleoclimatic evidence from MIS 11 leaves the Last Interglacial as the best available interval to compare our Holocene with. It is described in more detail in the subsequent chapter.

3.2 The Last Interglacial and the Eemian

3.2.1 Terminology

The usage of the terms “Last Interglacial”, “MIS 5e”, and the “Eemian” has been extensively discussed (*Kukla*, 2002, *Shackleton et al.*, 2003), but can still cause misunderstanding in paleoclimate discussions. The Eemian is associated to, but not an equivalent to MIS 5e (*Shackleton et al.*, 2003). The Eem zone was originally described in the vicinity of the *Eem* river in the Netherlands by HARTING in 1874 and refers to marine deposits indicative for warm climate. Due to the lack of radiometric dating, an exact time scale for the Eemian was not given and the term was rather used as a biostratigraphic sequence. It may be recognized in a vegetational sequence as the interval dominated by forest elements, preceded by the open vegetation of the previous glacial, and succeeded by the open vegetation of the last glacial complex (*Turner and West*, 1968). Other European pollen zones were taken as coeval and dated by comparison to oceanic records. However, the upper and lower boundaries may be of different ages in comparison to the marine records, and also relative to each other. E.g., the Eemian pollen zones in France and off Portugal probably correspond to an interval which was considerably longer than that in the Netherlands and Germany (*Kukla*, 2000, *Sanchez-Goni et al.*, 1999, *Shackleton et al.*, 2002). In southern and western Europe, the base of the Eemian is significantly younger than the base of MIS 5, and falls within the isotopic plateau of MIS 5e, during which global sea level is thought to have been a few meters higher than at present (*Shackleton et al.*, 2003), and the Eemian reached well into a period corresponding to MIS 5d.
Marine Isotope Stages (also: Oxygen Isotope Stages) refer to the $\delta^{18}O$ values of benthic *foraminifera* records, closely reflecting the variations of global ice volume.
The term “Last Interglacial” is used more generally and represents an interval with climate as warm or warmer than today, of low global ice volume and high sea level (*Kukla*, 2002). As the samples presented in this work neither refer to pollen zones nor to marine isotope stages *sensu stricto*, this term is mainly utilized for the growth phases of sinter of the Last Interglacial complex.

3.2.2 Termination II

The beginning of the Last Interglacial has been extensively discussed. According to the *MILANKOVITCH curve*, it did not commence before 128 kyr, when northern summer insolation reached its maximum. Accordingly, MIS 5e in the orbitally tuned *SPECMAP* curve commenced at 128 kyr, when defining the MIS 5/6 boundary (the so–called Termination II) as the mid point of the transition from glacial to full interglacial $\delta^{18}O$ values. In contrast, some other marine and terrestrial records have put the beginning of the Last Interglacial between 132 kyr and 135 kyr, the most important of which are:

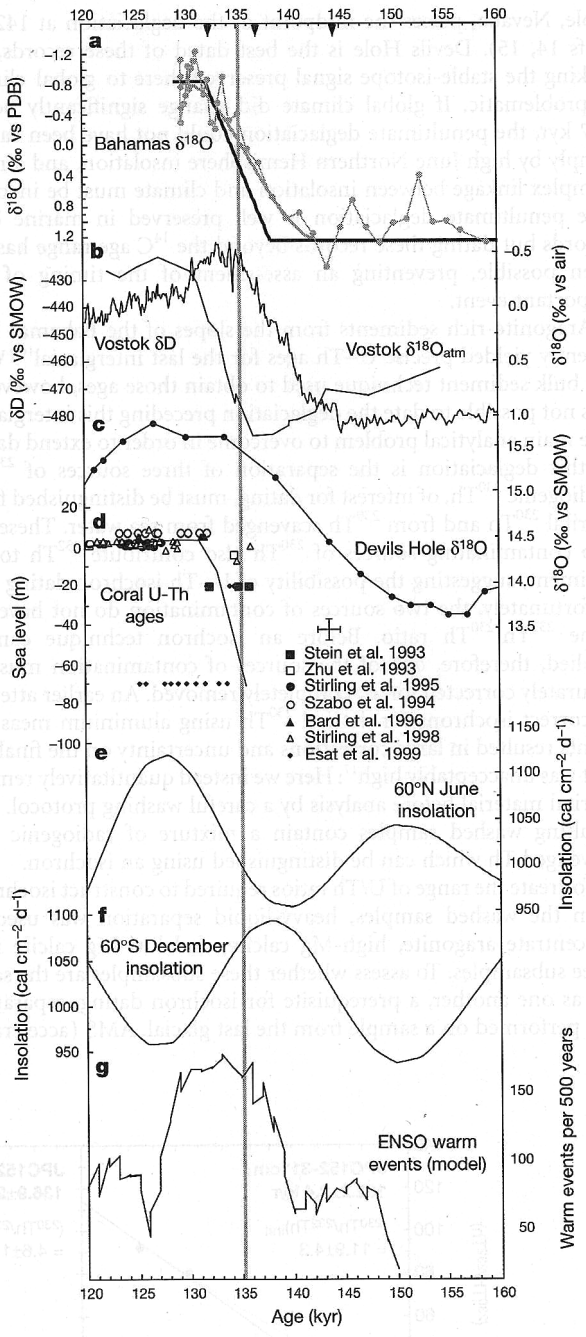

Fig. 3.4: Timing comparison of Termination II between different climate archives: **a:** $\delta^{18}O$ record from *Bahamas* slope sediments; **b:** *Vostok* δD (*Lorius* time scale) and $\delta^{18}O$ of atmospheric CO_2; **c:** *Devils Hole* $\delta^{18}O$; **d:** selected coral U/Th ages versus reconstructed sea level; **e, f:** Insolation curves for summer months at 60°N and 60°S; **g:** Number of ENSO events per 500 years in an orbitally forced model of the tropical Pacific. (*Henderson and Slowey*, 2000)

- The $\delta^{18}O$ values of the *Devils Hole* calcite vein (Nevada) represent the isotopic values of winter and spring precipitation, which are sensitive to the air temperature in that area. An early atmospheric warming was determined by U/Th datings with an unprecedented accuracy at that time, with the midpoint of the transition between glacial and interglacial $\delta^{18}O$ values being at 140 ± 3 kyr and the Last Interglacial plateau lasting from 134 kyr to 124 kyr (*Winograd et al.*, 1992). The record has extensively been criticized as local phenomenon or as being incorrectly dated (*Lea*, 2001, *Shackleton et al.*, 1993), but a number of additional archives corroborate the finding of an early warming of the Last Interglacial.
- The growth of speleothems at a high Alpine site, where today's temperatures are slightly above freezing point, as early as 135 ± 1.2 kyr testifies the presence of

liquid water and resultantly temperatures as high or higher than today (*Spötl et al.*, 2002).

- A complete sequence of Last Interglacial ice is present at *Vostok,* Antarctica. The δD values indicate increased air temperatures reaching current values at 132 kyr and remained as high or higher for about 13 kyr. The time scale was derived from an ice flow model tied to the astronomic chronology at two points, at 110 kyr and 390 kyr. The accuracy of the absolute dating is estimated to be about ± 5 kyr (*Petit et al.*, 1999).
- A sea level high stand at 135.2 ± 2.5 kyr was derived from U–rich slope sediments from the *Bahamas*, which were dated using a U/Th isochron technique (*Henderson and Slowey*, 2000), and it was suggested that possibly Southern Hemisphere summer insolation or changes in the tropical ocean–atmosphere system may have been involved.
- According to the U–series dating of uplifted coral terraces from *Alladin's Cave* at *Huon Peninsula* (Papua New Guinea), the sea level started to increase 140 kyr ago and rose to –14 m below the present level 135 kyr ago (*Esat et al.*, 1999).
- From combined ^{230}Th and ^{231}Pa datings of uplifted coral terraces from *Barbados*, a sea level of –18 ± 3 m below the present value at 135.8 ± 0.8 kyr has been derived (*Gallup et al.*, 2002).

Furthermore, according to a δ^{18}O record of North Atlantic core *MD95-2042*, which was put on a time scale by correlating the isotope curve with other records exclusively based on radiometric dates from uplifted coral terraces, Termination II was at 132 kyr, and the plateau of MIS 5e covers 128 kyr to 116 kyr (*Shackleton et al.*, 2002). Thus, there is recently little doubt that the first warming of the Last Interglacial commenced prior to the maximum of solar summer insolation, raising the question what initiated the termination of the penultimate glaciation.

3.2.3 Climate progression during the Last Interglacial

Investigations regarding the stability of the Last Interglacial climate have resulted in controversial debates. A number of archives derives clear indication, that the Last Interglacial climate was rather stable (*Boettger et al.*, 2000, *McManus et al.*, 1994, *Rioual et al.*, 2001), but there also exist records suggesting, that it was interrupted by one or more colder periods. A return to glacial conditions after an early first warming of the Last Interglacial is derived from U/Th dated coral terraces from *Huon Peninsula*, and the age of the cold event was dated ~130 kyr (*Esat et al.*, 1999). A sea–level regression–transgression cycle, which lasted for about 1.5 kyr, is recorded in a reefal facies on the *Bahamas*, which was U–series dated at 124–125 kyr (*Wilson et al.*, 1998), and has also been detected in another site of the *Bahamas* (*Hearty and Neumann*, 2001). Another archive recording a cool event within the Eemian is ODP Site 658 in the subtropical Atlantic, where benthic oxygen isotope values show a short,

but significant peak at ~122 kyr (*Maslin and Tzedakis*, 1996). At the same time, a brief interval of higher $\delta^{18}O$ values is visible in Site 769 in the *Sulu Sea* in the western Pacific (*Linsley*, 1996). The proxy temperature records from the three North Atlantic sediment cores display a number of high–frequency and high–amplitude variations, with main coolings at ~127–126 kyr, ~122–121 kyr, and 117 kyr (*Fronval and Jansen*, 1996). Two intra–Eemian cold events were detected in maar lake deposits in the *Massif Central*, France, but they could not be placed on an absolute time scale (*Thouveny et al.*, 1994).
Three features may possibly be responsible for the controversial results of different archives:

(i) The temporal resolution of a record might not be sufficient for recording events lasting a few hundred or thousand years only.
(ii) An archive might record local climate mainly instead of representing global or, at least, regional climate.
(iii) The lack of reliable absolute age determinations may result in a vague assignment of the viewed section of a record to the Eemian *sensu stricto* or to the Eemian in a wider context (i.e. a first warming corresponding to MIS 5e / "Pre–Eemian").

Yet, the problem is important, as it leads to the answer of the question, if climatic shifts within interglacials are naturally occurring phenomena. There have very few records been investigated where all mentioned problems can be excluded. As deep sea sediments are most likely to meet the criterion of representing global climate, a tentative way of assessing is to view marine records and subsequently compare the results with that of continental archives. A unique case is realized in the marine core *MD95-2042* from the south–western margin of the Iberian Peninsula, where a direct land–sea correlation demonstrates that during the Last Interglacial complex, the terrestrial climatic signal was similar to that of the ocean, and that North Atlantic sea–surface temperatures were in phase with European climate (*Sanchez-Goni et al.*, 1999) (fig. 3.5). In this core, a *Younger Dryas* like event ("*Heinrich event 11*") was detected, indicating a two–step deglaciation at Termination II, corroborating the finding of a "pre–Eemian" warming from other terrestrial (*Holzkämper et al.*, submitted) and marine (*Esat et al.*, 1999) records. The classical Eemian determined in core *MD95-2042* corresponds to the lightest isotopic values of MIS 5e and the heavier values towards the 5e/5d transition, lasting from ~126.1 kyr to 109.7 kyr. During this time, the sea level remained "more or less stationary" within a range of ± 10 m compared to the present value (*Shackleton et al.*, 2002), a range which is large, allowing for major cold spells to be explained during the Eemian. Furthermore, pollen an *dinocyst* data allowed the characterization of four different climatic phases during the Eemian which are difficult to establish on the basis of the isotopic data alone, with low amplitude oscillations from initially Mediterranean conditions to more oceanic climate, followed by a colder phase and finally a drying trend towards the end of the Eemian.

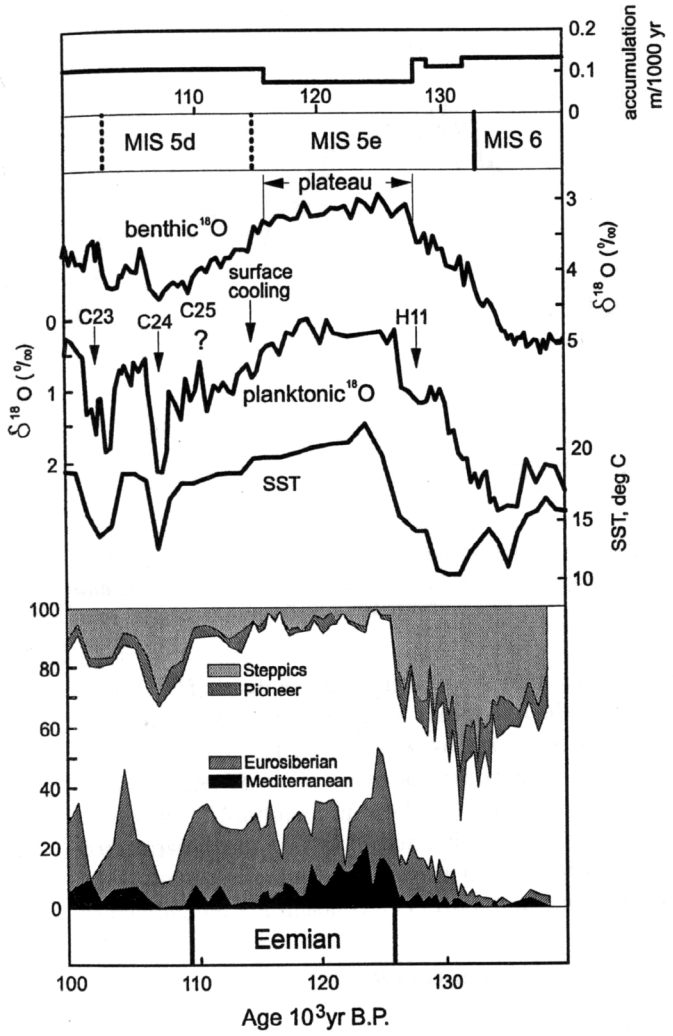

Fig. 3.5: Marine and continental records of the Last Interglacial period. From top to bottom: sedimentation rate from core *MD95-2042* (off the Iberian margin); Marine Isotope (Sub-) Stages; benthic $\delta^{18}O$ record from *MD95-2042*; planktonic $\delta^{18}O$ record with cold events (arrows) from North Atlantic core *NEAP18K*; sea surface temperature based on alkenones from *NEAP18K*; major groups of pollen taxa, on which the delimitation of the Eemian is based (*Shackleton et al.*, 2002).

3.2.4 The end of the Last Interglacial

The end of the Last Interglacial, following the decrease in summer insolation at high northern latitudes after 128 kyr, is documented by marine sediments, as for example by the previously described core *MD95-2042* from the Iberian margin. There, the MIS 5e plateau lasted until 116 kyr, and the midpoint of the transition from interglacial to glacial $\delta^{18}O$ values (i.e. sea levels) was dated at 115 kyr. At about this time, open vegetation started to replace forests in north–western Europe and the proportion of conifers increased significantly farther south. However, the essential interglacial conditions in south–western Europe prevailed until late MIS 5d, ~107 kyr ago (*Kukla*, 2002). This age coincides with the southward and eastward expansion of cold water in the North Atlantic recorded by peak *Ice Rafted Detritus* (*IRD*) values in marine sediments (so–called cold event "*C24*"), indicating the inception of the last glacial (*McManus et al.*, 1994). Thus, the environmental shift from peak interglacial into early glacial environments in the Atlantic and western Europe advanced gradually from high to middle latitudes, with tropical and mid–latitude oceans being relatively warm at that time (*Kukla*, 2002). However, there are still debates about the exact phases and shifts between

continental vegetation records and marine sediment cores at the end of the Last Interglacial (*Turner*, 2002).

Ages derived from U/Th dated uplifted coral terraces from *Hawaii*, *Bahamas*, *Barbados*, *Haiti*, and the *Huon Peninsula* suggest that the sea level was at or above modern values until 117 kyr (*Stirling et al.*, 1995), which corresponds to the results from the *Vostok* record, where a relatively rapid temperature decline began at ~117 kyr to 115 kyr, and over the next 10 millennia, the temperature fell about 7 °C.

4 Climatic reconstruction from calcareous sinter

4.1 Reconstruction from high Alpine speleothems

4.1.1 Site description

The speleothems used for the reconstruction of the past climate were found in the high Alpine *Spannagel Cave*. It is located in the *Zillertal Alps* (*Western Tauern Window*), about 30 km south–east of Innsbruck, Austria. The cave stretches from an altitude between 2195 m and 2521 m a.s.l., and more than nine kilometers have so far been surveyed (*Spötl et al.*, in press).

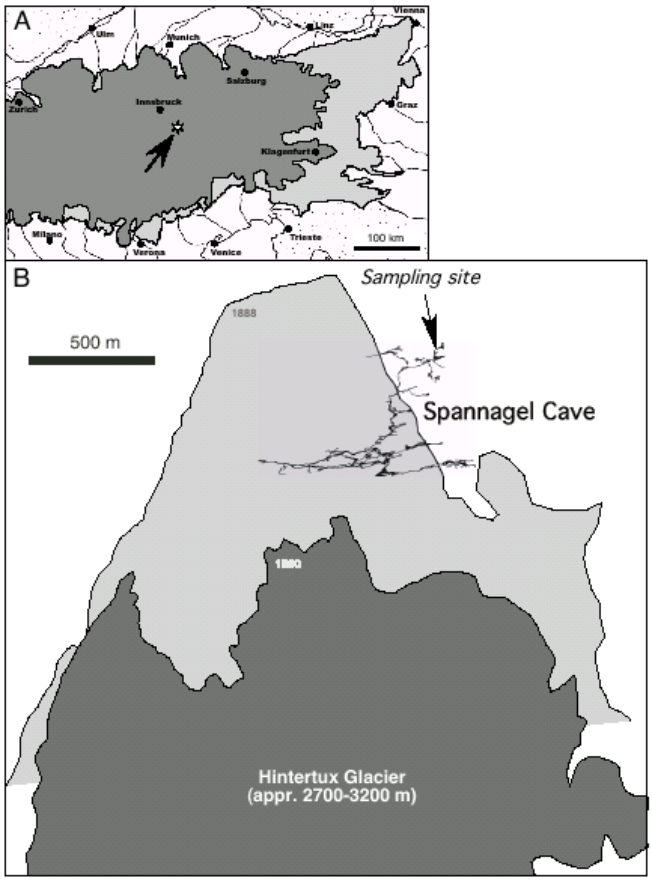

Fig. 4.1: A: Map showing the location of the *Spannagel Cave* in the *Zillertal Alps*, Austria. This site was well within the accumulation area of East Alpine glaciers during the Last Glacial Maximum (dark shaded area). **B:** The cave adjacent to the *Hintertux Glacier*, which partially covered the area above the cave during Little Ice Age (borders shown in light grey). (From *Spötl et al.*, 2002)

Geology

The cave consists of *Jurassic* calcitic marble, which is compressed between granitic gneisses. As the overlying *Zentral–Gneiss* is rich in uranium (3.4 to 12.0 µg/g), the respective concentrations in drip waters entering the cave (up to 33 ng/g) and in the speleothems (up to

300 µg/g) are extraordinary high. Speleothems in *Spannagel* are able to grow despite the absence of soil overlying the cave due to the presence of pyrite in the host rock. Local gypsum precipitates are revealing of its presence. Under oxidizing conditions, pyrite can transform into sulfuric acid (*Atkinson*, 1983):

[4.1] $$FeS_{2\ (solid)} + 3.5\ O_2 + H_2O \Rightarrow Fe^{2+} + 2\ SO_4^{2-} + 2\ H^+$$

[4.2] $$Fe^{2+} + 0.25\ O_2 + H^+ \Rightarrow Fe^{3+} + 0.5\ H_2O$$

[4.3] $$Fe^{3+} + 3\ H_2O \Rightarrow Fe(OH)_{3\ (solid)} + 3\ H^+$$

The acid dissolves the primary limestone, which produces excess CO_2 in the interstitial atmosphere; this leads to CO_2–degassing of the solution in the cave atmosphere and results in the formation of supersaturated carbonate solutions and calcite precipitation. Nevertheless, *Spannagel Cave* is only rarely decorated with speleothems, such as soda straws, stalactites, helictites, stalagmites, flowstones, moonmilk, and spar. All of them are generally of small size, and only a few are actively growing. The stalagmites and flowstones consist of coarsely–crystalline columnar low–Mg calcite. Detrital components, such as organic material or dust particles, are rare and – together with the high U concentrations – allow for high dating accuracy. Coarse sand and gravel and rounded cobbles of granitic gneiss at the cave floor suggest that high energy water flow was present during the cave development.

Climate

At present, the area above *Spannagel Cave* is ice–free, but was covered by the nearby *Hintertux Glacier* during glacials. Snow covers the cave during 8 to 10 months of the year. The interior cave temperature (at present +1.2 °C to +1.8 °C, depending on the location within the 10 km cave system) corresponds closely to the mean annual external air temperature of –1 °C at the main entrance (upper end of the cave) and +2.4 °C at its lower end and shows no daily or seasonal variation. As speleothems can only develop above freezing point, their growth in *Spannagel Cave* is very sensitive to temperature shifts. The relative humidity is higher than 96 %, and condensation droplets are sporadically detectable. A slight upward airflow is present during the winter season and a reversed flow in the summer season. Concentration of CO_2 is only slightly higher than in the external atmosphere at this altitude (285 ppmv) and shows only minor variations in different parts of the cave (*Spötl et al.*, in press).

4.1.2 Reconstruction of the Last Interglacial

Growth periods

A previously studied flowstone from *Spannagel Cave*, *SPA 52*, has provided data from MIS 7 and MIS 5e (*Spötl et al.*, 2002). It was dated via TIMS at 27 points along its growth axis. The beginning of the Last Interglacial was dated at 135.0 ±1.2 kyr and the Eemian lasted until 116.0 ±1.9 kyr (fig. 4.2).

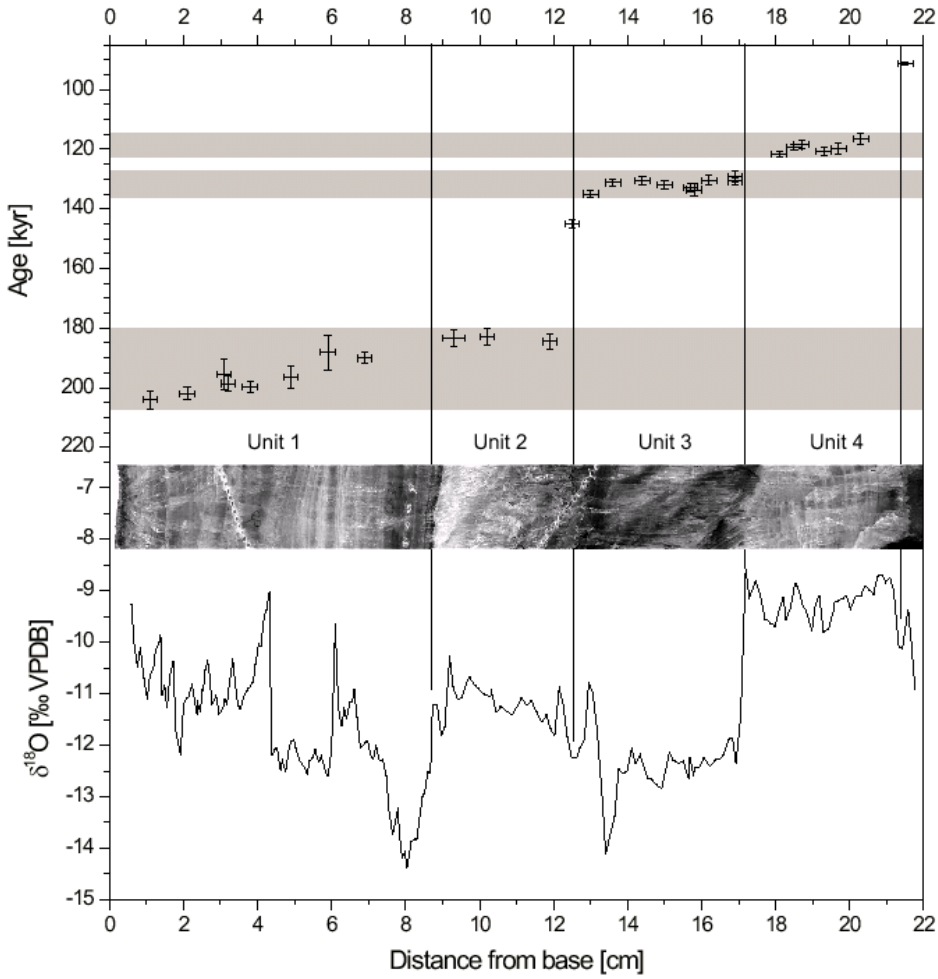

Fig. 4.2: U–series data and $\delta^{18}O$ profile of flowstone *SPA 52* (from *Spötl et al.*, 2002).

An unconformity within the MIS 5e section of the flowstone indicates a cessation of calcite deposition from 129.2 ±1.8 kyr to 121.8 ±0.9 kyr, separating the two growth units "U3" and "U4". This boundary was denoted as "H3" (Hiatus 3) in *SPA 52*. The growth intervals indicate periods with temperatures, which were similar or slightly higher than today, allowing for speleothems to form in this high–altitude cave setting. As the MIS 5e interval is represented by a section of only 82 mm thickness, the resolution is comparably poor. Thus, an additional speleothem from *Spannagel Cave* was studied: the 252 mm long stalagmite *SPA 50*, which developed only a few meters away from flowstone *SPA 52* and was found lying on the cave floor detached from its substrate. 22 subsamples along the growth axis of stalagmite *SPA 50* were taken for U/Th age determination. Due to the higher growth rate of *SPA 50* in comparison to *SPA 52*, we were able to obtain a record with a higher temporal resolution. It is characterized by a macroscopic hiatus about 25 mm above its base (fig. 4.3).

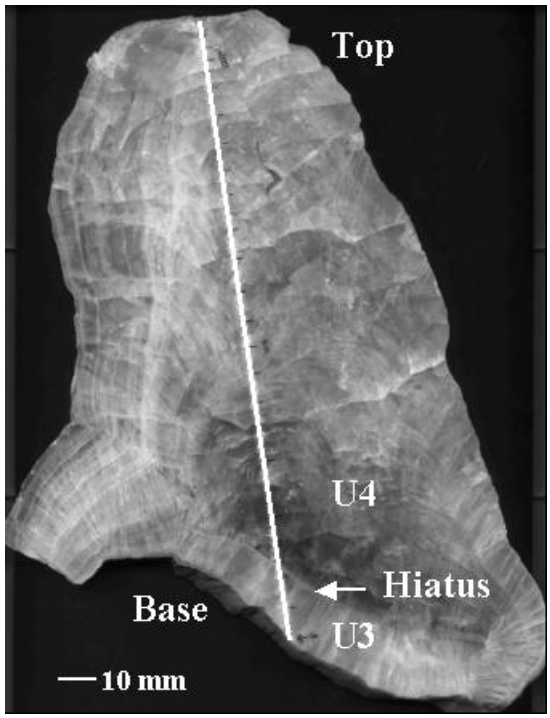

Fig. 4.3: Cross section of stalagmite *SPA 50*. The total height is 252 mm, the hiatus H3 is 25 mm above the base. It separates the lower part (U3) with the higher ^{238}U and ^{232}Th concentrations from the upper part (U4) with the comparatively lower respective concentrations. U–series datings and stable isotope analyses were performed along the growth axis (white line) in 150 µm intervals.

The hiatus separates the lower section, labelled U3, with ^{238}U concentrations of about 70 µg/g, from the middle and upper section with about 3.5 to 8.5 µg/g (U4) (fig. 4.3). Similar concentrations were found in the respective sections of flowstone *SPA 52*. The lowermost 25 mm have a darker color and a significantly higher ^{232}Th concentration of about 20 ng/g than the main section of the stalagmite (1 to 5 ng/g), which is still too low to have an influence on the age determination by detrital contamination.

The first depositional phase of *SPA 50* (U3) was dated at 130.5 ± 1.1 kyr and 130.2 ± 1.2 kyr. Thus, the growth of stalagmite *SPA 50* commenced 4.5 kyr later than that of flowstone *SPA 52*, indicating the presence of water on the ground of this cave chamber prior to ceiling water seepage. After a growth cessation marked by the macroscopic hiatus and a step in the age–depth profile, calcite deposition commenced again at 125.6 kyr (U4), and the youngest point was dated 118.2 kyr. One dated point with an age of 128.3 ±1.3 kyr from *SPA 50* is interpreted as a mixing age due to the short distance from the hiatus and therefore was excluded from the following interpretation. U4 in stalagmite *SPA 50* is represented by 19 dated points and shows two growth reductions around 123.8 kyr and 120.1 kyr, subdividing U4 into three subunits U4a, U4b, and U4c (fig. 4.4). Ages obtained from the top calcite of the adjacent flowstone sample *SPA 52* are scattered around the values of U4b and U4c, where the two respective growth reductions are not visible, probably due to the lower temporal resolution. However, the youngest age of the Last Interglacial is recorded by *SPA 52* at 116.0 ± 1.9 kyr, because the upper part of stalagmite *SPA 50* has a lower temporal resolution.

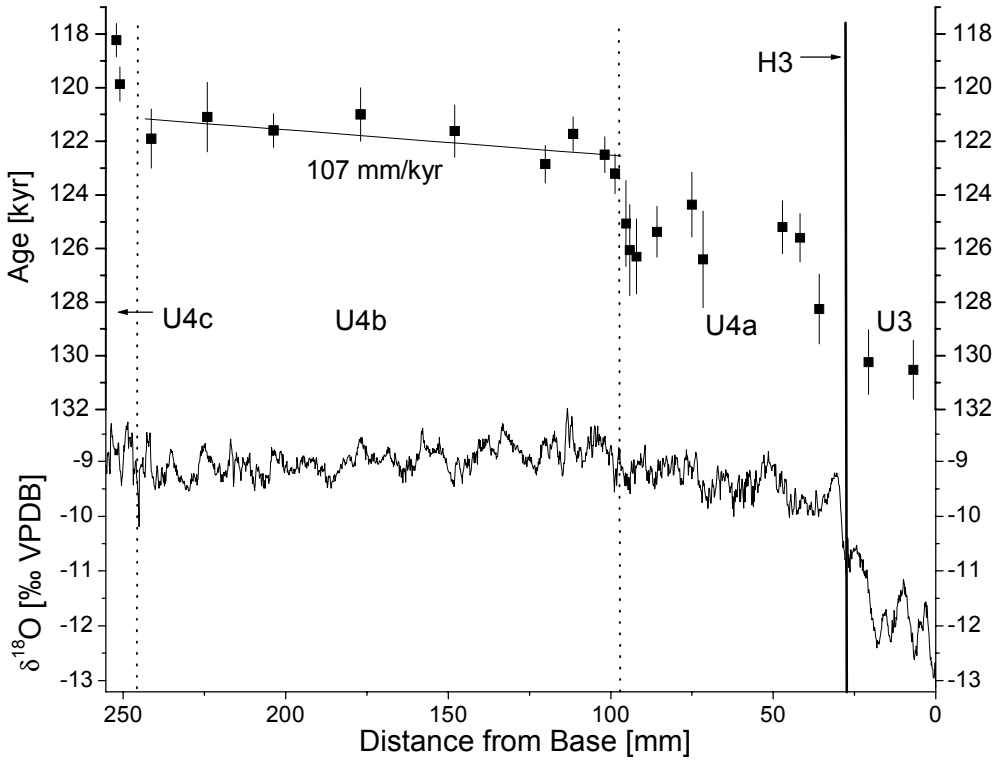

Fig. 4.4: $\delta^{18}O$ profile of stalagmite *SPA 50* and U–series ages with 2σ errors. The vertical line indicates the position of hiatus H3 separating growth units U3 and U4. Growth unit U4 is subdivided into three subunits, U4a, U4b, and U4c. They are separated by sections of reduced growth at about 97 mm and 246 mm from the stalagmite base (dotted lines). Also shown is the error–weighted linear fit through the 9 dated points of U4b used for the determination of growth rate (107 mm/kyr) and spectral analysis.

Provided that the growth interruptions around 130.2 kyr, 123.8 kyr, and 120.1 kyr recorded by the U/Th dates of *SPA 50* are not the product of incidentally changed flow paths of the drip water, they resultantly represent cold spells when mean annual temperatures were at least 1 to 2 °C lower than today. A number of other climate archives also show the existence of cooler but not glacial periods during the Last Interglacial (*Frogley et al.*, 1999, *Fronval and Jansen*, 1996, *Hearty and Neumann*, 2001, *Linsley*, 1996, *Sanchez-Goni et al.*, 1999, *Stirling et al.*, 1998, *Thouveny et al.*, 1994, *Wilson et al.*, 1998) (see also chapter 3.2.2).

In figure 4.5 we show the growth periods and isotopic age profile of *SPA 50*. It is based on an age model consisting of linear, error–weighted fits through the dated points. For U3 we determined a growth rate of 48 mm/kyr. The 17 points of U4a and U4b were put together in order to overcome the uncertain depth age relationship of U4a, entailing a rate of 37 mm/kyr. For the beginning of U4c the youngest model age of U4b has been used as a tie point in addition to the two dated points of U4c resulting in a growth rate of 3 mm/kyr.

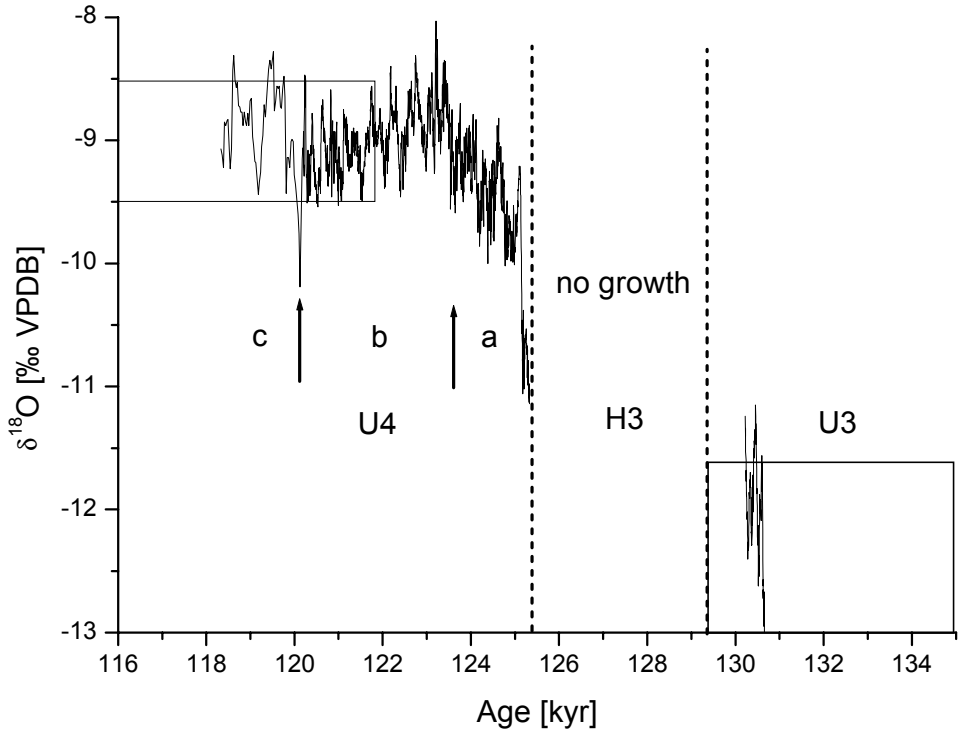

Fig. 4.5: $\delta^{18}O$ profile of stalagmite *SPA 50* versus age derived from TIMS measurements shown in fig. 4.4. The two arrows within U4 mark the position of the hiatuses both seen in the age–depth and in the $\delta^{18}O$ profile. The open boxes indicate the age and $\delta^{18}O$ range of flowstone *SPA 52*.

Stable isotopes

During growth phase U3, $\delta^{18}O$ values in both samples range between –13.0 ‰ and –11.0 ‰ VPDB, except for the older part of *SPA 52* with fluctuations from –10.7 ‰ to –14 ‰. The beginning of U4 is marked by a significant increase of $\delta^{18}O$ to values of around –9.5 ‰ in both samples. It has been argued earlier, that the difference of 2 ‰ to 3 ‰ in $\delta^{18}O$ between sections U3 and U4 may not convincingly be explained by a temperature increase, and is more likely to be ascribed to a change in water sources (*Spötl et al.*, 2002). This means that the more negative isotopic values in U3 reflect a larger contribution of melt waters from the nearby glacier. The glacier retreat led to a stronger influence of precipitation on drip waters in the cave, leading to the $\delta^{18}O$ values becoming markedly heavier.

The $\delta^{18}O$ values of U4 correspond roughly with the values of Holocene speleothems from *Spannagel Cave*. Stalagmite *SPA 12* for example shows recent calcite values around –7.8 ‰, in equilibrium with $\delta^{18}O$ values of -11 ‰ VSMOW in precipitation (*Spötl et al.*, in press). The difference of about 1 ‰ to 2 ‰ in comparison to the recent calcite would result in temperatures being 4 to 8 °C higher than today, if utilizing the temperature dependence of isotope fractionation during calcite precipitation of –0.24 ‰/°C (*Friedman et al.*, 1977). However, this difference may not solely be explained by a temperature effect. Instead we may ascribe it either to more negative $\delta^{18}O$ values of precipitation or to a larger contribution of melt water of the glacier in comparison to the Holocene.

During the Eemian, the profile of $\delta^{18}O$ in U4a of *SPA 50* increased from –9.7 ‰ to –9.1 ‰, and in U4b the $\delta^{18}O$ values show a slight downward trend from –8.8 ‰ to –9.2 ‰. The boundary between U4b and U4c is marked by a negative spike in the $\delta^{18}O$ values down to –10.3 ‰, which may indicate a relapse to colder conditions with an augmented contribution of glacial melt water in the cave. High amplitude variations of 1 ‰ mark the uppermost part U4c before the growth comes to an end. Presumed that $\delta^{18}O$ precipitation values remained constant during the Eemian, it can be deduced from the 0.9 ‰ difference in $\delta^{18}O$ values that variations in the range of 4 °C occurred, with higher temperatures at the beginning (U4a) of this period.

The short term variations in $\delta^{18}O$ of ± 0.5 ‰ in sections U4a, U4b, and U4c of stalagmite *SPA 50* probably reflect both the fluctuations in temperature inside the cave, influencing the fractionation coefficient of calcite precipitation, and variations of the $\delta^{18}O$ precipitation values. These may have been caused by any combination of the following factors: temperature effect, amount effect, changed seasonality of rainfall, or alterations in storm and cloud tracks in the Central Alps. This latter effect has been investigated earlier (*Florineth and Schlüchter*, 2000) and it is assumed that during colder periods the prevailing westerly circulation pattern over Central Europe is displaced by an augmented southerly wind component from the Mediterranean. From the data of this study it is not possible to deduce exact temperature shifts from the stable isotope variations or to determine the contributions of the above mentioned processes. Additional investigations, such as fluid inclusion analyses and modelling of stable isotopes in precipitation will help to quantify the influences of the suggested processes.

Spectral analysis

The uniquely high resolution of the $\delta^{18}O$ profile in U4b allowed to perform a spectral analysis in order to determine the periodicities of the isotope fluctuations. Therefore, the growth rate of U4b was determined separately and a growth rate of 107 mm/kyr was gained. $\delta^{18}O$ values from other sections of the stalagmite have not been used due to the lower resolution and the lack of a reliable age model derived from the dated points. The $\delta^{13}C$ profile does not show any significant correlation with the $\delta^{18}O$ record or with the cycles seen within the $\delta^{18}O$ data and has therefore been excluded from any further discussion at this stage. The database consists of the $\delta^{18}O$ values of U4b with ages derived from an error–weighted linear fit through the U–series dated points (fig. 4.4). A correlation coefficient of the fit function of 0.66 was determined. The distance between two analyzed points of the high resolution portion U4b is 0.15 mm or 1.4 years, according to the age model. Thus, it is unlikely that the resulting peaks are an artefact of a “seasonality effect” that would generate a pseudo–cyclicity in the stable isotope record. Figure 4.6 shows the spectral analysis results.

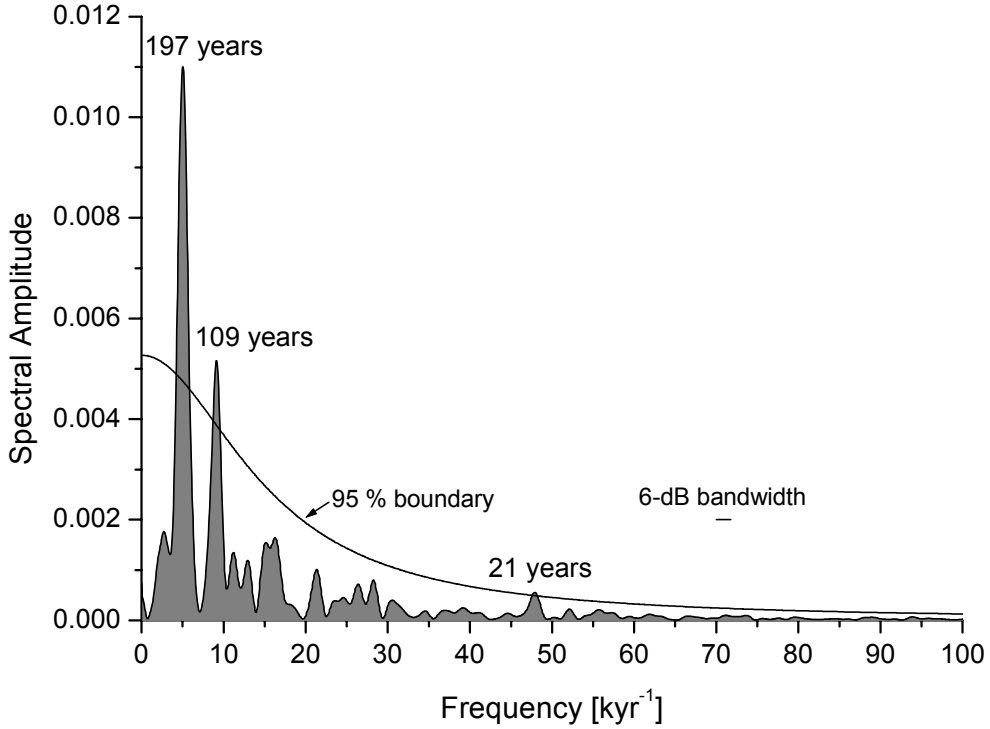

Fig. 4.6: Spectral analysis results of stalagmite *SPA 50*. Spectral analysis for the high resolution interval U4b (*Priestley*, 1981, *Schulz and Mudelsee*, 2002). Spectral amplitude was estimated using the *Lomb–Scargle Fourier Transform* for unevenly spaced data, a *Welch I* window and two overlapping (50 %) segments; red–noise boundary was estimated as upper 95 % chi–squared limit of a fitted *AR1 process*. High time–resolution and uneven spacing prohibit effectively against aliasing effects.

Three peaks exceeding the 95 % significance boundary are present at 197, 109, and 21 years. They are close to the well–established *Suess Cycle* (206 years periodicity), *Gleissberg Cycle* (89 years), and *Double Sunspot Cycle* (22 years) derived from Holocene $\Delta^{14}C$ and suggest that external forcing influenced the climate during the Eemian, at least within the analyzed unit U4b. The difference between the observed and Holocene $\Delta^{14}C$–derived cycle lengths can be explained by the uncertainty of the growth rate determination and by the spectral analysis uncertainty, expressed by the 6 db–bandwidth. Nevertheless, cycle lengths are also subject to changes, as has been demonstrated via dust records from the GISP2 ice core (*Ram and Stolz*, 1999). In the Holocene, North Atlantic marine sediments reveal a strong correlation between solar induced variations in ^{10}Be and ^{14}C and variations in surface winds and surface ocean hydrography on centennial to millennial timescales (*Bond et al.*, 2001). Two Holocene stalagmites from *Sauerland*, Central Germany, support the finding of a connection between solar activity and climate in Central Europe: the $\delta^{18}O$ values of stalagmites *B7-7* and *AH1* show a strong correlation with the solar induced $\Delta^{14}C$ (*Niggemann et al.*, 2003, *Niggemann et al.*, 2002). As the climate of Central Europe is mainly influenced by the North Atlantic, the high resolution record *SPA 50* suggests that solar activity modulated the high Alpine climate during the Eemian on decadal to centennial timescales in the same way. The mechanism linking solar output variations to tropospheric climate oscillations is still uncertain. One

possibility is that variations in the intensity of Galactic Cosmic Rays in the atmosphere causes changes in cloudiness. Another mechanism suggests that UV–irradiance variations affect ozone, which changes the temperature and wind pattern in the stratosphere, in turn altering tropospheric climate (*Carslaw et al.*, 2002, *Rind*, 2002).

Conclusion

The high–resolution study of stalagmite *SPA 50* and flowstone *SPA 52* from the Central Alps reveals a warm phase prior to the classical Eemian from ~135 to 130 kyr. The ambient temperature during the Eemian, from 125.6 ± 0.9 kyr to 116.0 ± 1.9 kyr, was at least as high as today in this region. This dataset provides a precise time frame for other continental climate archives for the duration of the Eemian. The growth reductions of stalagmite *SPA 50* at about 123.8 kyr and 120.1 kyr could be the product of cold spells, during which the annual mean temperature was at least 1 to 2 °C lower than today. The spectral analysis' results reveal solar forcing of the Eemian climate.

4.1.3 Reconstruction of the past 250 kyr

An additional speleothem from *Spannagel Cave* was studied, *SPA 59*, which is a several square meters wide flowstone and grew during the warm phases corresponding to MIS 7, 5e, 5a ,and 3 (fig. 4.7).

Fig. 4.7: Slice of flowstone *SPA 59*. The black scale bar indicates the growth axis. Numbers give the distance from the top in cm. Note the multiple hiatuses representing periods of growth interruptions.

37 subsamples along the growth axis of flowstone *SPA 59* were taken for U/Th age determination (see also table A.2). The difficulty of dealing with a low growth rate archive was solved by using minimal amounts of sampling material of less than 100 mg. Owing to the extraordinary high U concentrations of up to 171 µg/g and low detrital Th contamination, high resolution U/Th dates with little dating uncertainty of 0.4 % to 2.4 % of the yielded ages could be obtained. Prominent hiatuses are found along the entire section of the flowstone, which, according to the dating results, are accompanied by steps in the depth–age profile as well as by local minima in the stable isotope record (fig. 4.8).

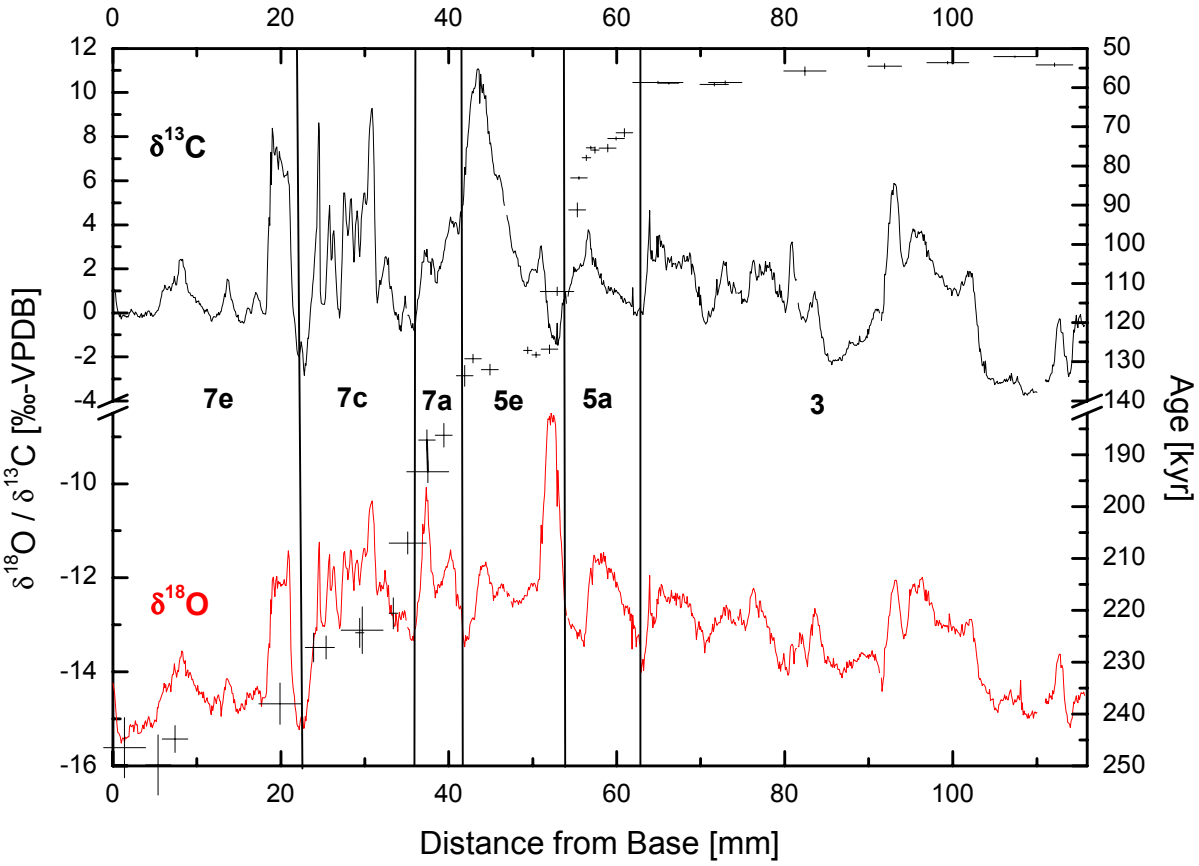

Fig. 4.8: Stable isotope profile and dating results of flowstone *SPA 59*. The U/Th–ages are given with 2σ errors. The error bars in x–direction indicate the insecurity of correlating the track of the stable isotope profile to the track along which the U/Th samples have been taken. The $\delta^{18}O$ profile is shown as a red curve, the $\delta^{13}C$ profile as a black curve. The subdivision of the flowstone into MIS 7e, 7c, 7a, 5e, 5a, and 3 is based both on the steps in the age profile and on prominent minima of the stable isotope profiles.

The formation of sinter indicates temperatures above the freezing point at this high Alpine site, as previously mentioned in chapter 4.1.1. Therefore, the flowstone serves as a good record of warm periods, which were associated with the Marine Isotope Stages of the *SPECMAP* time scale (*Imbrie et al.*, 1984). The growth phases reproduce the main features of other paleoclimatic reconstructions, but also illustrate some important differences (fig. 4.9).

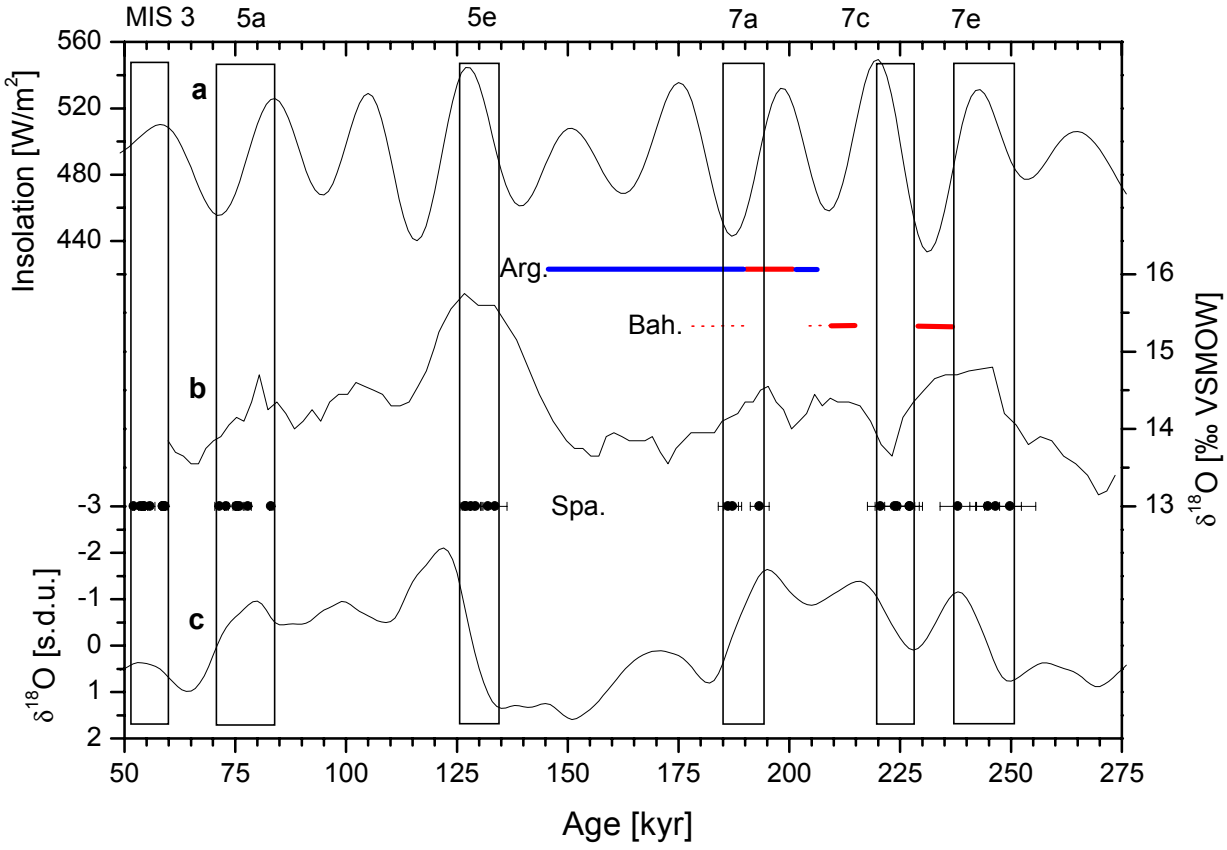

Fig. 4.9: Growth phases of flowstone *SPA 59* from *Spannagel Cave* (open boxes) compared with 60°N summer insolation (**a**), the $\delta^{18}O$ record from groundwater calcite at *Devils Hole*, Nevada (*Winograd et al.*, 1992) (**b**), and the stacked $\delta^{18}O$ record from marine calcite (*SPECMAP*) (*Imbrie et al.*, 1984) (**c**). Also shown are the 34 U–series dated points with 2σ error bars, 3 additional points interpreted as mixing ages have been omitted. Growth phases of a submerged stalagmite from *Argentarola Cave* (Italy) are indicated by the blue horizontal bar (*Bard et al.*, 2002), representing a sea level of less than –18 m in comparison to the present value; the interfering red bar indicates that the sea level was above this value (warm climate). Warm stages derived from U/Th dated slope sediments from the Bahamas (*Robinson et al.*, 2002) are indicated underneath (red bar/dots).

Apart from MIS 5c, all the other warm phases were found and some important paleoclimatic information is provided, especially for MIS 7, where absolutely dated records are rare (*Robinson et al.*, 2002).

MIS 7

The growth of flowstone *SPA 59* commences at 249.8 ± 5.8 kyr and continues until 238.0 ± 4.0 kyr. This first growth phase is assigned to MIS 7e. No macroscopic hiatus is visible within this section. The onset of MIS 7e, the so–called Termination III, as early as 249.8 ± 5.8 kyr is in general agreement with the results from the U/Th dated vein calcite core from *Devils Hole* (*Winograd et al.*, 1992), but it conflicts with the 60°N summer insolation, which has a minimum at 253 kyr and only starts to increase at 250 kyr. Thus, it is doubtful if the insolation was the major forcing agent, which initiated the penultimate interglacial. U/Th–ages derived

from *Bahamas* slope sediments suggest that the peak of MIS 7e lasted from ~237 kyr to 228 kyr (*Robinson et al.*, 2002), which is markedly later than what is derived from *SPA 59*. One possible explanation for the discrepancy between these records could be the time lag of 14 ± 5 kyr between the first warming of the atmosphere due to changes of orbital parameters and a substantial ice sheet melting that lowers marine $\delta^{18}O$ (*Shackleton*, 2000). Similar time lags on the order of 10 to 15 kyr have been given for the transition period from the *Last Glacial Maximum* (~20 kyr ago) to the Holocene sea level highstand (*Lambeck et al.*, 2002), which would explain the observed time gap. Whether the subsequent gap of flowstone formation observed between 238 ± 4.0 kyr and 227.1 ± 2.2 kyr is a result of a temperature drop at this high Alpine site or represents changed hydrological conditions remains unclear. However, both the solar summer insolation values and the marine *SPECMAP* curve show a markedly transition to colder conditions with a reduced sea level at that time, whereas the $\delta^{18}O$ values of the *Bahamas* slope sediments indicate interglacial conditions.

Above a distinct grayish hiatus, the growth of flowstone *SPA 59* continues from 227.1 ± 2.2 kyr to 220.6 ± 3.0 kyr, indicating that ice–free conditions prevailed in *Spannagel* during this period. Whether this growth interval represents MIS 7c or should rather be assigned to MIS 7e is debatable. The respective section is characterized by a couple of faint–whitish hiatuses, the ages of which could not be determined by the U/Th dating. The subsequent dated point with an age of 207 kyr is interpreted as an artefact of mixing due to the short distance from the next hiatus. According to both the *Devils Hole* record and the *Bahamas* sediment core, MIS 7c commences at 215 kyr, about 5 kyr later than defined by the *SPECMAP* curve. The time gap between our record and the *Bahamas* sediments of about 12 kyr could be explained via the ice sheet time constant, as suggested for the beginning of MIS 7e. It does, however, not explain the gap with the *Devils Hole* chronology; the onset and termination of MIS 7c in the *Devils Hole* calcite is constrained by only two data points, confining the significance of the derived timing. Both the *Devils Hole* record and the sea level record derived from submerged speleothems from *Argentarola Cave* (Italy) (Bard *et al.*, 2002) place the end of MIS 7c at about 206 kyr, 14 kyr later than according to the *Spannagel* record. Again, the absence of speleothem growth in *Spannagel* does not necessarily imply colder conditions, but may also be the result of changed hydrology in the cave chamber.

Similarly to the MIS 7e/7c boundary, the border between MIS 7c and 7a is marked by a distinct hiatus in *SPA 59*, where calcite deposition recommences at 193.3 ± 2.1 kyr. MIS 7a is represented by a section 6 mm in length and the youngest age of MIS 7a was dated at 186.2 ± 2.3 kyr. The beginning of MIS 7a is concordant with results from the *Devils Hole* and *SPECMAP* record, which both peak when speleothem growth commences at 193.3 ± 2.1 kyr. However, an earlier start at 202 kyr has been recorded from the submerged speleothems from *Argentarola Cave*, and another speleothem from *Spannagel Cave*, *SPA 52*, yielded ages between 207 and 180 kyr (*Spötl et al.*, 2002). This finding suggests that, due to the low resolution, the dating of flowstone *SPA 59* produces ages of the main parts of each warm phase rather than the exact timings of the onsets and terminations. The youngest date of MIS 7a is 186.2 ± 2.3 kyr, slightly later than expected from the *SPECMAP* curve, which at 190 kyr is half way to its minimum. But it is earlier than the date derived from *Bahamas* slope sediments, which places the end of MIS 7a at 178.4 kyr.

For MIS 7 the results of the *SPA 59* dating show marked differences between the timing of the interstadials derived from both the orbitally tuned *SPECMAP* curve and from absolutely dated climate archives. Furthermore, we can not derive any systematic shifts in comparison to the other records. We attribute this finding to the low resolution of the *SPA 59* record as well as to the partially uncertain or small number of dates of the other records.

MIS 5

The section corresponding to MIS 5e is represented by a thin porous layer of about 12 mm thickness and is therefore not suitable for high resolution investigations of the Last Interglacial, as was the case for flowstone *SPA 52* and stalagmite *SPA 50* retrieved from *Spannagel Cave* (*Holzkämper et al.*, submitted). The section can be subdivided into four distinct layers of about 3 mm thickness each. The first (oldest) and third layer consist of translucent clear calcite, the second one of brownish opaque carbonate, and the uppermost (youngest) unit is characterized by a porous multiple layering. In general concordance with *SPA 50* and *SPA 52*, the deposition commenced at 133.6 ± 2.7 kyr (first layer). The youngest point of the MIS 5e section yielded an age of 126.8 ± 1.1 kyr (third layer). The fourth layer, probably representing the "classical Eemian" (see chapter 3.2.1), wasn't dated due to the high porosity and small–scale sub–layering, comprising the risk of U–exchange processes and yielding artificial mixing ages. In agreement with a series of other absolutely dated climate archives (*Esat et al.*, 1999, *Gallup et al.*, 2002, *Henderson and Slowey*, 2000, *Spötl et al.*, 2002, *Winograd et al.*, 1992), the beginning of MIS 5e was dated earlier than suggested by the *SPECMAP* curve, at 133.6 ± 2.7 kyr. This age may be interpreted as the lower limit for the initiation of MIS 5 because of the low resolution of our record. Thus, it confirms the earlier finding of an investigation of speleothems from *Spannagel Cave*, which revealed an early onset of MIS 5e at 135 kyr (*Spötl et al.*, 2002). Such an early onset of MIS 5e is difficult to explain with increased 60°N summer insolation, which peaks at 128 kyr. A further subdivision of MIS 5e, as has been performed in *Holzkämper et al.*, submitted, could not be carried out from the *SPA 59* dating, but a series of macroscopic hiatuses suggests that the Last Interglacial was interrupted by several cool events. Furthermore, the absence of the classical Eemian in this record, which lasted from ~126 kyr until 116 kyr, is interpreted as a consequence of the presumably large amounts of water that flushed through the cave chamber, hindering the calcite precipitation on our flowstone, instead leaving a thin porous layer behind. This circumstance reveals the exceptional status of the Last Interglacial in comparison to other warm periods of the past 250 kyr.

A layer of 9 mm thickness above the Eemian section represents the interstadial 5a, yielding ages from 83.1 ± 0.4 kyr to 71.5 ± 1.1 kyr. The insolation curve shows a maximum at 84 kyr, followed by a minimum at 71 kyr, suggesting that northern summer insolation influenced this growth period. Two points in close proximity to the hiatus ensuing the porous section of the Eemian, which were dated at 112.0 kyr and 91.2 kyr, are interpreted as mixing ages and have therefore been excluded from the interpretation.

MIS 3

The youngest growth phase of flowstone *SPA 59* can be assigned to MIS 3, yielding ages between 58.9 ± 0.2 kyr and 52.1 ± 0.2 kyr. This part contains two faint brownish bands, around 8 more of which have accumulated at the uppermost section of the flowstone with vertical distances smaller than 1 mm. Owing to the greater size of this section in comparison to the other parts of the flowstone, the temporal resolution is significantly higher. For the lower 40 mm of the 53 mm long section, a growth rate of approximately 6 mm/kyr was calculated. However, the calculated growth rate is still low when compared to stalagmite *SPA 49*, which has earlier been studied (*Spötl and Mangini*, 2002). Its overall height of 30 cm recorded an interval from 57 kyr to 46 kyr, thus the mean growth rate is about 27 mm/kyr. A comparison between the $\delta^{18}O$ profiles derived from both speleothems reveals a general concordance (fig. 4.10). The slight discrepancy in the absolute timing and duration of "isotope events" may be attributed to the lower resolution of flowstone *SPA 59*, which was dated at 8 points within this interval, whereas stalagmite *SPA 49* had been dated at 14 points. In *SPA 49*, the $\delta^{18}O$ peaks had been compared to the GRIP ice core isotopes (*Johnsen et al.*, 2001) and it was concluded, that they may well be associated to the *DANSGAARD/OESCHGER–Events* of the North Atlantic.

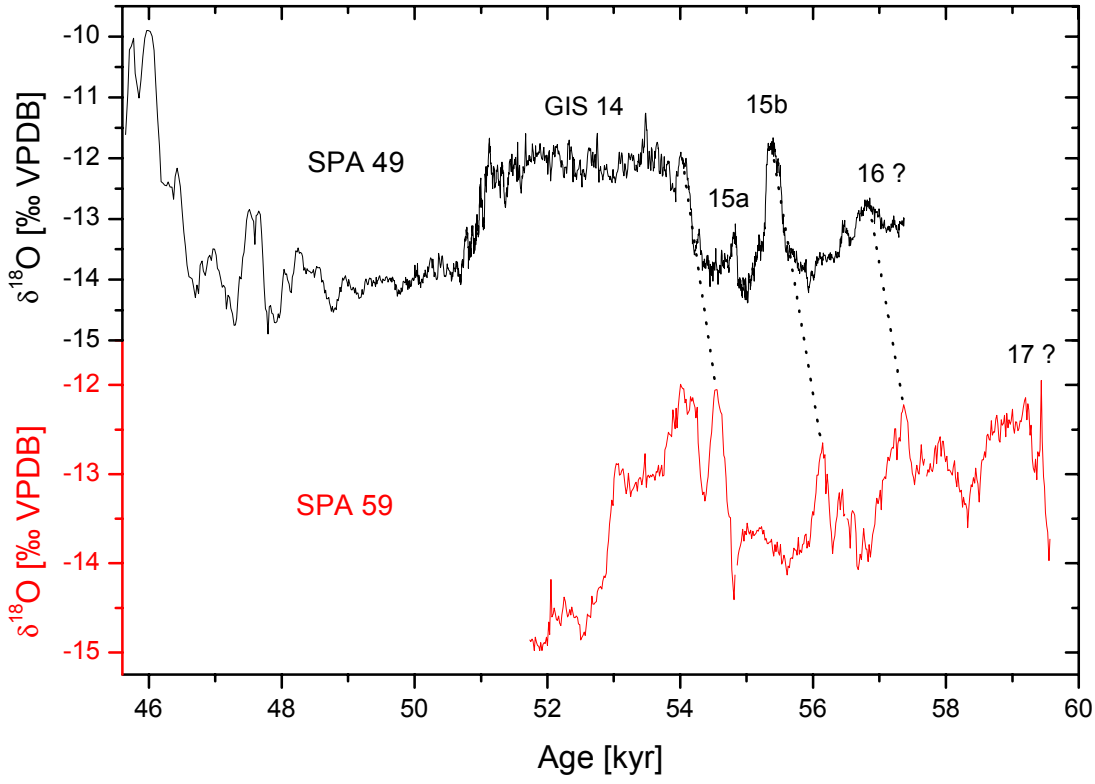

Fig. 4.10: Comparison of MIS 3 $\delta^{18}O$ values between stalagmite *SPA 49* (black curve) (*Spötl and Mangini*, 2002) and flowstone *SPA 59* (red curve). The numbers refer to the Greenland Isotope Stages (GIS) recorded in the GRIP ice core (*Johnsen et al.*, 2001).

Generally, when viewing the timing of the growth periods equivalent to MIS 5a and MIS 3, the theory of orbital climate forcing seems to be corroborated, as speleothem growth sets in when northern summer insolation is at its maximum. However, when examining the overall

timing of speleothem growth intervals in *Spannagel Cave*, we can not find any concordance with northern summer insolation, with growth during peak insolation values (MIS 7e), at minimum values (MIS 7a), during rising values (MIS 7c, MIS 5e), or during decreasing values (MIS 5a, MIS 3) (fig. 4.9 and fig. 4.11). Thus we conclude that an additional trigger must have been involved in initiating climate variations over the past 250 kyr. A comparison between the growth phases of speleothems from *Spannagel Cave* and from Oman with the flux of galactic cosmic rays derived from ^{10}Be of deep sea sediment cores has shown that there is a link between the strength of the Earth's magnetic field and the Earth's climate during the past 200 kyr (*Christl et al.*, in press) (fig. 4.11). Whether this is confirmed by the reconstruction of the Earth's magnetic field during the sub–stages MIS 7e and MIS 7c is currently being investigated (*Christl et al*., in preparation).

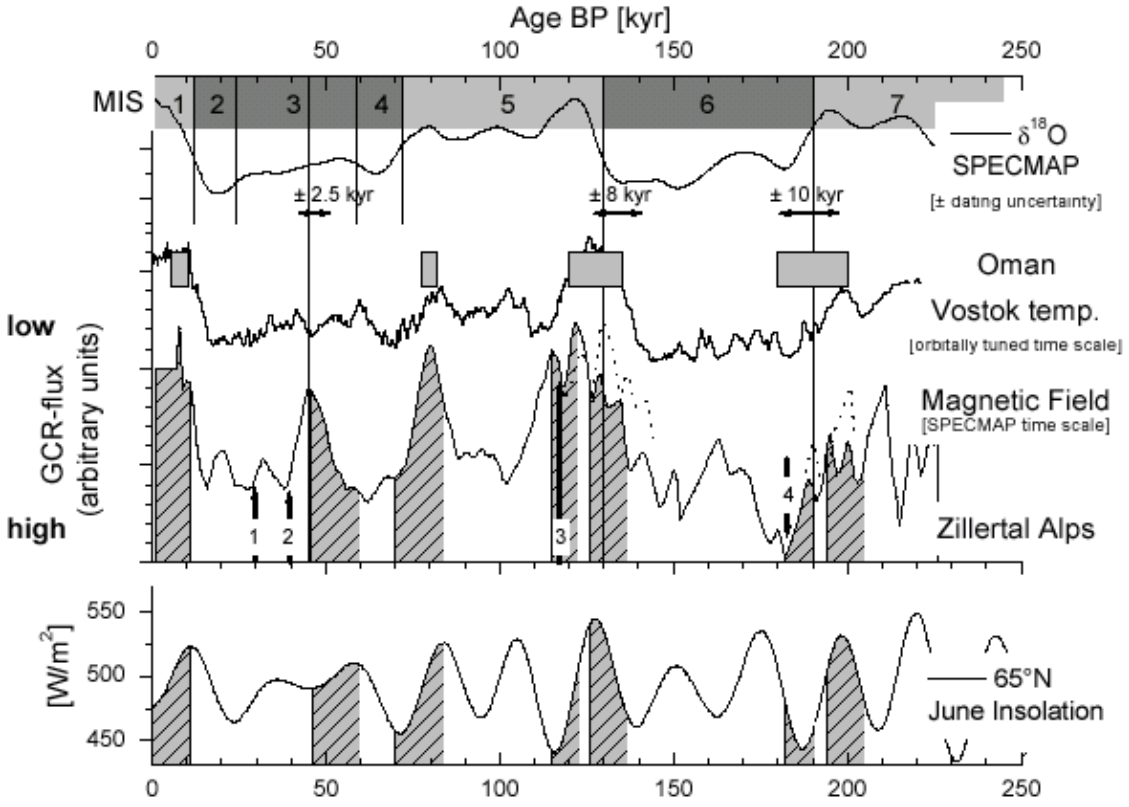

Fig. 4.11: From top to bottom: The *SPECMAP* curve (*Martinson et al.*, 1987) including its dating uncertainty; *Vostok* temperature record (orbitally tuned time scale); reconstructed geomagnetic paleointensity (*Christl et al.*, in press) interpreted as a record of galactic cosmic ray (GCR)–flux over the last 200 kyr based on the *SPECMAP* chronology; the dashed line shows the GCR–record on an adjusted timescale including the shift of the *SPECMAP* chronology (+8 kyr around 130 kyr and –10 kyr around 190 kyr). The vertical arrows indicate maxima in the GCR-flux that are associated with global geomagnetic events:1 *Mono Lake* (~32 kyr), 2 *Laschamp* (~40 kyr), 3 *Blake* (~117 kyr), 4 *Biwa I / Jamaica* (~187 kyr). Lower part: northern summer insolation. The shaded areas indicate growth periods of speleothems in Northern Oman and in the Central Alps. (From *Christl et al*., in press)

The growth period between 47 to 57 kyr recorded in *Spannagel* has no counterpart in Oman. It is possible that this period was missed during the sampling campaigns in Oman, where only

a limited amount of specimens was sampled. Alternatively, the lack of speleothem growth in Northern Oman during this time period might indicate that the temperature was not high enough for a northward shift of the *ITCZ* (see also chapter 4.2.1).
The *SPA 59* dataset reveals that calcite deposition took place during all interglacial periods over the past 250 kyr, with the exception of MIS 5c. The reason for this may be a potentially strong glacial advance during the 5d stadial in the Alpine region, corresponding to a sea level drop of ~50 to 70 m (*Lambeck and Chappell*, 2001), resulting in the warming of MIS 5c being insufficient in length to produce ice free conditions above *Spannagel Cave*. Alternatively, MIS 5c may not have been as warm as other interstadials, as indicated by sea surface temperature reconstructions from North Atlantic sediments (*Kandiano et al.*, in press).

Stable isotopes

Both the $\delta^{18}O$ and $\delta^{13}C$ values show high variations distributed over the entire profile taken along the growth axis of the flowstone (fig. 4.8). A weak long–term trend is visible in the $\delta^{18}O$ profile, with a slight increase from about –15 ‰ VPDB at the bottom of the flowstone, corresponding to MIS 7e, to about –12 ‰ (MIS 5e) and –8.5 ‰ (classical Eemian) respectively, in the middle part, followed by a reduction to the initial values at the top of the flowstone. No long–term trend is visible for the $\delta^{13}C$ profile, with a mean value of around +1 ‰. The short term variability, with amplitudes of about 1 ‰ to 4 ‰ ($\delta^{18}O$) and about 3 ‰ to 11 ‰ ($\delta^{13}C$) respectively, is extraordinary high in comparison to other speleothems, and local minima of the stable isotope profile can be paralleled to the hiatuses. Consistent with the dating results, each section between two hiatuses represents a warm stage, and the hiatuses are marked both by steps in the depth–age profile and spikes in the stable isotope profile.
Three remarkable features characterize the stable isotope profile of flowstone *SPA 59*: (i) the partially high values of $\delta^{13}C$ of up to +11 ‰, (ii) a high variability with large amplitudes in both $\delta^{18}O$ and $\delta^{13}C$, and (iii) the extraordinary high correlation between both isotope ratios.
In *Spannagel*, the main process that leads to the formation of speleothems is the dissolution of the marble host rock by the presence of sulfuric acid evolved from the oxidation of the adjacent pyrite (see chapter 4.1.1). Alternatively, a slight increase in temperature that glacial melt waters experience upon their journey into the cave could have enabled speleothem growth (*Dreybrodt*, 1982), but as the temperature in the cave is only slightly higher than the long–term mean annual air temperature, this process is regarded as negligible. Owing to the sparse vegetation above the cave, the $\delta^{13}C$ values of the speleothems are mainly influenced by the host rock with values of +2 to +3 ‰. The extraordinary high $\delta^{13}C$ values of up to +11 ‰ must consequently be attributed to kinetic fractionation during carbonate precipitation.
$\delta^{18}O$ values in speleothems are influenced by the isotopic composition of the precipitation and by the conditions during which calcite is precipitated from the solution percolating into the cave. Presuming constant values in precipitation during each growth phase and equilibrium fractionation during calcite precipitation, the observed short–time variations of 1 ‰ to 4 ‰ would account for 4 to 16 °C temperature fluctuations, utilizing the temperature dependence of isotope fractionation during calcite precipitation of –0.24 ‰/°C (*Friedman et al.*, 1977). As

today's temperature in the cave is about +1.8 °C and speleothems can only grow above the freezing point, such temperature amplitudes seem unlikely. Therefore, factors other than temperature effects under equilibrium conditions must be responsible for such large variations. This consideration together with the simultaneous enrichment of $\delta^{18}O$ and $\delta^{13}C$ suggests that kinetic fractionation seems to be a likely explanation for the observed phenomena (*Hendy*, 1971). Generally, speleothems that formed under non–equilibrium conditions are less useful to derive paleo–environmental information than those formed under equilibrium conditions. Here, the strong correlation between $\delta^{13}C$ and $\delta^{18}O$ points towards a highly kinetical fractionation process during calcite precipitation. Tentatively, the degree of kinetical enrichment may be used as a qualitative measure of melting water amounts or temperature:

Kinetic isotope effects arise from the preferential loss of light isotopes of both C and O from the solution during rapid irreversible loss of CO_2 (*Schwarcz*, 1986). This implies that an enhanced degassing of CO_2 leads to an enrichment in both ^{13}C and ^{18}O in the precipitated carbonate. Which process was actually responsible for the augmented kinetical fractionation in the *Spannagel Cave* is uncertain and needs further investigation. One possible explanation could be enhanced degassing as a result of additional water entering the cave (indicating warm and humid conditions with more precipitation and/or melt water penetrating into the cave). Thus, the flow velocity would increase and the duration between the first contact of the groundwater with the cave atmosphere and calcite precipitation on top of the flowstone would have been shorter, so that the supersaturation of the solution in respect to the cave atmosphere CO_2–level would still be high. At times of reduced water flow (indicating cool and dry conditions) in the cave, a large portion of calcite precipitation would already have taken place before the solution reached the respective flowstone and the CO_2 partial pressure in the solution would be lower. The precipitated calcite would then be closer to isotopic equilibrium with cave atmosphere CO_2 (*Dulinski and Rozanski*, 1990). Additionally, both $\delta^{13}C$ and $\delta^{18}O$ values would decrease significantly in the direction of flow because of the heavier isotopes being preferentially removed (*Fantidis and Ehhalt*, 1970). As a consequence, low values of $\delta^{13}C$ and $\delta^{18}O$ would represent reduced flow velocity and long residence times in the cave, whereas high values would represent comparably short residence times owing to larger amounts of water entering the cave. This would explain why the $\delta^{13}C$ values started at low levels during all examined growth phases, peaked at the centers of the respective growth intervals, and dropped to low values at the end of the warm phases.

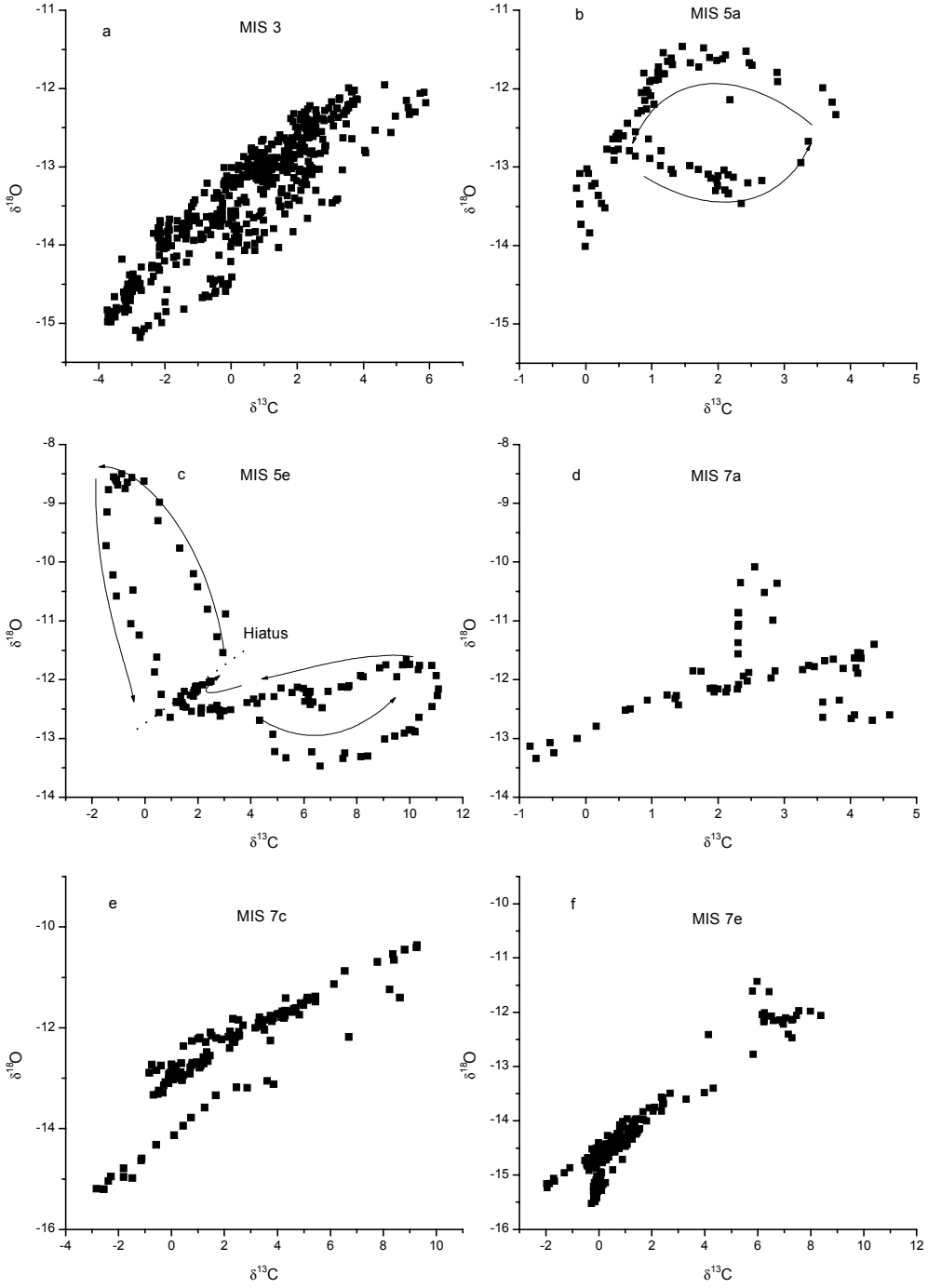

Fig. 4.12: Correlation between $\delta^{13}C$ and $\delta^{18}O$ for each growth phase. The arrows in plots **b** and **c** mark the progression of the isotope ratios during the respective growth phase. Note the partially different axes' scales.

The $\delta^{13}C$ / $\delta^{18}O$ diagrams (fig. 4.12) illustrate two pairs of isotopic characteristics: in 4 out of 6 growth periods, the correlation between $\delta^{13}C$ and $\delta^{18}O$ is high. The respective coefficients are 0.90 (MIS 3), 0.42 (MIS 7a), 0.88 (MIS 7c), and 0.94 (MIS 7e), and the gradients are nearly constant within one layer. In contrast, during MIS 5e ($R^2 = -0.55$) and MIS 5a ($R^2 = 0.27$) the ratio between $\delta^{13}C$ and $\delta^{18}O$ is more complex. Instead, we find a specific pattern for

each growth phase. Within MIS 5e two distinct loops subdivided by the previously mentioned macroscopic hiatus represent the first growth phase of MIS 5e and the presumed "classical Eemian", respectively (fig 4.12c). During the first part of MIS 5e (lower right part of fig. 4.12c), we observe no correlation between $\delta^{18}O$ and $\delta^{13}C$ isotopes ($R^2 = 0.04$). Presumably, the water flow in the cave was initially slow and scarce, leading to slow CO_2–degassing rates close to equilibrium, rose whilst the warming increased, and finally slowed down towards the end of the first warming of MIS 5e. This loop can be observed in the isotope plot and is indicated by the arrows in fig. 4.12c. During the second part, we observe a negative correlation between $\delta^{18}O$ and $\delta^{13}C$ ($R^2 = -0.62$), implying that another process was taking place (upper left part of fig. 4.12c). After the growth cessation, calcite with comparably low $\delta^{13}C$ and $\delta^{18}O$ ratios precipitated, and the subsequent rise of $\delta^{18}O$ values can probably be attributed to the reduced influence of isotopically depleted glacial melt water supply in comparison to precipitation, which directly penetrated the soil above the cave. Simultaneously, increasing vegetation density above the cave probably lead to a pedogenic CO_2 enrichment in the soil atmosphere resulting in a modest reduction of $\delta^{13}C$ values due to depleted values of CO_2 of organic matter. Despite a likely kinetical fractionation during the calcite precipitation, we observe only a slight corresponding enrichment in both isotope ratios during MIS 5e, probably owing to the fact that the resultant simultaneous enrichment was obscured by the massive alteration in water sources. The same situation, but to a lesser extent, may have existed during MIS 5a, where the correlation between $\delta^{18}O$ and $\delta^{13}C$ is partially reduced. As MIS 5e is the only period where a change of water sources can be observed, we regard the Last Interglacial as the warmest and longest phase within the past 250 kyr, when the glacier retreated further back and when plants could develop above the cave.

Spectral analysis

The MIS 3 interval of flowstone *SPA 59* is characterized by a comparably high and near–linear accretion rate of 6 mm/kyr. This value was derived from an error–weighted linear fit through 8 dated points, yielding a correlation coefficient of 0.989 (fig. 4.13). The uppermost point of MIS 3 was excluded from this calculation, because it yielded an age which lay outside of the stratigraphic order.

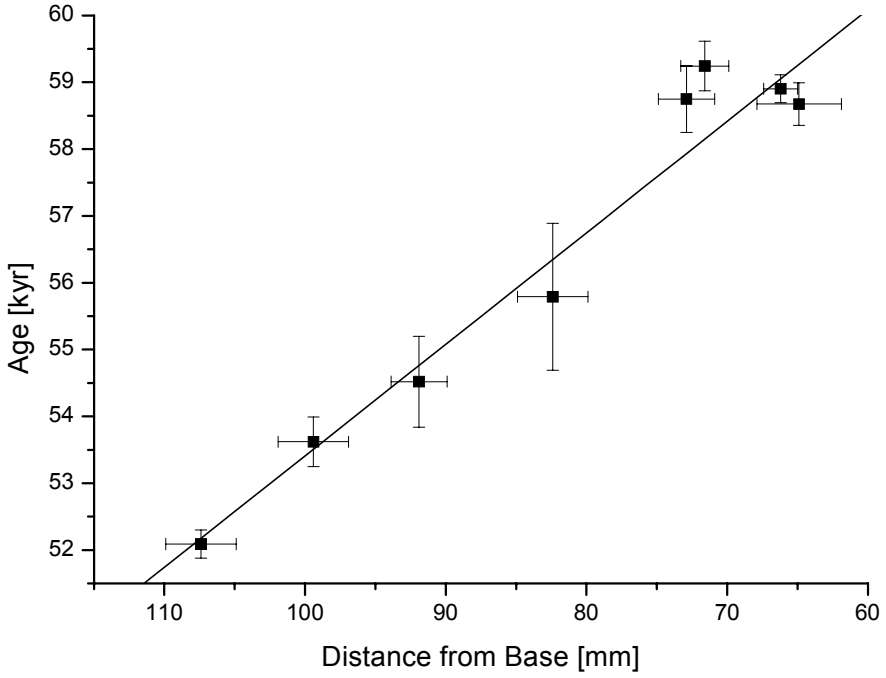

Fig. 4.13: Linear, error–weighted fit through the 8 dated points of the MIS 3 section of *SPA 59*, shown with 2σ error bars. The correlation coefficient is 0.989, the determined growth rate is 6 mm/kyr.

From the growth rate and the distance between two points where stable isotope samples have been taken, a mean time resolution of 16.7 years during the investigated interval of MIS 3 could be calculated. Based on these data, a spectral analysis was performed using the computer program *SPECTRUM* (*Schulz and Stattegger*, 1997) and *REDFIT* (*Schulz and Mudelsee*, 2002). It illustrated one major peak with a 1460 yr frequency for both the $\delta^{18}O$ and the $\delta^{13}C$ profiles (fig. 4.14). Three additional concordant peaks exceed the 95 % confidence level at 844 yr, 673 yr, and 508 yr, the latter of which had the highest amplitude. The low amplitude peaks at 2.93 kyr ($\delta^{13}C$) and 4.15 kyr ($\delta^{18}O$) are an artefact of the spectral analysis, because the investigated time interval is too short to derive frequencies longer than ~2 kyr. The detected cycles at 1460 yr and 508 yr periodicity are similar to two prominent cycles cited frequently in paleoclimatic investigations. Two minor peaks exceeding the 95 % significance level with a periodicity of 844 yr and 673 yr could not be linked to any published cycles.

For example, the 1470 yr cycle has been found in North Atlantic sediments and Greenland ice cores (*Bond et al.*, 2001, *Bond et al.*, 1997). It has been shown that the North Atlantic's ocean surface and the atmosphere above Greenland were a coupled system undergoing recurring shifts on millennial time scales. Additionally, variations of the methane content of ice in both Greenland and Antarctica parallel the Greenland warmings (*Blunier and Brook*, 2001), thus providing strong evidence that the Earth as a whole experienced this unstable climatic rhythm with a periodicity of about 1470 yr during glacial times. This finding is supported by $\delta^{18}O$ and $\delta^{13}C$ profiles taken from a stalagmite of a cave in the *Sauerland* (Western Germany) (*Niggemann et al.*, 2003). Spectral analysis yields a statistically significant peak at 1450 yr

and the stable isotopes show a good correlation with $\Delta^{14}C$ from European tree–rings. It has previously been demonstrated that warm peaks (*DANSGAARD/OESCHGER–Events*) occurred periodically every 1470 years in $\delta^{18}O$ in the GISP2 ice core over the past 100 kyr, but were not visible in the Holocene(*Grootes and Stuiver*, 1997). However, such periodicity could be found in the GISP2 ice chemistry, where it continued during the Holocene with reduced amplitude, but statistically indistinguishable frequency (*Bond et al.*, 2001).

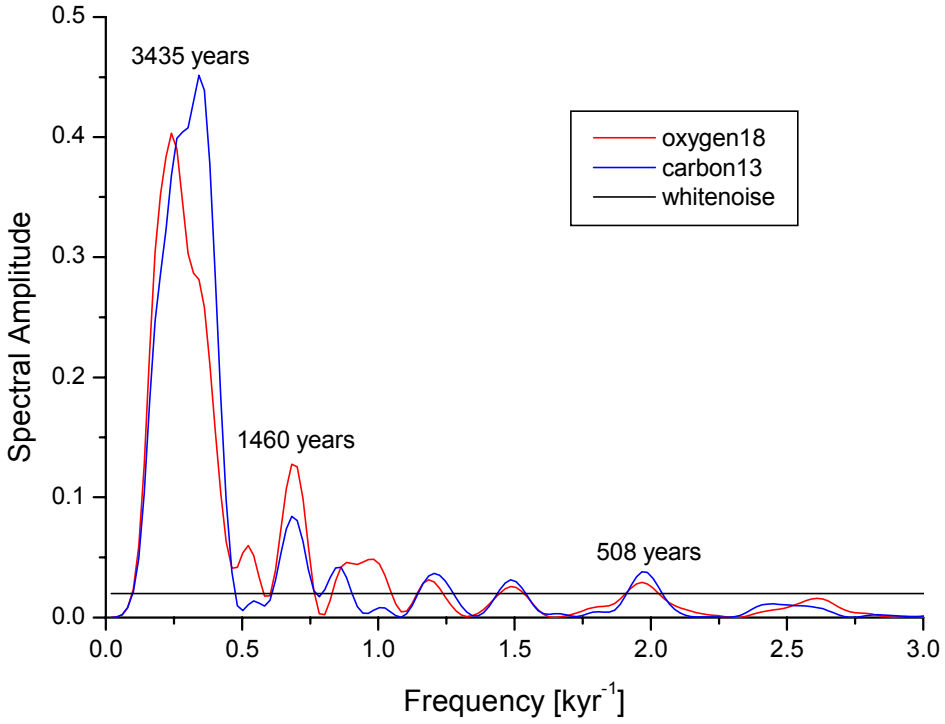

Fig. 4.14: Spectral analysis of the MIS 3 section of flowstone *SPA 59*.

The *SPA 59* results reveal that this cycle was also present over the past 58 kyr in a high Alpine setting, and was not restricted to the North Atlantic, where the respective sediments show such periodic imprint. However, no evidence of a solar cycle in the range of 1400 to 1500 yr has yet been found (*Stuiver and Braziunas*, 1993). The regularity of the occurrence of *D/O–Events* every 1470 yr or multiples thereof points to an extraterrestrial origin of the trigger of these globally detected climate changes (*Rahmstorf*, 2003). As proposed by *Niggemann et al.* (2003), a strong teleconnection between the North Atlantic ocean atmosphere pattern and Central Europe climate exists. This finding is supported by a previously studied $\delta^{18}O$ record of a stalagmite from *Spannagel Cave*, where remarkable correlations with $\delta^{18}O$ values of Greenland ice cores have been found (*Spötl and Mangini*, 2002). It has been shown that large–amplitude 1470 yr oscillations occurred, when continental ice mass exceeded a threshold level equivalent to approximately –45 m sea level in comparison to today and that the oscillations were tied to times of rapid change in ice mass (*Schulz et al.*, 1999). If this threshold is real, the strong 1460 yr signal of the *SPA 59* record suggests that sea level was below this value from ~59 kyr to 51 kyr, which corresponds to the sea level reconstruction from U/Th dated corals from *Huon Peninsula* (Lambeck *et al.*, 2002). No firm consensus yet exists on whether the 512 yr cycle is of solar origin or the result of internal marine circulation patterns. A strong 512 yr peak has been found in $\Delta^{14}C$ of the early

Holocene derived from tree–ring measurements (*Stuiver and Braziunas*, 1993), which was related to instabilities in North Atlantic thermohaline circulation, in turn potentially affected by a solar modulation of climate. From the presence of this cycle in the *Spannagel* archive one could conclude that the same trigger affected North Atlantic circulation pattern and Central Europe climate. Whether this trigger is of solar origin or the result of internal climate processes remains unclear.

Cycles on the decadal to centennial timescale have been found in the adjacent stalagmite *SPA 50* which have been related to solar cycles (*Holzkämper et al.*, submitted). Explaining the presence of both decadal to centennial scale cycles and millennial cycles within the same archive with a common trigger is tantalizing, but can not be proofed by findings of this study.

The *SPA 59* results reveal that the driving force for major climate changes during the past 250 kyr can not solely be reduced to the Earth's orbital parameters, and additional triggers have to be considered. This finding has been derived from the growth phases of speleothems, which are an indicator of warm climate. The timing of the onset and termination of growth phases can only partly be explained by *MILANKOVITCH* forcing, but it also contradicts this forcing at certain time intervals. Alternatively, geomagnetic field maxima can explain the observed deviations, and a link between the flux of galactic cosmic rays and the Earth's climate appears to be corroborated (*Christl et al.*, in press). The detected cycles of 1460 yr and 508 yr periodicity in the stable isotope profile from flowstone *SPA 59* indicates that Central European climate and North Atlantic circulation are a coupled system, and that the pacing of ~1470 yr of *D/O events* extends back at least 59 kyr. Furthermore we emphasize the marked difference of MIS 5e in comparison to the other interglacials over the past 250 kyr with high temperatures and/or high precipitation amounts, which have also been visible by several other climatic archives (*Kandiano et al.*, in press, *Winograd et al.*, 1997).

4.2 Reconstruction from sinter influenced by the Indian Ocean / African Monsoon

4.2.1 Oman

Southern Arabia is affected by one of the most important components of tropical climate, the Indian Ocean Monsoon. Today, the northern limit of the summer monsoon, the *Intertropical Convergence Zone* (*ITCZ*), is located south of the Arabian landmass (fig. 4.15). As a consequence, the main part of the Arabian peninsula is characterized by arid or semiarid conditions. The only source of humidity are cyclonic low–pressure systems approaching from the Mediterranean Sea during the winter months (*Weyhenmeyer et al.*, 2000). Previous studies in Oman have shown that during Interglacials, the *ITCZ* was shifted towards the north, so that monsoonal precipitation could reach the southern and eastern parts of the Arabian Peninsula (*Burns et al.*, 2001). This was documented by growth phases of stalagmites from southern and northern Oman. Low $\delta^{18}O$ values of deposited calcite ranging from –4 ‰ to –8 ‰ VPDB are characteristic for a monsoonal origin of precipitation, whereas modern speleothems range from –1 ‰ to –3 ‰ (*Burns et al.*, 2001). In this study, the attention was turned to the Last Interglacial growth phases of stalagmites. *Hoti Cave*, located at 23°06'N / 57°21'E and 800 m a.s.l., is a 4.5 km–long through cave in the foothills along the Oman Mountains. Cave temperatures range from 23 °C and 26 °C, relative humidity is close to 100 %. The cave is decorated with a number of active, but small stalagmites (< 10 cm) and larger fossil stalagmites (30 cm to 3 m).

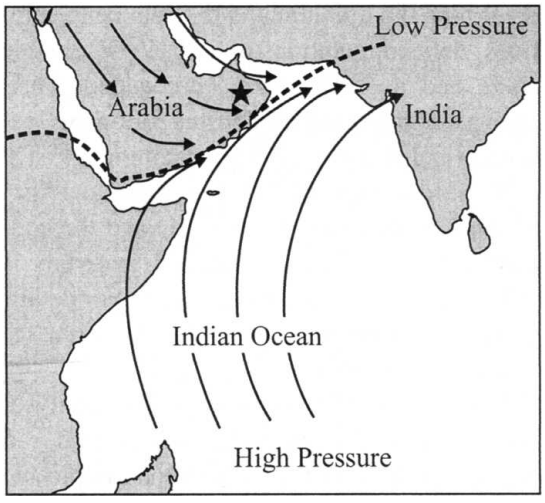

Fig. 4.15: Map showing location of *Hoti Cave* (star) and generalized modern, summer, surface wind pattern. The dashed line represents the approximate location of the ITCZ. (From *Burns et al.*, 2001)

One fossil stalagmite, labelled *H13*, is 3 m high and was found lying detached from its substrate. It has previously been dated by U–series method (*Neff*, 2001), and it was determined that the stalagmite has formed during periods equivalent to MIS 5e, MIS 7a, and MIS 9. No growth took place during intervening times. As the Last Interglacial section of stalagmite *H13* was only dated at 3 points with a comparatively large error, additional 33 datings were performed in order to achieve a better accuracy in determining the beginning, the progression, and the termination of the Last Interglacial growth period. The results of the

TIMS dates are summarized in table A.3 and plotted in fig. 4.16. The beginning of the Last Interglacial section was dated at 129.9 ± 2.8 kyr. A number of datings yielded older ages, but they are interpreted as mixing ages due to the unclear and dense layering at the transition from the previously dated growth phase corresponding to MIS 7a and the Last Interglacial growth phase. For this reason, some of the yielded ages are in stratigraphically reversed order. The youngest age at the top of the stalagmite was dated at 116.6 ± 2.6 kyr. However, additional datings on samples taken a few centimeter away from the top yielded ages that are markedly older than samples from the main part of the MIS 5e section. We attribute this to possible uranium leaching of the topmost part of the stalagmite during the past ~120 kyr, when the stalagmite was inactive and erosional processes could have affected the calcite over a long period of time. This may also be the reason for several dates which lie significantly off the determined depth–age relationship, e.g. between 100 cm and 120 cm from the top of the stalagmite. Probably, these deviations reflect a period of growth cessation interrupting the Last Interglacial growth period, as a result of reduced monsoonal influence at around 125 kyr.

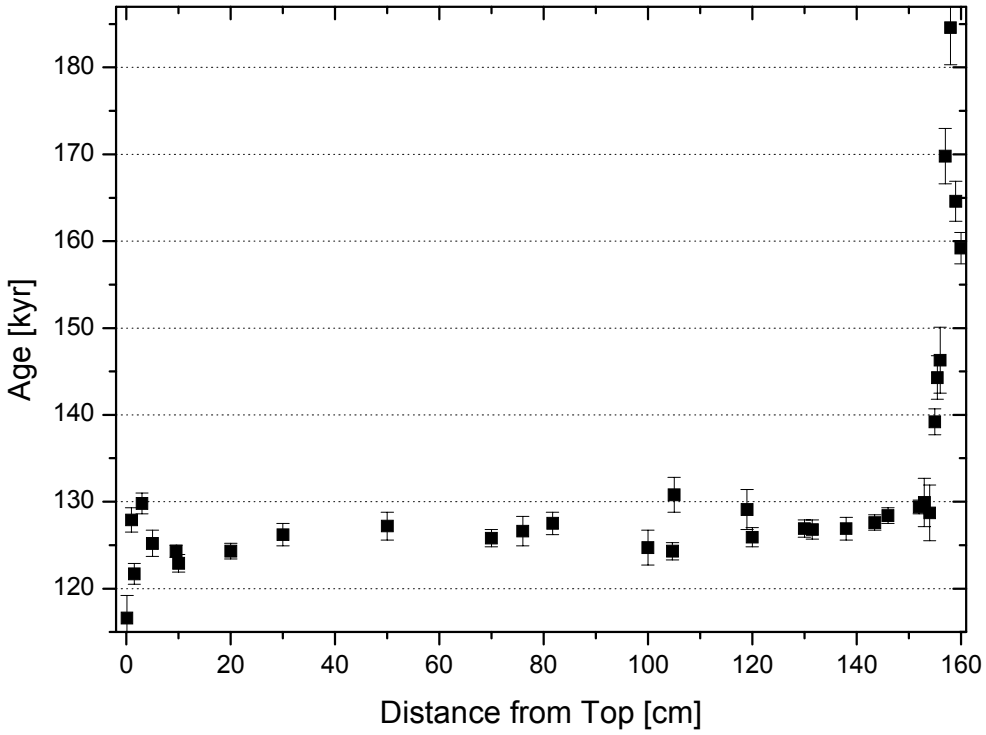

Fig. 4.16: U–series ages of stalagmite *H13* with associated 2σ error bars versus sample depth (see also table A.3).

Apart from the TIMS dating, $\delta^{18}O$ and $\delta^{13}C$ values were measured along the growth axis of the Last Interglacial section of the stalagmite (fig. 4.17). In low–latitude settings temperature and $\delta^{18}O$ of rainfall are not correlated and oxygen isotope changes rather reflect variations in rainfall amounts, particularly in areas receiving heavy, tropical rainfall (*Rozanski et al.*, 1993). Isotopic data on modern monsoonal rainfall show that the precipitation during monsoonal months is characterized by much lower $\delta^{18}O$ values than those measured on precipitation during the rest of the year (for example in New Delhi: monsoonal months: mean $\delta^{18}O$ = –6.4 ‰ VSMOW; other months: mean $\delta^{18}O$ = –0.46 ‰ (*Burns et al.*, 1998)). Therefore it was

concluded, that the low $\delta^{18}O$ calcite values of –5 ‰ to –10 ‰ VPDB in *H13* are the result of enhanced monsoonal precipitation during the time of speleothem formation. The isotope dates were put on an absolute timescale by applying an age model, which consists of a linear, error–weighted fit through 22 dated points of the Last Interglacial section. For calculating the fit function, the uppermost four dates were omitted due to possible uranium leaching of these samples. A mean growth rate of 36.3 cm/kyr was calculated for the main part of the Last Interglacial section, with a correlation coefficient of the fit function of 0.79. Initial and final growth rates may have been lower, but could not be determined from the few data. Stable isotope samples were taken in 5 mm steps from the top to 127 cm from the top. According to the TIMS dates, the Last Interglacial section covers the uppermost ~155 cm of the stalagmite. As the remaining 28 cm could not be analyzed for stable isotopes by the time this study was printed, they were simulated by fitting a second order polynomial to the existing data and by extrapolating the calculated trend over the entire 155 cm section (dashed curve in fig. 4.17). The resulting curve exhibits a slight trend towards lower $\delta^{18}O$ values in the middle part of the growth phase, and comparatively higher values at the beginning and termination of the Last Interglacial. This trend possibly represents the initially and finally weaker influence of the summer monsoon in comparison to the middle part of the Last Interglacial, from about 128 kyr to 125 kyr.

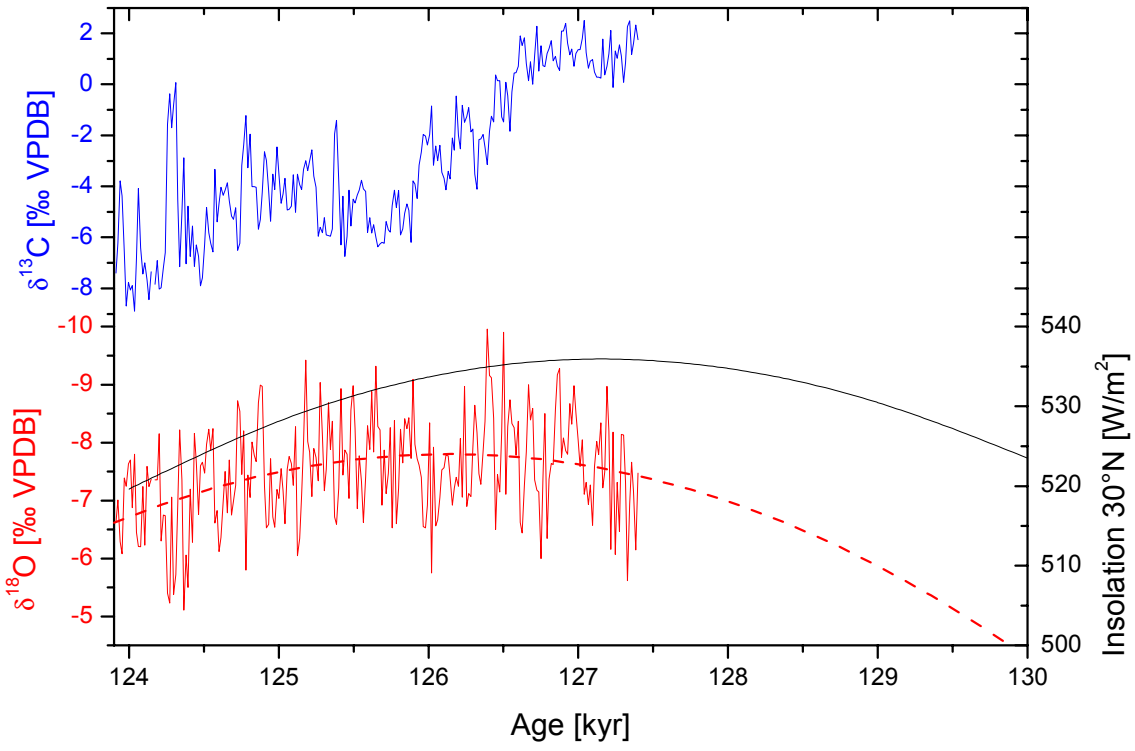

Fig. 4.17: $\delta^{13}C$ and $\delta^{18}O$ profile based on age model. Solid black line: June insolation at 30°N. Dashed red line: second order polynomial fit through the isotope profile, extended back to 130 kyr, when stalagmite growth commenced.

When comparing the general trend of the oxygen isotope progression during the Last Interglacial with the June insolation curve at 30°N, an approximate similarity can be detected, suggesting that solar summer insolation was the main trigger for the strength of the Indian

Ocean monsoon, at least during the Last Interglacial. However, this finding does not necessarily answer the question, if solar summer insolation plays the predominant role for monsoonal strength rather than glacial boundary conditions (see chapter 4.2.4).

The $\delta^{13}C$ profile shows a characteristic feature for soil development during the humid period of the Last Interglacial. Commencing with high values of about +2 ‰ VPDB, reflecting the host rock values, they rapidly decrease to values from –2 ‰ to –8 ‰ about 3 kyr after the beginning of the pluvial period, indicating that persistently moist conditions enabled vegetation to develop, leading to enhanced root respiration in the upper soil and decreased $\delta^{13}C$ values in the interstitial water.

A further conclusion may be drawn from the carbon and oxygen isotope profile. As shown in fig. 4.18, there is no correlation between both isotope ratios, indicating, that calcite precipitation took place under equilibrium conditions and no kinetical fractionation was involved. This finding is in concordance with the high relative humidity measured in the cave, preventing effectively from evaporation of the drip water the stalagmite was fed by.

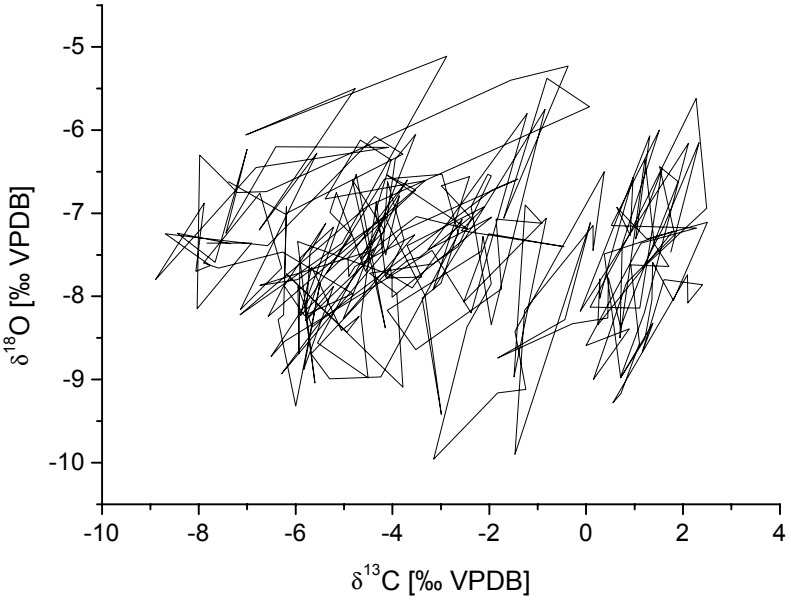

Fig. 4.18: $\delta^{13}C$ versus $\delta^{18}O$ of the Last Interglacial interval of stalagmite *H13*, indicating that there have no kinetical effects taken place during calcite precipitation.

An additional stalagmite from *Kahf Tahry*, located near the coast of northern Oman, ~150 km east of *Hoti Cave*, corroborates the finding that the growth rates of speleothems were greatest during periods of maximum northern summer insolation. The somewhat earlier start of the growth phase corresponding to MIS 5e relies on the shorter distance from the coast, where the South Asian Monsoon influence was larger than further to the west. Lower $\delta^{18}O$ values from –11 ‰ to –9 ‰ of the precipitated calcite than in *H13* may reflect enhanced monsoonal influence near the coast, too (fig. 4.19).

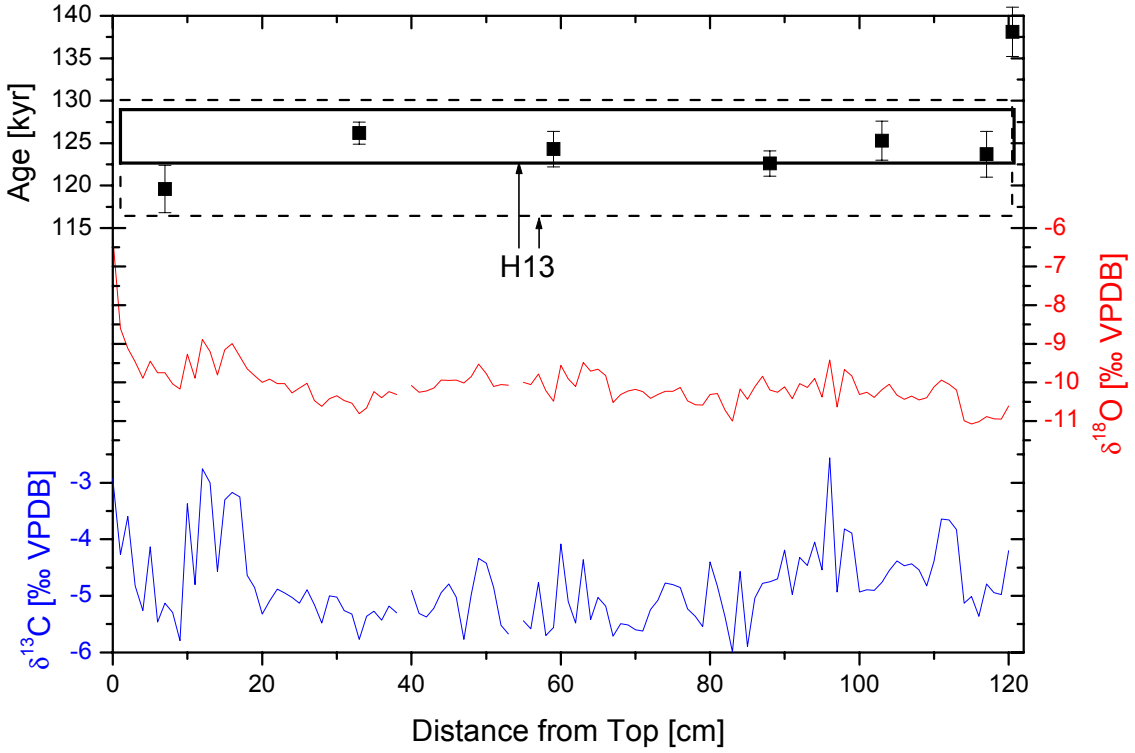

Fig. 4.19: U–series ages with associated 2σ error bars versus sample depth $\delta^{18}O$ profile (red curve) and $\delta^{13}C$ profile (blue curve) of stalagmite *T1* from *Kahf Tahry* (northern Oman). The dashed black box indicates the growth period of stalagmite *H13* , the solid box the main growth period with high accretion rate.

The $\delta^{13}C$ values vary rapidly along the growth axis between –6 ‰ and –2.5 ‰ VPDB. Thus, they are less negative than in *H13*, which could be the result of merely scarce vegetation above the cave. Furthermore, a slight correlation between the $\delta^{13}C$ and $\delta^{18}O$ values of R^2 = 0.38 can be observed, indicating that calcite precipitation took place under non–equilibrium conditions. Evaporation effects may be the most likely explanation for that, leading to a concomitant enrichment of heavy carbon and oxygen isotopes.

4.2.2 Egypt

Djara Cave is one of the few caves in the Western Desert of Egypt containing speleothems. It is located close to the *Farafra*–oasis in western Egypt and was first visited by the German GERHARD ROHLFS on 24th December 1873, who found an extensive speleothem development in this cave (*Brook et al.*, 2002). The cave is located on an Eocene plateau between the *Farafra* depression and the *Nile* valley, at about 27.5°N and 30°E, which consists of highly fractured carbonates of the *Minia* and *Naqb* formations.

Fig. 4.20: Map of Egypt with the location of the *Djara Cave* (blue star) near *Farafra*–oasis. (from www.lib.utexas.edu)

Presently, the area's climate is hyper–arid, with only 4 mm of recorded rain from 1948 to 1982, and a mean annual temperature of 21.8 °C in *Farafra* (*Brook et al.*, 2002). The cave temperature is 23 °C year–round and appears to stay very close to the external mean temperature. A variety of partially sand covered speleothems, like stalactites, stalagmites, and flowstones decorate the single cave chamber with a diameter of about 25 m and a maximum height of 6 m. An archaeological feature are etchings close to the entrance of the cave, showing ostrichs, antelopes, bovids, and goats, all of which are not present today due to the dry conditions. A plan of the cave with the location of the most prominent features and speleothems is shown in fig. 4.21.

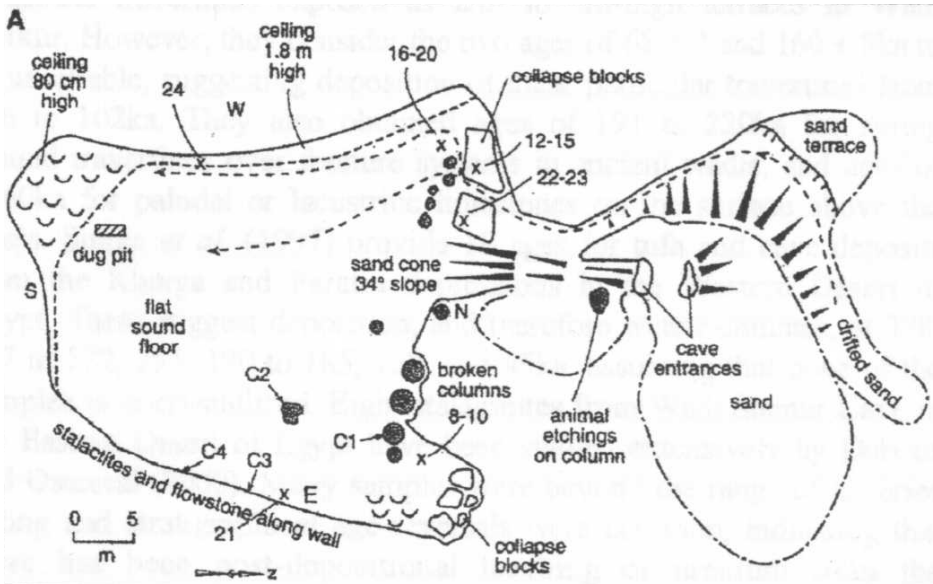

Fig. 4.21: Plan of *Djara Cave* showing the most prominent features and sampling sites of former expeditions (from *Brook et al.*, 2002).

A number of covered hearths in the close vicinity of the cave have been found by previous expeditions, some of which were dated with the radiocarbon method. These and additional datings of ostrich egg shells yielded ages between 9.7 kyr to 5.5 kyr, indicating that wetter conditions prevailed in the area during this time interval.
Previously conducted U/Th datings of speleothems by α–spectrometry yielded ages ranging from 140 ± 15.9 kyr to 283 ± 56 kyr (*Brook et al.*, 2002). One TIMS date yielded 201.05 ± 2.1 kyr. A number of samples was beyond the U/Th dating limit (~ 500 kyr for TIMS dating, ~ 350 kyr for α–spectrometry). These results indicate that the main growth phases of speleothems occurred during MIS 5, 7 and 9, and additionally, during earlier periods exceeding the U/Th dating limit. Isotopically depleted values, which were also measured within earlier investigations, suggest that enhanced African summer monsoon and westerly circulation during the winter months advected precipitation to the Western Desert enabling speleothems to form in the recently hyper–arid region.
Five different stalagmites from *Djara Cave* have been sampled in an expedition in January 2003 and were dated in this study. The results of the mass spectrometric U–series dates are summarized in table 4.1.

Table 4.1: Results of the mass-spectrometric analyses of stalagmites from *Djara Cave*. ^{232}Th concentration was < 0.1 ng/g for all samples. *F03-K* is a sample from the *Crystal Mountains*, ~ 100 km northwest of *Djara Cave*.

Sample	Dst. fr. top	δU		^{238}U		^{230}Th		Age	
	cm	‰	error	µg/g	error	pg/g	error	kyr	error
F03-1-1-1,0	1	17.29	2.91	0.2157	0.0003	3.515	0.022	394	+ 32/ - 25
F03-1-1-3,0	3	3.27	2.65	0.2267	0.0002	3.679	0.020	475	+ 74/ - 44
F03-2-0-1,5	1.5	6.43	5.71	0.2656	0.0002	4.375	0.023	>500	x
F03-2-2-9,0	9.0	14.31	5.13	0.1899	0.0004	3.148	0.037	>500	x
F03-3-1-1,5	1.5	-4.13	6.47	0.2083	0.0002	3.408	0.060	>500	x
F03-3-1-5,0	5	3.92	2.29	0.3648	0.0004	6.049	0.057	>500	x
F03-4tl-1-1,0	1	53.37	20.78	0.6057	0.0032	12.588	0.516	>500	x
F03-4tl-1-4,0	4	19.91	2.56	0.7326	0.0009	12.118	0.052	449	+ 43/ - 30
F03-4tl-1-7,5	7.5	9.99	6.22	0.8052	0.0027	13.665	0.112	>500	x
F03-K-i	x	-63.25	33.51	0.0497	0.0001	1.484	0.115	>500	x
FAR1-1	1	7.63	3.38	0.2718	0.0003	4.413	0.052	437	+ 120/ - 55
FAR1-35	35	9.20	3.52	0.2375	0.0002	3.830	0.062	395	+ 99/ - 51
FAR1-68	68	-3.47	3.22	0.2573	0.0002	4.153	0.022	515	+ 150/ - 61

Two out of five sampled stalagmites from *Djara Cave* yielded ages exceeding the U/Th-dating range of ~ 500 kyr, as it was the case for an additional small stalagmite from the nearby *Crystal Mountains* (labelled *F03-K*). One large stalagmite (*F03-4tl*) was close to the dating limit, so that no age could be calculated for two out of three datings. The stalagmites *F03-1* and *FAR1* (the latter one was sampled in a previous expedition by H.J. PACHUR, Berlin) most likely originate from MIS 11, which is supported by an ESR–dating of *FAR1*, yielding

an accumulated dose of 59.9 ± 1.9 Gy and a resulting age of 400 ± 50 kyr (*Hoffmann, D.* and *Holzkämper, S.*, unpublished data).

4.2.3 United Arab Emirates

The aim of our investigation was to determine the age of the travertines forming at a well near the excavation site at *Jebel al-Buhais* (United Arab Emirates).

Fig. 4.22: Map of the United Arab Emirates with sampling location (blue star). (from www.worldatlas.com)

The investigation may serve to indicate any coherency between the availability of water and the neolithic settlements and graves found at the sampling site. Six different samples from the area have been analyzed by mass spectrometric U–series dating technique. The samples were cleaned from dust and sand remains with a micro drill before sample preparation was performed using ion exchange columns as described in chapter 2.1.4.
Additionally, the same set of samples was analyzed for stable isotope ratios ($\delta^{18}O$ and $\delta^{13}C$) in order to gain insights into the precipitation's origins, which had fed the well.

Sample description

„E-72010": amorphous, porous filling-material of the well-basin, top of the hill, ~5 cm below the recent surface.
„E-72212": amorphous, porous filling-material of the well-basin, top of the hill, ~25 cm below the recent surface.
„E-72211": well sinter-layer, uppermost hill-position, massive rock.
„E-72205": well sinter-layer, lowermost hill-position, massive rock.
„E-72198": multi-layered sinter, sitting on a big rock, ~5 m next to the well.
„E-72177": wall-sinter from a vertical crevice, ~10 m above the well.

The mass spectrometric U/Th dating of travertines at the *Jebel al–Buhais* site yielded ages between 65.5 kyr and 368 kyr (table 4.2). Holocene travertines were not found. From a technical point of view, the yielded ages are reliable, as almost no detrital contamination had to be corrected for, and the age errors are acceptably low.
Uncertainty arises from possible contamination of the measured samples with old carbonate from the surroundings, which could have contributed non–authigenic U and Th to the sinter via windblown dust. Additionally, post–sedimentary processes of U–leaching of the partially porous sinter may have altered the initial isotope composition, resulting in unrealistic ages derived from the present U/Th ratios.

Table 4.2: Mass–spectrometric U–series ages, $^{234}U/^{238}U$ activity ratios, and isotope concentrations of sampled calcareous sinter. All values are given with 2σ errors.

Sample	δU		^{238}U		^{232}Th		^{230}Th		Age	
	(‰)	error	(µg/g)	error	(ng/g)	error	(pg/g)	error	(kyr)	error
E-72010	43.161	5.741	0.577	0.001	18.562	0.098	9.644	0.128	368	44
E-72177	70.588	3.692	0.488	0.001	13.720	0.077	7.646	0.094	230.7	10.0
E-72198	27.113	4.216	1.262	0.003	9.758	0.024	16.376	0.084	159.5	2.6
E-72205	39.670	2.336	1.229	0.001	34.721	0.076	16.290	0.044	161.2	1.4
E-72211	46.904	2.298	0.991	0.001	17.118	0.034	14.535	0.064	204.5	3.1
E-72212	24.801	9.905	0.965	0.004	53.402	0.326	7.441	0.067	65.5	1.3

However, if the ages are real, we conclude that the growth periods of travertines in the determined site all fall into periods of low solar summer insolation over the Northern Hemisphere (fig. 4.23), but with different glacial boundary conditions.

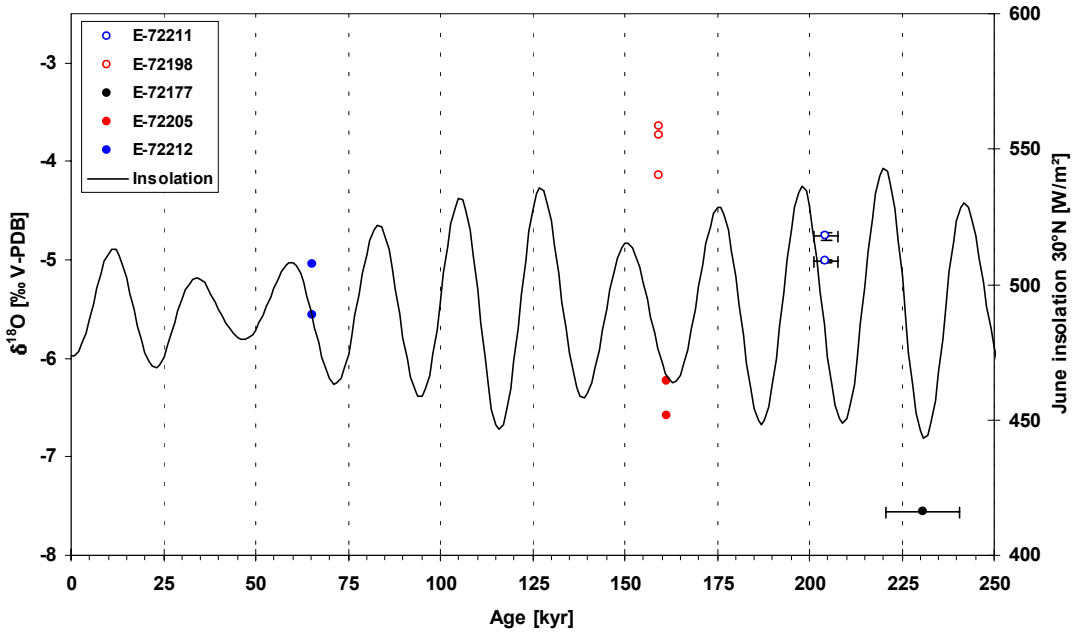

Fig. 4.23: Ages and $\delta^{18}O$ values of analyzed sinter and June insolation curve (30°N). *E-72010* is not plotted due to its large dating uncertainty.

Samples *E-72211* and *E-72177* formed during the MIS 7 interglacial, whereas samples *E-72212*, *E-72198*, and *E-72205* formed during glacial periods. The large age uncertainties of samples *E-72177* and *E-72010* do not allow any conclusions about the phasing with the insolation curve to be drawn. Oxygen isotope analyses were carried out at least once on each sample that had previously been dated. The results show a wide range of $\delta^{18}O$ values ranging from –2.47 ‰ to –7.05 ‰ VPDB, whereas the $\delta^{13}C$ values are fairly constant with a mean of –0.35 ‰ VPDB (table 4.3).

Table 4.3: $\delta^{13}C$ and $\delta^{18}O$ values given as ‰ VPDB of sampled calcareous sinter with standard deviations (SD). Suffixes a-c indicate multiple analyses on the same sample.

Sample	$\delta^{13}C$		$\delta^{18}O$	
	(‰)	SD	(‰)	SD
E-72010-a	-1.15	0.01	-2.47	0.04
E-72010-b	-0.46	0.01	-4.19	0.03
E-72177-a	-1.44	0.02	-7.05	0.02
E-72198-a	0.77	0.01	-3.17	0.03
E-72198-b	0.37	0.01	-3.65	0.04
E-72198-c	0.53	0.02	-3.23	0.02
E-72205-a	-1.12	0.02	-5.69	0.02
E-72205-b	-1.76	0.01	-6.09	0.05
E-72211-a	0.12	0.02	-4.28	0.03
E-72211-b	-0.22	0.02	-4.52	0.02
E-72212-a	0.32	0.02	-4.54	0.04
E-72212-b	-0.22	0.02	-5.07	0.03

Generally, the low values of $\delta^{18}O$ point to the south–west summer monsoon as being the major contributor to the local precipitation. During glacial times the *ITCZ* was located farther south than it is today, so that the north–eastern part of the Arabian peninsula was not affected by the southwest monsoon (*Weyhenmeyer et al.*, 2000). Concomitantly, the northern, Mediterranean water vapor source was reduced, as shown by many continental records from Arabia, Africa and southern Europe. Thus, it is unlikely that samples *E-72212*, *E-72198*, and *E-72205* reflect a monsoonal or Mediterranean influence at our study site. Rather, they may reflect tropical cyclonic storm cells from the Arabian sea, which formed during hot summers and advected precipitation to the Arabian peninsula during times of a reduced south–west monsoon. During periods with high solar insolation, a large land–sea thermal gradient between the Indian Ocean and the Asian landmass resulted in a strengthened summer monsoon (*Overpeck et al.*, 1996), causing a strong offshore monsoonal air stream which paralleled the south–eastern Arabian coast (*Weyhenmeyer et al.*, 2000). These strong winds prevented tropical cyclonic storm cells forming over the Arabian Sea from reaching the Arabian coast. Additionally, the interglacial–glacial temperature decrease of about 6 °C recorded in northern Oman (*Weyhenmeyer et al.*, 2000) probably led to a reduction of evaporation during cooler periods.

These two factors may have led to an increased precipitation/evaporation ratio during colder periods resulting in the well at the study site to be activated during these time intervals.

During periods which were warmer than today, as for example during the early Holocene, MIS 5e, and probably parts of MIS 7e, when the ITCZ moved far to the north, the summer monsoon may have reached the study site, advecting isotopically light precipitation (*Burns et al.*, 2001). Sample *E-72177* probably represents the warm MIS 7e, and the light $\delta^{18}O$ value of ~ –7 ‰ indicates monsoonal precipitation. But due to the large age uncertainty, the sample may also originate from a cold phase interrupting MIS 7.
The wide range of $\delta^{18}O$ values from –7 ‰ to –2.5 ‰, even from concomitantly growing sinter, suggests the presence of local effects which influenced the isotope ratios of the precipitated carbonate. Depending on the evaporation rate and percolation processes, the water was isotopically fractionated, resulting in a simultaneous enrichment of $\delta^{18}O$ and $\delta^{13}C$ values. $\delta^{18}O$ values as high as –2.5 ‰ therefore do not contradict a tropical cyclonal origin.
The U/Th age determinations as well as the stable isotope analyses of six calcareous sinter from the excavation site *Jebel al–Buhais* reveals humid episodes during glacial periods, when tropical cyclones from the Arabian sea advanced to the north–eastern Arabian peninsula. However, the existence of an active well during times of enhanced southwest summer monsoon, as during the early Holocene from ~10 kyr to 6 kyr, seems to be possible, when the *ITCZ* reached farther to the north than today. Two samples which formed during MIS 7 have been found, supporting the hypothesis of humid conditions over large parts of Arabia during peak interglacial periods.

4.2.4 Paleoclimatic implications

The results of the investigation of archives recording the Asian and African summer monsoon support some previously stated characteristics of low latitude climate: MIS 11 was probably the warmest and longest interglacial of the last 500 kyr. It was warm enough to shift the *ITCZ* so far to the north that the summer monsoon could reach areas that were semi– to hyper–arid during the most parts of the last 500 kyr. However, it is still being discussed, whether the monsoon system is more responsive to changes in solar insolation or to glacial boundary conditions. The more recent investigations corroborate a link between high– and low–latitude climates derived from the comparison of monsoonal strength proxies and glacial condition proxies in a marine sediment core near the coast of Oman (*Clemens et al.*, 1996). The Eemian in Northern and Central Europe appears concomitantly to enhanced monsoon in Eastern Arabia. It has previously been concluded, that the peak interglacial periods during the past four glacial cycles were accompanied by a continental pluvial phase over Northern Africa and Arabia (*Burns et al.*, 2001); thus, continental wetness was probably controlled by some aspect of glacial boundary conditions, such as sea–surface temperatures in the Indian Ocean, snow cover on the Himalayan plateau, or CO_2–concentrations. The dataset of this study supports this idea, but additionally, insolation plays an important role for the strength of the summer monsoon as well. This can be concluded from stalagmite *H13* from Oman, where the growth parallels the peak insolation during the Last Interglacial, from 130 kyr to 124 kyr. The samples from the United Arab Emirates formed during periods with low summer insolation,

when monsoonal strength probably was weak, corroborating the strong influence of solar insolation to monsoonal activity. The stalagmites from Egypt can not be interpreted with respect of insolation phasing due to the large age error, but may support the assumption that the monsoon was strongest during peak interglacial conditions, which were present during the period equivalent to MIS 11.

5 Conclusions

The investigation of stalagmites and similar secondary carbonate deposits has yielded insights in the timing and progression of Last Interglacial climate and has added valuable data to determine possible forcing mechanisms influencing the climate of the past 400 kyr.
The high–resolution study of stalagmite *SPA 50* and flowstone *SPA 52* from the *Spannagel Cave* (Central Alps) revealed the existence of a warm phase prior to the classical Eemian from ~135 to 130 kyr, which can not be explained by *MILANKOVITCH* forcing. Instead, the Sun's and Earth's magnetic fields might have acted as an additional trigger, initiating the first warming of the Last Interglacial. After a climatic deterioration, the classical Eemian commenced about 126 kyr ago and lasted until ~116 kyr. According to the stable isotope profiles taken along the growth axes of the speleothems, the ambient temperature during the Eemian was at least as high as today at this high Alpine site. The growth reductions of stalagmite *SPA 50* at about 123.8 kyr and 120.1 kyr could be the product of cold spells, during which the annual mean temperature was at least 1 to 2 °C lower than today, but may alternatively be the result of changed hydrological conditions in the cave. A spectral analysis of the $\delta^{18}O$ profile of stalagmite *SPA 50* yielded cycles on the decadal to centennial time scale with periodicities of 197, 109, and 21 years, which are probably related to solar activity cycles, revealing solar forcing of the Eemian climate. A possible forcing mechanism could be the influence of the flux of Galactic Cosmic Rays on condensation processes in clouds, in turn affecting the energy budget and latent heat transport of the Earth's climate.

External forcing of the Earth's climate is also derived from the investigation of flowstone *SPA 59* from *Spannagel Cave*. The timing of growth phases of *SPA 59* reveals that the climate changes during the past 250 kyr can not solely be ascribed to alterations of the Earth's orbital parameters. Variations of the geomagnetic field intensity may explain the observed deviations from orbitally tuned climate archives, and a link between the flux of Galactic Cosmic Rays and the Earth's climate appears to be corroborated.
The spectral analysis of a growth period corresponding to MIS 3 yielded cycles of 1460 yr and 508 yr periodicity in the stable isotope profile from flowstone *SPA 59*. Explaining the presence of both decadal to centennial scale cycles and millennial cycles within the same archive with a common trigger is tantalizing, but can not be proofed by the findings of this study. The detected 1460–year cycle might correspond to the *DANSGAARD/OESCHGER cycles* detected in deep sea sediments of the North Atlantic and in Greenland ice cores, indicating that Central European climate and North Atlantic circulation are a coupled system, and that the pacing of ~1470 yr of *D/O–Events* extended back at least 59 kyr.

The results of the investigation of archives recording the South Asian and African summer monsoon support some previously stated features of low latitude climate:
MIS 11 was probably the warmest and longest interglacial of the past 500 kyr. It was warm enough to shift the *ITCZ* further to the north, so that the African summer monsoon could

influence the Central–Sahara, and speleothems could grow, where semi– to hyper–arid conditions had prevailed during the most parts of the past Quaternary. The dataset of this study supports the idea that the monsoon system is responsive to changes of glacial boundary conditions, as the speleothem growth periods were in concert with the Marine Isotope Stages. Additionally, insolation plays an important role for the strength of the summer monsoon as well. This can be concluded from stalagmite *H13* from Oman, where the main growth period of the Last Interglacial is accompanied by a high solar summer insolation interval, lasting from 130 kyr to 124 kyr, with the $\delta^{18}O$ values of precipitated calcite – an indicator of monsoonal strength – running parallel with the insolation curve. The sinter deposits from *Jebel al–Buhais* in the United Arab Emirates formed during periods with low summer insolation, when monsoonal strength probably was weak, corroborating the strong influence of solar insolation on monsoonal activity.

The task of utilizing the Eemian as a template to the Holocene remains challenging. Defining the beginning of the Holocene as the end of the *Younger Dryas* cold event, about 10 kyr ago, and viewing the duration of the classical Eemian from 126 kyr to 116 kyr, then a natural end of the Holocene should be close. However, by viewing at other interglacials, such as MIS 7, it is obvious that the timing and progression of each interglacial seems to be special, probably as a result of different orbital constellations and different glacial boundary conditions preceding the interglacials. More data have to be collected, especially from the interglacials MIS 7, MIS 9, and MIS 11, to obtain deeper knowledge about their duration and progression, before forecasts can be made about the duration of the Holocene.

An important component of future investigations should be the recovery and analysis of fluid inclusions entrapped in calcite deposits, as they can serve as archives directly linked to the past precipitation. Thus, the problem of deriving stable isotope values of the groundwater from the values of precipitated calcite could be circumvented. Additional parameters could include atmospheric noble gases dissolved in fluid inclusions, which provide information about the temperature, at which the calcite was deposited. Furthermore, intercomparisons between different climate archives will continue to be an important tool to create reliable and consistent reconstructions of past climate. Finally, the global map illustrating the locations of investigated climate archives still shows regions where only a few or no data exist, such as the continents of the Southern Hemisphere or the Arctic region.

Appendix

TIMS data

Table A.1: Stalagmite *SPA 50*:

D.f.Base [mm]	$\delta^{234}U$ [‰]	± [‰]	Conc. ^{238}U [µg/g]	± [µg/g]	Conc. ^{232}Th [ng/g]	± [ng/g]	Conc. ^{230}Th [pg/g]	± [pg/g]	Age [kyr]	± [kyr]
6.8	21.40	1.88	69.063	0.090	19.203	0.060	807.93	2.91	130.5	1.1
20.6	11.54	3.16	72.338	0.145	26.106	0.050	835.80	2.34	130.2	1.2
35.7	9.01	1.65	7.348	0.007	3.950	0.014	83.98	0.40	128.3	1.3
41.7	12.74	2.63	8.390	0.010	2.579	0.004	95.24	0.21	125.6	0.9
47.0	6.88	1.68	6.770	0.006	2.791	0.008	76.20	0.28	125.2	1.0
71.5	15.30	4.12	7.667	0.019	1.884	0.009	87.58	0.46	126.4	1.8
74.9	10.36	1.67	7.523	0.005	1.071	0.003	84.71	0.41	124.4	1.2
85.7	11.66	1.44	5.952	0.005	3.095	0.007	67.42	0.24	125.4	1.0
91.9	16.18	2.73	5.033	0.009	2.789	0.012	57.52	0.26	126.3	1.4
94.1	16.73	1.67	4.541	0.005	2.993	0.012	51.88	0.36	126.1	1.7
95.1	-0.47	1.75	3.600	0.003	2.528	0.013	40.16	0.26	125.1	1.6
98.6	12.39	1.52	4.822	0.004	1.481	0.002	54.15	0.14	123.2	0.7
101.8	15.00	1.75	5.096	0.005	1.166	0.002	57.22	0.11	122.5	0.7
111.4	11.92	1.32	6.001	0.004	4.844	0.010	66.91	0.16	121.7	0.6
120.0	14.41	1.44	5.869	0.005	4.972	0.008	65.95	0.16	122.9	0.7
148.9	17.98	1.38	6.015	0.005	1.353	0.004	67.50	0.27	121.6	1.0
176.9	21.77	2.66	6.203	0.009	1.061	0.003	69.71	0.22	121.0	1.0
203.7	15.60	1.59	5.397	0.005	2.030	0.004	60.39	0.11	121.6	0.6
224.1	20.37	2.05	5.477	0.005	2.139	0.009	61.48	0.34	121.1	1.3
241.3	16.67	2.77	5.353	0.007	2.300	0.008	60.06	0.20	121.9	1.1
250.9	15.76	1.73	4.975	0.005	1.566	0.001	55.25	0.10	119.9	0.6
252.0	16.33	1.27	3.552	0.002	1.428	0.003	39.17	0.09	118.2	0.6

Table A.2: Flowstone *SPA 59*:

Distance from Base		$\delta^{234}U$		Conc. ^{238}U		Conc. ^{232}Th		Conc. ^{230}Th		Age	
[mm]	± [mm]	[‰]	±[‰]	[µg/g]	±[µg/g]	[ng/g]	±[ng/g]	[pg/g]	±[pg/g]	[kyr]	± [kyr]
1.4	2.5	25.81	1.83	165.21	0.18	2.90	0.01	2500.62	14.75	246.5	5.8
5.4	1.5	30.57	2.35	168.10	0.24	0.97	0.01	2568.47	13.36	249.8	5.8
7.4	1.5	31.06	1.57	170.94	0.10	0.37	0.00	2599.48	5.20	244.8	2.6
19.9	2.5	55.85	2.79	100.52	0.16	0.40	0.00	1557.12	4.83	238.0	4.0
23.9	1.0	44.39	1.78	97.84	0.11	0.24	0.00	1479.53	2.66	227.1	2.2
23.9	1.0	56.42	2.03	81.09	0.10	118.30	0.22	1244.07	3.36	227.2	2.8
29.4	0.5	45.46	2.45	102.30	0.15	< 0.1		1543.12	3.09	224.3	2.8
29.7	2.5	46.29	4.22	100.07	0.29	< 0.1		1509.94	3.32	223.8	4.5
33.4	0.5	39.75	2.75	47.08	0.08	1.84	0.00	701.70	1.68	220.6	3.0
35.1	2.2	51.48	2.09	23.29	0.03	45.72	0.06	344.84	0.72	207.0	2.1
37.4	1.0	82.46	2.19	65.99	0.07	105.90	0.23	974.94	3.12	187.2	2.0
37.5	2.5	80.36	2.79	52.52	0.08	62.79	0.10	783.67	1.80	193.3	2.1
39.4	1.0	83.52	2.76	76.34	0.13	4.09	0.01	1126.94	3.94	186.2	2.3
41.9	1.0	85.24	2.77	83.46	0.14	128.72	1.08	1060.22	10.50	133.6	2.7
42.9	1.0	91.33	2.47	55.26	0.08	123.85	0.37	694.29	2.22	129.2	1.1
44.9	1.0	85.66	1.85	56.19	0.06	86.50	0.29	709.62	3.83	132.0	1.4
49.4	0.5	71.32	1.98	28.80	0.04	349.60	0.42	351.34	0.91	127.1	0.9
50.4	0.5	74.59	1.85	25.21	0.03	133.50	0.17	309.88	0.62	128.2	0.7
52.0	1.0	73.55	2.21	10.67	0.01	221.60	0.44	130.40	0.53	126.8	1.1
52.9	2.0	76.53	3.18	16.84	0.02	104.40	0.29	192.49	0.87	112.0	1.1
55.3	1.0	43.62	5.28	13.88	0.03	28.81	0.21	134.98	1.50	91.2	1.8
55.5	1.0	34.61	1.67	39.38	0.03	75.59	0.15	356.60	0.89	83.1	0.4
56.4	0.5	44.69	4.60	50.09	0.14	34.40	0.10	438.96	1.14	77.9	0.7
56.9	0.5	23.26	2.24	63.49	0.10	8.01	0.02	531.12	1.27	75.3	0.4
57.4	0.5	26.70	4.17	48.88	0.12	5.60	0.03	412.69	2.27	76.0	0.8
58.9	1.0	22.70	3.21	37.97	0.05	11.34	0.07	317.76	2.64	75.5	1.0
59.9	1.0	18.29	1.67	25.32	0.03	20.79	0.04	206.18	0.68	73.0	0.4
60.9	1.0	36.20	7.06	21.58	0.09	52.33	0.14	176.56	1.17	71.5	1.1
64.9	2.0	23.06	2.89	105.47	0.21	8.72	0.01	735.41	1.47	58.7	0.3
66.2	1.2	22.16	1.90	136.82	0.15	12.53	0.01	955.90	1.43	58.9	0.2
71.6	1.7	24.48	2.97	141.70	0.28	1.21	0.00	996.74	2.99	59.2	0.4
72.9	2.0	17.61	4.83	145.06	0.51	1.94	0.00	1006.56	2.01	58.7	0.5
82.4	2.5	22.65	5.79	59.02	0.22	0.57	0.01	395.82	5.22	55.8	1.1
91.9	2.0	30.06	3.75	55.61	0.11	1.55	0.01	369.25	3.21	54.5	0.7
99.4	2.5	18.94	2.02	51.30	0.07	3.02	0.02	332.42	1.60	53.6	0.4
107.4	2.5	15.18	2.03	30.36	0.04	79.98	0.10	191.80	0.36	52.1	0.2
112.1	2.2	20.48	2.03	30.42	0.04	72.17	0.20	199.19	1.10	54.2	0.4

Table A.3: Stalagmite *H13*:

D.f.Top [cm]	$\delta^{234}U$ [‰]	±[‰]	Conc. ^{238}U [µg/g]	±[µg/g]	Conc. ^{232}Th [ng/g]	±[ng/g]	Conc. ^{230}Th [pg/g]	±[pg/g]	Age [kyr]	± [kyr]
0.1	343.53	3.25	0.2477	0.0002	< 0.1		3.71	0.05	116.6	2.6
1	350.83	2.81	0.3141	0.0004	< 0.1		5.00	0.03	127.9	1.4
1.5	352.84	4.60	0.3166	0.0004	< 0.1		4.90	0.02	121.7	1.2
3	351.69	2.25	0.3920	0.0004	0.1650	0.0002	6.29	0.03	129.8	1.2
5	361.33	4.82	0.3591	0.0004	< 0.1		5.69	0.03	125.2	1.5
9.5	359.13	2.86	0.3202	0.0003	0.2582	0.0003	5.04	0.01	124.3	0.7
10	372.03	3.39	0.3379	0.0003	0.1454	0.0003	5.34	0.02	122.9	1
20	365.67	2.64	0.3180	0.0002	0.6822	0.0009	5.04	0.02	124.3	0.9
30	382.09	3.09	0.2514	0.0003	0.7555	0.0018	4.07	0.02	126.2	1.3
50	361.84	5.09	0.2923	0.0003	0.2089	0.0007	4.68	0.03	127.2	1.6
70	358.32	2.98	0.2876	0.0003	0.4677	0.0012	4.56	0.02	125.8	1
76	359.59	3.01	0.2710	0.0002	1.0972	0.0037	4.32	0.03	126.6	1.7
81.7	357.30	3.34	0.2707	0.0003	0.2575	0.0007	4.32	0.02	127.5	1.3
100	365.48	3.60	0.2774	0.0003	0.5111	0.0014	4.40	0.04	124.7	2
104.7	367.16	2.73	0.3440	0.0004	1.1340	0.0018	5.45	0.02	124.3	1
105	376.39	5.48	0.3192	0.0006	0.7584	0.0042	5.25	0.04	130.8	2
119	373.21	4.44	0.8899	0.0011	0.3894	0.0021	14.49	0.14	129.1	2.3
120	371.83	1.98	0.6616	0.0005	0.3531	0.0008	10.61	0.05	125.9	1.1
130	381.70	2.54	1.0802	0.0014	0.8850	0.0018	17.54	0.06	126.9	1
131.5	385.80	2.84	2.1399	0.0032	0.6063	0.0016	34.83	0.14	126.8	1.1
138	418.72	2.75	3.1676	0.0035	< 0.1		52.96	0.27	126.9	1.3
143.5	419.09	2.62	2.1862	0.0026	3.4845	0.0066	36.68	0.12	127.6	0.9
146	406.32	3.30	3.2191	0.0048	0.7667	0.0016	53.66	0.15	128.4	0.9
152	417.47	2.21	2.4925	0.0027	0.2002	0.0003	42.09	0.12	129.4	0.8
153	416.58	7.35	2.2460	0.0054	1.0459	0.0071	37.98	0.40	129.9	2.8
154	424.72	6.50	2.1640	0.0043	1.9683	0.0415	36.65	0.47	128.7	3.2
155	423.19	3.57	2.1445	0.0026	2.3413	0.0080	37.86	0.19	139.2	1.5
155.5	398.99	2.38	1.5104	0.0017	12.3863	0.0545	26.72	0.24	144.3	2.5
156	401.51	5.72	1.6877	0.0035	6.8428	0.0438	30.07	0.37	146.3	3.8
157	429.53	3.02	1.9281	0.0021	6.9800	0.0230	37.79	0.32	169.8	3.2
158	315.03	5.39	0.2238	0.0002	3.3395	0.0117	4.14	0.04	184.6	4.3
159	319.12	4.38	0.1768	0.0002	4.8354	0.0116	3.11	0.02	164.6	2.3
160	339.54	3.22	0.1952	0.0001	21.2750	0.0383	3.44	0.02	159.2	1.8

Table A.4: Stalagmite *T1* (measured by R. EICHSTÄDTER):

D.f.Top [cm]	$\delta^{234}U$ [‰]	±[‰]	Conc. ^{238}U [µg/g]	±[µg/g]	Conc. ^{232}Th [ng/g]	±[ng/g]	Conc. ^{230}Th [pg/g]	±[pg/g]	Age [kyr]	± [kyr]
7	-217.77	4.45	0.5159	0.0012	0.1526	0.0012	4.20	0.04	119.6	2.8
33	-237.82	1.91	0.5099	0.0010	<0.1		4.14	0.01	126.2	1.3
59	-226.25	3.39	0.5208	0.0010	0.1317	0.0004	4.27	0.03	124.3	2.1
88	-224.59	2.31	0.5262	0.0011	<0.1		4.30	0.02	122.6	1.5
103	-224.88	2.25	0.5794	0.0012	0.1775	0.0009	4.78	0.04	125.3	2.3
117	-230.19	3.83	0.5574	0.0010	0.1523	0.0012	4.53	0.04	123.7	2.7
120.5	-231.89	3.03	0.6986	0.0014	<0.1		5.97	0.05	138.1	2.9

Stable isotope data

Table A.5: Stalagmite *SPA 50*:

Depth [mm]	$\delta^{13}C$ [‰ PDB]	$\delta^{18}O$ [‰ PDB]	Depth [mm]	$\delta^{13}C$ [‰ PDB]	$\delta^{18}O$ [‰ PDB]	Depth [mm]	$\delta^{13}C$ [‰ PDB]	$\delta^{18}O$ [‰ PDB]
0.00	4.44	-13.12	11.10	4.61	-11.48	21.60	1.20	-11.08
0.15	5.46	-12.67	11.25	4.91	-11.44	21.75	1.43	-11.00
0.30	5.25	-12.80	11.40	4.59	-11.58	21.90	1.35	-11.09
0.45	4.77	-12.94	11.55	4.48	-11.50	22.05	1.51	-11.04
0.60	4.94	-12.95	11.70	4.30	-11.60	22.20	1.57	-11.03
0.75	5.04	-12.94	11.85	4.14	-11.66	22.35	1.99	-10.79
0.90	5.19	-12.79	12.00	3.52	-11.89	22.50	1.56	-10.99
1.05	5.55	-12.78	12.15	3.54	-11.84	22.65	1.89	-10.86
1.20	5.46	-12.65	12.30	2.97	-12.00	22.80	1.85	-10.79
1.35	5.43	-12.72	12.45	2.91	-12.01	22.95	1.96	-10.79
1.50	5.49	-12.57	12.60	2.62	-12.02	23.10	2.07	-10.70
1.65	5.60	-12.62	12.75	2.99	-11.72	23.25	1.91	-10.93
1.80	5.47	-12.41	12.90	3.19	-11.92	23.40	2.04	-10.67
1.95	5.48	-12.30	13.05	2.63	-12.08	23.55	2.11	-10.74
2.10	5.76	-12.17	13.20	2.43	-12.13	23.70	2.22	-10.68
2.40	5.99	-11.90	13.35	3.06	-11.90	23.85	2.35	-10.66
2.55	6.16	-11.76	13.50	2.19	-12.19	24.00	2.27	-10.65
2.70	6.14	-11.62	13.65	1.76	-12.29	24.15	2.39	-10.69
2.85	5.74	-11.85	13.80	1.96	-12.28	24.30	2.69	-10.53
3.00	6.18	-11.56	13.95	1.80	-12.29	24.45	2.64	-10.57
3.15	5.79	-11.64	14.10	1.61	-12.18	24.60	2.54	-10.62
3.30	5.69	-11.58	14.25	1.67	-12.19	24.90	2.67	-10.61
3.45	5.29	-11.65	14.40	1.79	-12.16	25.05	2.47	-10.64
3.60	4.90	-11.82	14.55	1.67	-12.11	25.20	2.65	-10.58
3.75	4.92	-11.85	14.70	1.91	-11.99	25.50	2.33	-10.65
3.90	4.58	-12.09	14.85	1.97	-11.99	25.65	2.41	-10.67
4.05	4.76	-12.00	15.00	2.16	-11.82	25.80	2.37	-10.78
4.35	4.93	-12.04	15.15	2.37	-11.82	25.95	2.38	-10.75
4.50	4.82	-11.93	15.30	2.57	-11.70	26.10	2.78	-10.61
4.65	4.70	-11.98	15.45	2.54	-11.74	26.25	2.39	-10.79
4.80	4.57	-11.92	15.60	2.53	-11.81	26.40	2.01	-11.02
4.95	4.57	-11.94	15.75	2.46	-11.76	26.55	2.47	-10.81
5.10	4.34	-12.03	15.90	2.49	-11.80	26.70	2.77	-10.70
5.25	4.32	-11.88	16.05	2.37	-11.82	26.85	2.38	-10.93
5.40	3.98	-12.10	16.20	2.37	-11.78	27.00	3.41	-10.42
5.55	3.65	-12.17	16.35	2.35	-11.91	27.15	3.88	-10.38
5.70	3.37	-12.35	16.50	2.17	-11.86	27.30	3.09	-10.74
5.85	3.11	-12.54	16.65	1.74	-12.04	27.45	2.63	-10.91
6.00	2.89	-12.37	16.80	1.59	-12.09	27.60	2.59	-11.06
6.15	2.67	-12.50	16.95	1.53	-12.14	27.75	2.66	-10.78
6.30	2.62	-12.45	17.10	1.21	-12.21	27.90	2.46	-10.79
6.45	2.33	-12.56	17.25	0.92	-12.29	28.05	2.48	-10.65
6.60	2.20	-12.62	17.40	0.72	-12.33	28.20	2.67	-10.61
6.75	2.19	-12.56	17.55	0.65	-12.29	28.35	2.63	-10.46
6.90	2.83	-12.35	17.70	0.61	-12.32	28.50	2.66	-10.57
7.05	3.11	-12.18	17.85	0.67	-12.26	28.65	2.67	-10.43
7.20	3.23	-12.13	18.00	0.44	-12.31	28.80	1.92	-10.25
7.35	2.58	-12.29	18.15	0.35	-12.40	28.95	1.20	-10.13
7.50	2.78	-12.22	18.30	0.50	-12.24	29.10	1.12	-9.94
7.65	3.62	-12.00	18.45	0.42	-12.20	29.25	0.69	-9.87
7.80	3.60	-11.97	18.60	0.48	-12.11	29.40	0.02	-9.64
7.95	3.71	-11.92	18.75	0.52	-12.02	29.55	-0.87	-9.45
8.10	3.61	-11.89	18.90	0.28	-12.08	29.70	-1.23	-9.44
8.25	3.95	-11.83	19.05	0.40	-12.08	29.85	-1.13	-9.43
8.40	3.64	-11.87	19.20	0.57	-11.94	30.00	-1.45	-9.29
8.55	3.91	-11.74	19.35	0.67	-11.86	30.30	-1.51	-9.26
8.70	4.08	-11.67	19.50	0.53	-11.88	30.45	-1.47	-9.21
8.85	4.30	-11.45	19.65	0.68	-11.89	30.60	-1.33	-9.28
9.00	4.43	-11.44	19.80	0.81	-11.68	30.75	-1.15	-9.27
9.15	4.52	-11.47	19.95	0.62	-11.77	30.90	-1.34	-9.27
9.30	4.71	-11.30	20.10	0.75	-11.60	31.05	-1.40	-9.21
9.45	4.24	-11.43	20.25	0.84	-11.53	31.20	-1.71	-9.24
9.60	4.67	-11.24	20.40	0.77	-11.43	31.35	-1.90	-9.32
9.90	4.60	-11.15	20.55	0.89	-11.34	31.50	-1.82	-9.31
10.05	4.65	-11.28	20.70	1.17	-11.40	31.65	-2.07	-9.31
10.20	4.94	-11.40	20.85	1.39	-11.24	31.80	-2.06	-9.36
10.50	4.99	-11.46	21.00	1.45	-11.14	31.95	-2.24	-9.31
10.65	4.91	-11.35	21.15	1.47	-10.98	32.10	-2.45	-9.41
10.80	4.70	-11.49	21.30	1.33	-11.10	32.25	-2.61	-9.40
10.95	4.62	-11.55	21.45	1.27	-11.13	32.40	-2.93	-9.54

Depth [mm]	$\delta^{13}C$ [‰ PDB]	$\delta^{18}O$ [‰ PDB]	Depth [mm]	$\delta^{13}C$ [‰ PDB]	$\delta^{18}O$ [‰ PDB]	Depth [mm]	$\delta^{13}C$ [‰ PDB]	$\delta^{18}O$ [‰ PDB]
32.55	-3.21	-9.49	43.65	-3.32	-9.87	54.75	-3.66	-9.57
32.70	-3.51	-9.52	43.80	-3.18	-9.88	54.90	-3.14	-9.40
32.85	-3.37	-9.58	43.95	-3.09	-9.97	55.05	-3.41	-9.35
33.00	-3.69	-9.66	44.10	-3.48	-9.95	55.20	-4.29	-9.22
33.15	-4.06	-9.59	44.25	-4.13	-9.83	55.35	-4.36	-9.17
33.30	-4.19	-9.71	44.55	-4.49	-9.60	55.50	-4.38	-9.52
33.45	-4.40	-9.78	44.70	-4.47	-9.70	55.65	-3.23	-9.33
33.60	-4.26	-9.70	44.85	-4.28	-9.75	55.80	-3.53	-9.73
33.75	-4.45	-9.75	45.00	-4.25	-10.02	55.95	-3.55	-9.54
33.90	-4.45	-9.70	45.15	-4.22	-9.98	56.10	-4.41	-9.82
34.05	-4.58	-9.75	45.30	-4.65	-9.84	56.25	-5.21	-9.45
34.20	-4.68	-9.60	45.45	-4.80	-9.78	56.40	-5.66	-9.72
34.35	-4.56	-9.61	45.60	-4.51	-9.80	56.55	-4.37	-9.79
34.50	-4.04	-9.64	45.75	-3.21	-9.72	56.70	-4.29	-9.59
34.65	-3.71	-9.64	45.90	-2.05	-9.42	56.85	-5.06	-9.38
34.80	-3.65	-9.72	46.05	-2.81	-9.33	57.00	-4.95	-9.28
34.95	-3.26	-9.77	46.20	-4.01	-9.37	57.15	-4.46	-9.16
35.10	-3.15	-9.85	46.35	-3.84	-9.32	57.30	-3.36	-9.28
35.25	-2.92	-9.91	46.50	-4.51	-9.44	57.45	-3.41	-9.23
35.40	-2.95	-9.87	46.65	-4.71	-9.59	57.60	-4.64	-9.27
35.55	-3.55	-9.90	46.80	-4.48	-9.57	57.75	-5.46	-9.45
35.70	-3.70	-9.87	46.95	-4.40	-9.58	57.90	-5.39	-9.33
35.85	-3.78	-9.87	47.10	-3.87	-9.40	58.05	-4.96	-9.19
36.00	-3.68	-10.01	47.25	-3.44	-9.38	58.20	-5.14	-9.47
36.15	-4.06	-9.87	47.40	-2.54	-9.18	58.35	-5.38	-9.34
36.45	-3.99	-9.76	47.55	-2.67	-9.23	58.50	-6.16	-9.32
36.60	-3.61	-9.60	47.70	-3.23	-9.46	58.65	-5.68	-9.74
36.75	-3.55	-9.53	47.85	-3.14	-9.22	58.80	-4.90	-9.38
36.90	-4.02	-9.61	48.00	-3.42	-9.28	58.95	-3.92	-9.51
37.05	-4.91	-9.82	48.15	-4.07	-9.42	59.10	-3.39	-9.85
37.20	-5.32	-9.97	48.30	-4.67	-9.57	59.25	-2.69	-9.62
37.50	-5.30	-9.99	48.45	-4.64	-9.53	59.40	-3.63	-9.38
37.65	-5.15	-9.90	48.60	-4.66	-9.56	59.55	-4.43	-9.32
37.80	-5.22	-9.95	48.75	-4.81	-9.51	59.70	-4.29	-9.37
37.95	-5.35	-9.98	48.90	-4.41	-9.51	59.85	-3.59	-9.51
38.10	-4.91	-9.86	49.05	-3.58	-9.44	60.00	-3.05	-9.73
38.25	-4.47	-9.74	49.20	-2.81	-9.05	60.15	-3.22	-9.51
38.55	-4.62	-9.88	49.35	-2.85	-9.05	60.30	-3.26	-9.73
38.70	-4.29	-9.82	49.50	-3.48	-9.27	60.45	-2.31	-9.25
38.85	-3.94	-9.80	49.65	-3.95	-9.05	60.60	-2.40	-9.34
39.00	-4.07	-9.91	49.80	-4.22	-9.08	60.75	-1.99	-9.33
39.15	-4.17	-9.90	49.95	-4.18	-9.09	60.90	-1.94	-9.43
39.30	-4.35	-9.98	50.10	-3.83	-9.07	61.05	-2.73	-9.56
39.45	-4.19	-9.95	50.25	-4.45	-9.08	61.20	-3.20	-9.65
39.60	-4.00	-9.76	50.40	-5.54	-9.17	61.35	-3.58	-9.54
39.75	-4.04	-9.76	50.55	-5.58	-9.12	61.50	-4.05	-9.51
39.90	-3.83	-9.77	50.70	-5.45	-9.08	61.65	-5.23	-9.73
40.05	-3.73	-9.66	50.85	-5.25	-9.06	61.80	-5.08	-9.55
40.20	-3.77	-9.75	51.00	-4.97	-9.02	61.95	-6.33	-9.65
40.35	-3.97	-9.76	51.15	-4.68	-9.03	62.10	-7.32	-10.00
40.50	-3.47	-9.64	51.30	-4.31	-9.02	62.25	-7.44	-9.67
40.65	-3.82	-9.65	51.45	-3.33	-8.82	62.40	-7.87	-9.64
40.80	-3.90	-9.66	51.60	-3.38	-8.95	62.55	-8.08	-9.86
40.95	-3.90	-9.68	51.75	-4.04	-9.04	62.70	-7.73	-9.39
41.10	-4.16	-9.61	51.90	-4.53	-9.08	62.85	-7.49	-9.48
41.25	-4.34	-9.66	52.05	-4.80	-9.10	63.00	-7.90	-9.46
41.40	-4.52	-9.69	52.20	-5.05	-9.21	63.15	-7.99	-9.54
41.55	-4.92	-9.86	52.35	-4.63	-9.09	63.30	-7.94	-9.57
41.70	-4.75	-9.84	52.50	-5.08	-9.31	63.45	-7.91	-9.50
41.85	-3.83	-9.72	52.65	-3.92	-9.03	63.60	-7.60	-9.42
42.00	-3.99	-9.87	52.80	-3.61	-8.88	63.75	-6.63	-9.33
42.15	-3.18	-9.85	52.95	-4.28	-8.96	63.90	-4.96	-9.23
42.30	-3.21	-9.95	53.10	-4.79	-9.03	64.05	-4.89	-9.29
42.45	-3.40	-9.95	53.25	-3.85	-9.02	64.20	-4.50	-9.21
42.60	-3.73	-9.89	53.40	-3.19	-9.03	64.35	-3.33	-9.27
42.75	-4.33	-9.97	53.85	-4.56	-9.35	64.50	-3.35	-9.15
42.90	-4.02	-9.83	54.00	-3.77	-9.32	64.65	-3.52	-9.26
43.05	-3.38	-9.63	54.15	-4.20	-9.30	64.80	-3.98	-9.35
43.20	-3.03	-9.49	54.30	-4.65	-9.44	64.95	-4.11	-9.36
43.35	-3.18	-9.61	54.45	-4.64	-9.42	65.10	-4.16	-9.30
43.50	-3.16	-9.80	54.60	-4.31	-9.46	65.25	-3.81	-9.22

Depth [mm]	$\delta^{13}C$ [‰ PDB]	$\delta^{18}O$ [‰ PDB]	Depth [mm]	$\delta^{13}C$ [‰ PDB]	$\delta^{18}O$ [‰ PDB]	Depth [mm]	$\delta^{13}C$ [‰ PDB]	$\delta^{18}O$ [‰ PDB]
65.40	-4.18	-9.28	76.20	-3.76	-8.99	86.85	-6.24	-9.45
65.55	-4.44	-9.29	76.35	-3.35	-8.90	87.00	-6.22	-9.41
65.70	-5.04	-9.35	76.50	-2.57	-8.98	87.15	-5.99	-9.27
65.85	-5.74	-9.18	76.65	-1.95	-8.79	87.30	-6.02	-9.13
66.00	-5.32	-9.20	76.80	-1.93	-8.90	87.45	-5.44	-9.19
66.15	-4.92	-9.35	76.95	-2.31	-8.98	87.60	-5.45	-9.09
66.30	-5.08	-9.70	77.10	-2.61	-8.93	87.75	-5.62	-9.11
66.45	-4.91	-9.36	77.25	-3.25	-8.98	87.90	-5.46	-9.24
66.60	-4.89	-9.33	77.40	-3.51	-9.10	88.05	-5.30	-9.23
66.75	-4.86	-9.27	77.55	-3.78	-9.31	88.20	-5.56	-9.40
66.90	-4.18	-9.14	77.70	-3.83	-9.42	88.35	-5.12	-9.17
67.05	-4.50	-9.08	77.85	-3.96	-9.37	88.50	-5.54	-9.35
67.20	-5.37	-9.15	78.00	-4.30	-9.40	88.65	-5.15	-9.19
67.35	-5.48	-9.28	78.15	-4.51	-9.31	88.80	-4.73	-9.35
67.50	-5.36	-9.44	78.30	-4.31	-9.43	88.95	-4.38	-9.17
67.65	-5.18	-9.49	78.45	-3.77	-9.32	89.10	-3.99	-9.17
67.80	-4.95	-9.54	78.60	-3.59	-9.41	89.25	-2.95	-9.01
67.95	-5.24	-9.61	78.75	-4.33	-9.13	89.40	-3.69	-8.70
68.10	-6.15	-9.65	78.90	-5.73	-9.18	89.55	-3.75	-8.77
68.25	-5.60	-9.49	79.05	-5.72	-9.14	89.70	-4.25	-8.87
68.40	-4.75	-9.43	79.20	-5.41	-9.12	89.85	-3.98	-8.97
68.55	-4.18	-9.47	79.35	-5.65	-9.08	90.00	-4.19	-9.09
68.70	-4.55	-9.33	79.50	-4.87	-8.95	90.15	-4.56	-9.08
68.85	-6.22	-9.52	79.65	-4.06	-8.93	90.30	-4.49	-9.11
69.00	-6.99	-9.71	79.80	-3.81	-8.93	90.45	-4.46	-8.95
69.15	-7.22	-9.76	79.95	-3.70	-8.98	90.60	-4.45	-9.02
69.30	-6.69	-9.75	80.10	-3.62	-9.06	90.75	-4.39	-8.86
69.45	-6.07	-9.53	80.25	-3.74	-8.88	90.90	-4.76	-9.07
69.60	-5.90	-9.49	80.40	-4.03	-9.16	91.05	-4.88	-9.05
69.75	-5.82	-9.49	80.55	-3.88	-9.24	91.20	-4.76	-9.00
69.90	-6.20	-9.67	80.70	-3.61	-9.25	91.35	-4.18	-9.05
70.05	-6.04	-9.86	80.85	-3.66	-9.07	91.50	-3.95	-9.04
70.20	-5.71	-9.65	81.00	-3.67	-8.90	91.65	-4.11	-8.99
70.35	-5.79	-9.65	81.15	-4.37	-8.95	91.80	-3.83	-9.06
70.50	-5.57	-9.64	81.30	-5.09	-9.03	91.95	-3.17	-9.07
70.65	-6.38	-9.71	81.45	-5.45	-9.10	92.10	-2.77	-9.12
70.80	-6.75	-9.64	81.60	-5.33	-9.19	92.25	-3.02	-9.08
70.95	-6.44	-9.57	81.75	-5.04	-9.21	92.40	-3.38	-9.22
71.25	-5.83	-9.40	81.90	-5.58	-9.22	92.55	-3.45	-9.41
71.40	-5.45	-9.44	82.05	-5.22	-9.09	92.70	-3.14	-9.10
71.55	-5.11	-9.35	82.20	-4.76	-9.06	92.85	-3.23	-8.97
71.70	-5.10	-9.49	82.35	-5.18	-9.27	93.00	-3.34	-9.18
71.85	-5.09	-9.75	82.50	-4.71	-8.99	93.15	-3.54	-9.22
72.00	-5.03	-9.59	82.65	-5.49	-8.97	93.30	-4.43	-9.20
72.15	-4.81	-9.53	82.80	-5.66	-8.90	93.45	-6.10	-9.05
72.30	-4.56	-9.53	82.95	-4.35	-8.90	93.60	-7.05	-9.00
72.45	-4.56	-9.44	83.10	-3.87	-9.02	93.75	-7.80	-9.19
72.60	-4.46	-9.48	83.25	-5.34	-9.04	93.90	-7.84	-9.20
72.75	-4.56	-9.41	83.40	-5.48	-9.10	94.05	-7.99	-9.59
72.90	-4.78	-9.35	83.55	-4.91	-9.06	94.20	-7.60	-9.37
73.05	-4.81	-9.43	83.70	-5.09	-9.02	94.35	-8.27	-9.29
73.20	-4.18	-9.18	83.85	-4.91	-8.94	94.50	-8.19	-9.35
73.35	-2.51	-9.03	84.00	-4.97	-8.96	94.65	-8.69	-9.52
73.50	-2.63	-8.96	84.15	-5.85	-9.13	94.80	-8.86	-9.38
73.65	-2.21	-8.86	84.30	-6.13	-9.30	94.95	-8.61	-9.23
73.80	-2.34	-8.83	84.45	-6.17	-9.21	95.10	-8.27	-9.33
73.95	-2.01	-8.93	84.60	-5.58	-9.26	95.25	-8.20	-9.45
74.10	-2.45	-8.97	84.75	-5.05	-9.00	95.40	-8.07	-9.23
74.25	-3.13	-9.02	84.90	-4.48	-9.11	95.55	-7.90	-9.21
74.40	-3.31	-9.13	85.05	-5.18	-9.15	95.70	-8.11	-9.44
74.55	-3.50	-9.18	85.20	-4.19	-9.17	95.85	-8.28	-9.28
74.70	-4.12	-9.18	85.35	-4.46	-8.97	96.15	-8.28	-9.23
74.85	-4.08	-9.11	85.50	-5.23	-9.10	96.30	-8.25	-9.11
75.00	-4.49	-9.32	85.65	-6.03	-9.26	96.45	-8.15	-9.12
75.15	-4.67	-9.11	85.80	-5.01	-9.42	96.60	-8.09	-9.09
75.30	-4.72	-9.09	85.95	-4.31	-9.36	96.75	-8.14	-9.17
75.45	-4.84	-9.10	86.10	-4.12	-9.19	96.90	-7.73	-9.07
75.60	-4.57	-9.09	86.25	-4.56	-9.38	97.05	-7.38	-8.99
75.75	-4.27	-9.00	86.40	-5.57	-9.50	97.20	-6.97	-8.78
75.90	-3.98	-9.08	86.55	-5.38	-9.31	97.35	-7.50	-8.97
76.05	-3.89	-9.25	86.70	-5.49	-9.42	97.50	-6.66	-8.75

Depth [mm]	$\delta^{13}C$ [‰ PDB]	$\delta^{18}O$ [‰ PDB]	Depth [mm]	$\delta^{13}C$ [‰ PDB]	$\delta^{18}O$ [‰ PDB]	Depth [mm]	$\delta^{13}C$ [‰ PDB]	$\delta^{18}O$ [‰ PDB]
97.65	-6.40	-8.91	108.45	-5.96	-8.99	119.10	-4.77	-8.89
97.80	-6.45	-8.94	108.60	-6.36	-9.00	119.25	-4.83	-8.86
97.95	-6.68	-9.16	108.75	-6.68	-9.11	119.40	-4.90	-8.72
98.10	-6.89	-9.44	108.90	-6.44	-8.90	119.55	-4.89	-8.69
98.25	-6.69	-9.25	109.05	-6.82	-8.81	119.70	-4.61	-8.58
98.40	-6.71	-9.13	109.20	-7.06	-8.75	119.85	-4.69	-8.72
98.55	-6.73	-9.24	109.35	-6.27	-8.75	120.00	-4.53	-8.60
98.70	-6.74	-9.39	109.50	-6.11	-8.80	120.15	-4.98	-8.67
98.85	-6.97	-9.56	109.65	-5.83	-8.75	120.30	-4.95	-8.57
99.00	-6.49	-9.38	109.80	-5.55	-8.90	120.45	-5.23	-8.66
99.15	-5.97	-9.17	109.95	-5.45	-8.94	120.60	-5.01	-8.70
99.30	-5.59	-8.94	110.10	-5.13	-8.81	120.75	-4.99	-8.63
99.45	-5.37	-8.86	110.25	-4.71	-8.92	120.90	-4.74	-8.63
99.60	-4.83	-8.89	110.40	-5.23	-9.01	121.05	-4.73	-8.66
99.75	-5.07	-8.76	110.55	-5.54	-8.90	121.20	-4.65	-8.81
99.90	-4.71	-8.71	110.70	-5.74	-8.87	121.35	-5.20	-8.93
100.05	-3.67	-8.75	110.85	-5.69	-8.87	121.50	-4.71	-8.70
100.20	-3.44	-8.80	111.00	-5.48	-8.67	121.65	-4.66	-8.93
100.35	-5.16	-8.87	111.15	-5.64	-8.81	121.80	-5.56	-9.04
100.50	-6.02	-9.07	111.30	-5.73	-8.78	121.95	-5.56	-8.95
100.65	-5.42	-8.92	111.45	-4.58	-8.62	122.10	-5.66	-9.06
100.80	-4.69	-8.83	111.60	-3.29	-8.61	122.25	-5.86	-9.01
100.95	-3.28	-8.86	111.75	-2.03	-8.36	122.40	-5.99	-9.10
101.10	-3.20	-8.79	111.90	-2.21	-8.18	122.55	-6.41	-9.17
101.25	-4.60	-8.86	112.05	-1.93	-8.36	122.70	-6.64	-9.11
101.40	-5.32	-8.77	112.20	-2.36	-8.35	122.85	-6.66	-9.25
101.55	-5.34	-8.67	112.35	-2.88	-8.34	123.00	-5.80	-9.13
101.70	-4.66	-8.54	112.50	-4.32	-8.57	123.15	-5.46	-9.21
101.85	-3.31	-8.55	112.65	-4.83	-8.75	123.30	-5.37	-9.09
102.00	-3.41	-8.64	112.80	-3.90	-8.60	123.45	-5.64	-9.07
102.15	-2.62	-8.69	112.95	-3.29	-8.40	123.60	-6.01	-9.10
102.30	-4.17	-8.57	113.10	-2.99	-8.19	123.75	-6.37	-9.14
102.45	-5.65	-8.82	113.25	-2.36	-8.03	123.90	-6.43	-9.12
102.60	-6.56	-8.68	113.40	-2.04	-8.12	124.05	-6.26	-9.08
102.75	-8.14	-8.71	113.55	-2.81	-8.24	124.20	-6.29	-9.04
102.90	-7.89	-8.73	113.70	-3.07	-8.30	124.35	-6.16	-8.93
103.05	-8.90	-8.56	113.85	-3.95	-8.52	124.50	-6.47	-9.03
103.20	-8.22	-8.55	114.00	-4.69	-8.70	124.65	-6.32	-8.93
103.35	-7.61	-8.62	114.15	-5.33	-8.97	124.80	-6.12	-8.99
103.50	-7.49	-8.51	114.30	-5.50	-9.04	124.95	-5.78	-8.87
103.65	-6.42	-8.70	114.45	-5.86	-9.03	125.10	-5.51	-8.98
103.80	-4.82	-8.63	114.60	-6.32	-9.22	125.25	-5.44	-8.93
103.95	-3.36	-8.36	114.75	-6.38	-9.27	125.40	-5.77	-8.92
104.10	-3.16	-8.46	114.90	-6.18	-9.27	125.55	-5.61	-8.94
104.25	-4.21	-8.63	115.05	-5.54	-9.15	125.70	-6.28	-9.09
104.55	-4.26	-8.73	115.20	-5.21	-9.08	125.85	-6.03	-9.10
104.70	-3.32	-8.40	115.35	-5.16	-8.98	126.00	-5.44	-9.01
104.85	-3.76	-8.36	115.50	-4.76	-8.83	126.15	-6.00	-8.92
105.00	-4.62	-8.35	115.65	-4.92	-8.96	126.30	-6.66	-9.05
105.15	-4.55	-8.53	115.80	-4.97	-8.82	126.45	-7.19	-9.02
105.30	-3.37	-8.72	115.95	-5.62	-9.05	126.60	-6.89	-9.05
105.45	-3.20	-8.70	116.10	-5.74	-8.91	126.75	-7.00	-8.98
105.60	-3.58	-8.90	116.25	-5.91	-8.92	126.90	-7.01	-8.89
105.75	-3.10	-8.93	116.40	-5.97	-8.80	127.05	-6.37	-9.03
105.90	-2.67	-8.66	116.55	-5.63	-8.62	127.20	-6.34	-8.87
106.05	-2.45	-8.37	116.70	-5.68	-8.57	127.35	-6.54	-8.82
106.20	-3.31	-8.54	116.85	-5.70	-8.65	127.50	-6.88	-8.80
106.35	-3.93	-8.64	117.00	-5.71	-8.61	127.65	-6.62	-8.85
106.50	-4.85	-8.77	117.15	-5.71	-8.62	127.80	-6.67	-8.80
106.65	-4.54	-8.64	117.30	-5.50	-8.45	127.95	-6.42	-8.84
106.80	-4.46	-8.64	117.45	-5.98	-8.63	128.10	-6.58	-8.85
106.95	-4.23	-8.55	117.60	-5.67	-8.52	128.25	-6.68	-8.82
107.10	-4.03	-8.76	117.75	-5.74	-8.65	128.40	-6.64	-8.80
107.25	-3.61	-8.75	117.90	-5.20	-8.59	128.55	-5.88	-8.72
107.40	-4.28	-8.89	118.05	-5.25	-8.71	128.70	-5.87	-8.71
107.55	-4.14	-8.84	118.20	-4.90	-8.78	128.85	-6.47	-8.72
107.70	-4.88	-8.86	118.35	-4.74	-8.76	129.00	-6.37	-8.75
107.85	-5.53	-9.00	118.50	-4.29	-8.69	129.15	-6.05	-8.78
108.00	-6.16	-9.00	118.65	-4.58	-8.71	129.30	-6.41	-8.79
108.15	-6.04	-9.00	118.80	-4.52	-8.95	129.45	-6.32	-8.72
108.30	-5.86	-8.99	118.95	-4.64	-8.95	129.90	-6.33	-8.67

Depth [mm]	$\delta^{13}C$ [‰ PDB]	$\delta^{18}O$ [‰ PDB]	Depth [mm]	$\delta^{13}C$ [‰ PDB]	$\delta^{18}O$ [‰ PDB]	Depth [mm]	$\delta^{13}C$ [‰ PDB]	$\delta^{18}O$ [‰ PDB]
130.05	-6.46	-8.83	140.70	-3.56	-8.68	151.35	-6.49	-8.88
130.20	-6.49	-8.79	140.85	-3.65	-8.79	151.50	-6.52	-8.93
130.35	-4.82	-8.61	141.00	-3.80	-9.05	151.65	-6.52	-8.76
130.50	-5.27	-8.66	141.15	-3.61	-8.82	151.80	-6.27	-8.84
130.65	-5.24	-8.70	141.30	-3.59	-8.87	151.95	-6.09	-8.86
130.80	-5.13	-8.62	141.45	-3.42	-8.86	152.10	-6.08	-8.88
130.95	-4.87	-8.63	141.60	-3.74	-9.02	152.25	-6.11	-8.83
131.10	-4.77	-8.64	141.75	-3.73	-8.92	152.40	-6.04	-8.72
131.25	-4.61	-8.50	141.90	-3.65	-8.83	152.55	-5.85	-8.67
131.40	-4.38	-8.57	142.05	-4.02	-9.03	152.70	-5.51	-8.56
131.55	-4.43	-8.61	142.20	-3.94	-8.88	152.85	-4.86	-8.86
131.70	-4.48	-8.54	142.35	-3.84	-8.84	153.00	-5.10	-8.76
131.85	-4.02	-8.57	142.50	-3.47	-8.91	153.15	-5.20	-8.68
132.00	-4.04	-8.51	142.65	-3.49	-8.97	153.30	-5.00	-8.79
132.15	-4.06	-8.45	142.80	-4.37	-9.05	153.45	-4.64	-8.76
132.30	-4.53	-8.53	142.95	-5.84	-9.19	153.60	-4.34	-8.84
132.60	-4.29	-8.49	143.10	-6.58	-9.21	153.75	-4.23	-8.84
132.75	-3.82	-8.45	143.25	-5.79	-9.25	153.90	-4.18	-8.80
132.90	-3.70	-8.44	143.40	-5.11	-9.13	154.05	-4.22	-8.84
133.05	-3.62	-8.34	143.55	-3.82	-8.96	154.35	-4.77	-8.78
133.20	-3.92	-8.31	143.70	-3.60	-9.03	154.50	-4.74	-8.85
133.35	-4.98	-8.44	143.85	-4.03	-9.08	154.65	-5.17	-8.76
133.50	-4.37	-8.37	144.00	-5.06	-8.89	154.80	-5.35	-8.85
133.65	-5.03	-8.49	144.15	-6.31	-9.12	155.25	-6.12	-8.87
133.80	-5.14	-8.56	144.30	-6.43	-9.05	155.40	-5.86	-8.84
133.95	-5.47	-8.68	144.45	-6.69	-9.03	155.55	-5.28	-8.91
134.10	-5.61	-8.65	144.60	-6.12	-9.07	155.70	-4.91	-8.78
134.25	-5.62	-8.62	144.75	-5.06	-8.99	155.85	-4.52	-8.84
134.40	-5.24	-8.66	144.90	-4.50	-8.96	156.00	-4.30	-8.81
134.55	-6.13	-8.74	145.05	-4.35	-9.03	156.15	-4.01	-8.73
134.70	-6.13	-8.86	145.20	-4.85	-9.15	156.30	-3.96	-8.73
134.85	-5.99	-8.91	145.35	-4.64	-9.20	156.45	-4.03	-8.77
135.00	-6.43	-8.91	145.50	-4.86	-9.22	156.60	-4.20	-8.71
135.15	-6.57	-8.96	145.65	-5.16	-9.40	156.75	-4.32	-8.80
135.30	-6.36	-8.84	145.80	-4.95	-9.26	156.90	-4.75	-8.77
135.45	-6.48	-8.87	145.95	-4.42	-9.26	157.05	-5.51	-8.76
135.60	-6.55	-8.85	146.10	-4.10	-9.22	157.20	-6.07	-8.75
135.75	-6.64	-8.86	146.25	-4.21	-9.14	157.35	-5.87	-8.62
135.90	-6.44	-8.77	146.40	-4.18	-9.14	157.50	-6.11	-8.66
136.05	-6.44	-8.82	146.55	-3.79	-9.05	157.65	-5.93	-8.60
136.20	-6.34	-8.82	146.70	-3.78	-8.98	157.80	-4.94	-8.40
136.35	-5.58	-8.80	146.85	-3.98	-8.95	157.95	-4.42	-8.42
136.50	-5.66	-8.76	147.00	-4.60	-8.97	158.10	-4.49	-8.50
136.65	-5.35	-8.81	147.15	-4.74	-8.93	158.25	-4.49	-8.45
136.80	-5.18	-8.89	147.30	-5.06	-9.06	158.40	-4.22	-8.72
136.95	-5.07	-8.79	147.45	-5.25	-9.03	158.70	-4.55	-8.84
137.10	-4.54	-8.77	147.60	-5.36	-9.02	158.85	-4.42	-8.84
137.25	-4.44	-8.66	147.75	-5.86	-9.09	159.00	-4.54	-8.96
137.40	-4.00	-8.52	147.90	-6.25	-9.22	159.15	-4.65	-8.87
137.55	-3.86	-8.55	148.05	-6.48	-9.39	159.30	-4.96	-8.93
137.70	-3.61	-8.59	148.20	-6.78	-9.46	159.45	-5.16	-8.99
137.85	-3.09	-8.66	148.35	-6.56	-9.35	159.60	-5.22	-8.86
138.00	-3.53	-8.64	148.50	-7.32	-9.36	159.90	-5.81	-9.02
138.15	-3.29	-8.60	148.65	-7.44	-9.41	160.05	-5.99	-9.11
138.30	-3.26	-8.64	148.80	-7.22	-9.33	160.20	-6.25	-9.16
138.45	-3.35	-8.71	148.95	-6.62	-9.35	160.35	-6.67	-9.17
138.60	-3.25	-8.59	149.10	-6.59	-9.36	160.50	-6.46	-9.09
138.75	-3.39	-8.75	149.25	-5.80	-9.20	160.65	-6.42	-9.13
138.90	-3.45	-8.66	149.40	-5.61	-9.23	160.80	-6.23	-9.16
139.05	-3.61	-8.77	149.55	-5.64	-9.20	160.95	-6.13	-9.08
139.20	-3.71	-8.68	149.70	-5.36	-9.20	161.10	-5.97	-9.27
139.35	-3.66	-8.59	149.85	-5.56	-9.19	161.25	-5.68	-8.97
139.50	-3.76	-8.80	150.00	-5.24	-9.18	161.40	-5.53	-9.08
139.65	-3.65	-8.79	150.15	-4.73	-9.14	161.55	-5.39	-8.96
139.80	-3.65	-8.75	150.30	-4.77	-9.07	161.70	-5.03	-9.16
139.95	-3.69	-8.82	150.45	-4.77	-9.02	162.00	-5.31	-8.91
140.10	-3.58	-8.62	150.60	-5.01	-8.95	162.15	-5.53	-9.07
140.25	-3.65	-8.76	150.75	-5.32	-9.03	162.30	-5.92	-9.11
140.40	-3.47	-8.64	151.05	-6.23	-8.93	162.45	-6.70	-9.16
140.55	-3.65	-8.60	151.20	-6.63	-8.93	162.60	-7.16	-9.09

Depth [mm]	$\delta^{13}C$ [‰ PDB]	$\delta^{18}O$ [‰ PDB]	Depth [mm]	$\delta^{13}C$ [‰ PDB]	$\delta^{18}O$ [‰ PDB]	Depth [mm]	$\delta^{13}C$ [‰ PDB]	$\delta^{18}O$ [‰ PDB]
162.75	-7.41	-8.98	173.85	-6.18	-8.96	184.65	-7.72	-9.33
162.90	-7.79	-9.15	174.00	-5.15	-8.96	184.80	-7.52	-9.36
163.05	-7.99	-9.38	174.15	-4.79	-9.00	184.95	-7.16	-9.24
163.20	-8.15	-9.26	174.30	-5.48	-8.97	185.10	-6.80	-9.28
163.35	-7.64	-9.13	174.45	-6.18	-9.05	185.25	-6.62	-9.27
163.50	-7.47	-9.18	174.60	-6.26	-8.91	185.40	-6.73	-9.37
163.65	-7.08	-9.15	174.75	-6.04	-8.89	185.55	-6.89	-9.36
163.80	-7.45	-9.12	174.90	-5.55	-8.89	185.85	-7.08	-9.38
163.95	-7.60	-9.39	175.05	-5.31	-8.82	186.00	-6.92	-9.49
164.10	-7.36	-9.14	175.20	-5.14	-8.72	186.15	-6.90	-9.40
164.25	-7.24	-9.24	175.35	-5.27	-8.97	186.30	-6.59	-9.31
164.40	-7.38	-9.29	175.50	-4.78	-8.87	186.45	-6.66	-9.27
164.55	-7.35	-9.19	175.65	-4.89	-8.74	186.60	-6.25	-9.29
164.70	-6.76	-9.17	175.80	-5.13	-8.72	186.75	-6.14	-9.26
164.85	-5.28	-9.08	175.95	-5.39	-8.70	186.90	-6.91	-9.34
165.00	-5.35	-9.27	176.10	-6.04	-8.77	187.05	-8.20	-9.45
165.15	-6.48	-9.03	176.25	-6.53	-8.73	187.20	-8.82	-9.48
165.30	-6.25	-9.00	176.40	-6.57	-8.62	187.35	-8.49	-9.28
165.45	-5.30	-9.02	176.55	-6.22	-8.56	187.50	-9.64	-9.38
165.60	-5.42	-9.08	176.70	-6.41	-8.67	187.65	-9.61	-9.38
165.75	-5.78	-9.05	176.85	-5.79	-8.57	187.80	-9.18	-9.29
166.20	-5.28	-8.91	177.00	-6.20	-8.64	187.95	-7.24	-9.04
166.35	-6.08	-8.85	177.15	-6.14	-8.63	188.10	-7.80	-9.13
166.50	-5.83	-9.06	177.30	-6.71	-8.60	188.25	-7.72	-9.17
166.65	-5.47	-9.01	177.45	-6.36	-8.66	188.40	-7.29	-9.15
166.80	-6.28	-9.10	177.60	-6.86	-8.70	188.55	-6.62	-9.19
166.95	-5.63	-9.00	177.75	-6.58	-8.76	188.70	-6.64	-9.11
167.10	-6.12	-9.03	177.90	-6.26	-8.75	188.85	-6.74	-9.08
167.25	-5.86	-8.98	178.05	-6.64	-8.88	189.00	-7.05	-9.16
167.40	-5.82	-9.00	178.20	-6.90	-8.84	189.15	-6.97	-9.11
167.55	-5.64	-8.94	178.35	-5.96	-8.88	189.30	-7.54	-9.27
167.70	-5.39	-8.95	178.50	-6.20	-8.95	189.45	-7.21	-9.16
167.85	-5.20	-8.88	178.65	-5.97	-9.08	189.60	-6.37	-9.18
168.00	-4.47	-8.76	178.80	-5.29	-9.01	189.75	-6.38	-9.17
168.15	-4.89	-8.85	178.95	-5.20	-9.07	189.90	-6.39	-9.21
168.30	-5.19	-8.81	179.10	-4.67	-9.07	190.05	-6.57	-9.25
168.45	-5.66	-8.74	179.25	-4.35	-9.10	190.20	-6.59	-9.05
168.60	-5.85	-8.86	179.40	-4.32	-9.09	190.35	-5.09	-9.06
168.75	-6.30	-8.79	179.55	-4.45	-9.01	190.50	-5.32	-8.93
168.90	-5.82	-8.82	179.70	-4.55	-9.00	190.65	-5.43	-8.94
169.05	-6.11	-8.89	179.85	-5.04	-8.92	190.80	-5.62	-9.08
169.20	-5.87	-8.90	180.00	-5.04	-8.97	190.95	-5.88	-9.13
169.35	-5.89	-8.91	180.15	-5.17	-8.99	191.10	-6.04	-8.97
169.50	-5.22	-8.88	180.30	-5.11	-8.89	191.25	-5.46	-8.99
169.65	-5.37	-8.88	180.45	-5.10	-8.89	191.40	-5.40	-9.00
169.80	-5.28	-8.89	180.75	-5.45	-8.91	191.55	-5.30	-8.93
169.95	-5.41	-8.98	180.90	-5.89	-8.93	191.70	-5.70	-8.98
170.10	-5.30	-8.92	181.05	-6.13	-8.95	191.85	-5.20	-9.00
170.25	-5.14	-8.97	181.20	-6.15	-9.00	192.00	-5.50	-8.97
170.40	-4.81	-8.96	181.35	-6.85	-9.04	192.15	-5.42	-8.96
170.70	-4.55	-9.03	181.50	-7.05	-9.02	192.30	-5.54	-9.03
170.85	-4.38	-9.01	181.65	-7.39	-9.07	192.45	-5.61	-8.98
171.00	-4.52	-9.00	181.80	-7.30	-8.99	192.60	-5.72	-8.95
171.15	-5.03	-8.99	181.95	-7.33	-9.00	192.75	-5.60	-8.94
171.30	-4.65	-9.03	182.10	-7.34	-8.96	192.90	-5.66	-8.98
171.45	-5.56	-9.05	182.25	-7.17	-8.94	193.05	-6.03	-9.08
171.60	-5.44	-9.05	182.40	-6.97	-9.02	193.20	-6.39	-9.04
171.75	-5.55	-9.03	182.55	-6.92	-9.05	193.35	-6.58	-9.01
171.90	-5.40	-8.93	182.70	-6.89	-9.13	193.50	-6.87	-9.12
172.05	-5.28	-8.98	182.85	-6.93	-9.10	193.65	-6.90	-9.04
172.20	-4.66	-9.03	183.00	-7.22	-9.05	193.80	-6.81	-9.09
172.35	-4.45	-9.03	183.15	-7.39	-9.10	193.95	-6.91	-9.10
172.50	-3.47	-9.03	183.30	-7.42	-9.15	194.10	-6.74	-8.93
172.65	-3.62	-8.94	183.45	-7.59	-9.21	194.25	-6.79	-9.02
172.80	-3.64	-8.85	183.60	-7.51	-9.18	194.40	-6.61	-8.90
172.95	-3.87	-8.92	183.75	-7.32	-9.21	194.55	-6.88	-8.91
173.10	-4.09	-9.00	183.90	-7.11	-9.17	194.70	-6.77	-8.90
173.25	-5.00	-8.91	184.05	-7.50	-9.21	194.85	-6.66	-9.05
173.40	-5.28	-8.87	184.20	-7.52	-9.21	195.00	-6.46	-8.93
173.55	-4.88	-8.87	184.35	-7.68	-9.24	195.15	-6.67	-9.00
173.70	-5.02	-9.04	184.50	-7.71	-9.26	195.30	-6.67	-8.98

Depth [mm]	$\delta^{13}C$ [‰ PDB]	$\delta^{18}O$ [‰ PDB]	Depth [mm]	$\delta^{13}C$ [‰ PDB]	$\delta^{18}O$ [‰ PDB]	Depth [mm]	$\delta^{13}C$ [‰ PDB]	$\delta^{18}O$ [‰ PDB]
195.45	-6.83	-9.00	206.40	-6.24	-9.35	217.50	-6.00	-9.00
195.60	-7.24	-9.11	206.55	-5.86	-9.42	217.65	-5.89	-8.98
195.75	-7.68	-9.20	206.70	-5.89	-9.49	217.80	-5.98	-9.16
195.90	-7.85	-9.21	206.85	-6.10	-9.36	217.95	-6.32	-9.18
196.05	-7.98	-9.12	207.00	-6.10	-9.22	218.10	-6.55	-9.29
196.20	-8.14	-9.12	207.15	-6.36	-9.32	218.25	-6.81	-9.23
196.35	-7.20	-9.04	207.30	-6.25	-9.45	218.40	-6.99	-9.17
196.50	-6.66	-8.93	207.45	-6.86	-9.40	218.55	-7.30	-9.20
196.65	-6.12	-9.13	207.60	-6.54	-9.23	218.70	-7.43	-9.27
196.80	-6.86	-9.13	207.75	-7.04	-9.27	218.85	-6.94	-9.20
196.95	-7.39	-9.15	207.90	-7.41	-9.29	219.00	-7.33	-9.21
197.10	-8.24	-9.20	208.05	-7.17	-9.31	219.15	-6.63	-9.20
197.25	-7.88	-9.22	208.20	-7.17	-9.18	219.30	-7.25	-9.37
197.40	-8.09	-9.14	208.35	-7.28	-9.10	219.45	-7.04	-9.30
197.55	-7.76	-9.21	208.50	-7.25	-9.18	219.60	-7.42	-9.24
197.70	-7.52	-9.22	208.65	-6.84	-9.13	219.75	-7.84	-9.34
197.85	-7.60	-9.21	208.80	-5.81	-9.13	219.90	-7.66	-9.37
198.00	-7.21	-9.20	208.95	-5.32	-9.05	220.05	-7.40	-9.22
198.15	-6.32	-9.11	209.10	-5.66	-9.10	220.20	-7.41	-9.11
198.30	-6.17	-9.17	209.40	-7.06	-9.47	220.35	-7.67	-9.04
198.45	-6.41	-9.12	209.55	-7.02	-9.53	220.50	-7.62	-9.07
198.60	-6.51	-9.17	210.00	-6.68	-9.28	220.65	-7.28	-9.20
198.75	-6.19	-9.16	210.15	-6.32	-9.41	220.80	-7.23	-9.11
198.90	-6.48	-9.25	210.30	-5.98	-9.16	220.95	-7.44	-9.18
199.05	-6.96	-9.23	210.45	-6.09	-9.18	221.10	-7.27	-9.22
199.20	-7.65	-9.20	210.60	-5.86	-9.16	221.25	-7.23	-9.24
199.35	-7.60	-9.15	210.75	-5.94	-9.27	221.40	-6.88	-9.24
199.50	-8.28	-9.20	210.90	-5.48	-9.07	221.55	-7.10	-9.25
199.65	-7.71	-9.00	211.05	-5.60	-8.85	221.70	-7.42	-9.24
199.80	-7.14	-9.05	211.20	-5.95	-8.89	221.85	-7.06	-9.04
199.95	-7.00	-9.11	211.35	-6.27	-9.03	222.00	-7.40	-9.14
200.10	-6.52	-9.07	211.50	-6.84	-9.03	222.15	-7.17	-9.06
200.25	-7.11	-9.16	211.65	-6.56	-8.93	222.30	-6.75	-9.09
200.40	-8.29	-9.21	211.80	-6.70	-9.07	222.45	-6.48	-9.03
200.55	-8.29	-9.15	211.95	-6.47	-9.00	222.90	-5.87	-8.92
200.70	-8.27	-8.92	212.10	-6.56	-9.05	223.05	-5.75	-9.02
200.85	-8.25	-8.87	212.25	-6.20	-9.18	223.20	-5.34	-8.93
201.00	-8.74	-9.10	212.40	-5.45	-9.08	223.35	-5.24	-8.90
201.15	-8.43	-8.90	212.55	-5.37	-9.02	223.50	-5.12	-8.99
201.30	-7.45	-8.84	212.70	-5.66	-9.06	223.65	-5.24	-9.01
201.45	-7.40	-8.81	212.85	-5.58	-9.01	223.80	-5.03	-8.90
201.60	-7.33	-8.84	213.00	-5.57	-8.98	223.95	-4.86	-8.95
201.75	-7.19	-8.83	213.15	-5.94	-8.93	224.10	-4.69	-8.91
201.90	-7.02	-8.90	213.30	-5.96	-9.10	224.25	-4.62	-8.83
202.05	-7.21	-9.04	213.45	-6.36	-9.11	224.40	-4.55	-8.81
202.20	-7.58	-9.01	213.60	-7.02	-9.17	224.55	-4.65	-8.81
202.35	-7.37	-8.96	213.75	-7.48	-9.35	224.70	-4.59	-8.67
202.50	-7.56	-9.03	213.90	-7.47	-9.22	224.85	-4.87	-8.69
202.80	-6.87	-8.94	214.05	-7.78	-9.15	225.00	-4.71	-8.75
203.10	-5.92	-8.82	214.20	-8.15	-9.11	225.15	-4.80	-8.71
203.25	-5.73	-8.89	214.35	-8.34	-9.08	225.30	-5.05	-8.81
203.40	-5.75	-8.79	214.50	-8.19	-8.93	225.45	-5.29	-8.79
203.55	-6.09	-8.79	214.65	-8.99	-9.03	225.60	-5.41	-8.84
203.70	-6.06	-8.89	214.80	-9.21	-8.96	225.75	-5.84	-8.72
203.85	-6.20	-8.83	214.95	-9.30	-8.95	225.90	-6.03	-8.86
204.00	-5.82	-8.81	215.10	-9.34	-8.84	226.05	-6.34	-8.90
204.15	-5.71	-8.90	215.25	-8.59	-8.99	226.20	-6.35	-8.81
204.30	-6.15	-8.75	215.40	-8.20	-8.96	226.35	-6.61	-8.96
204.45	-6.30	-9.00	215.55	-7.95	-8.97	226.50	-6.74	-9.01
204.60	-6.12	-9.00	215.70	-7.80	-9.11	226.65	-6.62	-9.03
204.75	-6.40	-9.14	215.85	-7.91	-9.29	226.80	-6.61	-9.07
204.90	-6.79	-9.35	216.00	-7.97	-9.46	226.95	-6.98	-9.33
205.05	-6.95	-9.34	216.15	-7.10	-9.19	227.10	-7.50	-9.33
205.20	-6.89	-9.40	216.30	-6.69	-8.92	227.25	-7.18	-9.43
205.35	-6.48	-9.25	216.45	-6.58	-8.87	227.40	-6.79	-9.24
205.50	-5.94	-9.30	216.60	-5.46	-8.75	227.55	-6.86	-9.34
205.65	-6.36	-9.27	216.75	-4.86	-8.68	227.70	-6.88	-9.37
205.80	-6.61	-9.29	216.90	-4.87	-8.59	227.85	-6.68	-9.30
205.95	-6.58	-9.28	217.05	-4.93	-8.66	228.00	-6.29	-9.29
206.10	-6.27	-9.25	217.20	-5.48	-8.88	228.15	-6.55	-9.23
206.25	-5.74	-9.49	217.35	-6.00	-9.08	228.30	-6.52	-9.22

Depth [mm]	$\delta^{13}C$ [‰ PDB]	$\delta^{18}O$ [‰ PDB]
228.45	-6.43	-9.36
228.60	-6.46	-9.36
228.75	-6.59	-9.33
228.90	-6.08	-9.23
229.05	-5.77	-9.40
229.20	-6.31	-9.33
229.35	-6.35	-9.43
229.50	-6.63	-9.52
229.80	-7.43	-9.54
229.95	-7.62	-9.52
230.10	-7.50	-9.46
230.25	-7.02	-9.48
230.40	-6.20	-9.44
230.55	-5.13	-9.51
230.70	-4.15	-9.49
230.85	-4.85	-9.51
231.15	-4.35	-9.36
231.30	-4.55	-9.36
231.45	-4.93	-9.40
231.60	-5.22	-9.39
231.75	-4.74	-9.33
231.90	-4.58	-9.33
232.05	-4.70	-9.26
232.20	-4.96	-9.26
232.35	-5.21	-9.37
232.50	-5.46	-9.29
232.65	-6.24	-9.38
232.80	-6.36	-9.30
232.95	-6.66	-9.35
233.10	-6.24	-9.28
233.25	-6.08	-9.22
233.40	-5.78	-9.15
233.55	-6.10	-9.25
233.70	-6.32	-9.07
233.85	-6.43	-9.18
234.00	-6.42	-9.13
234.15	-6.67	-9.04
234.30	-5.97	-9.11
234.45	-5.88	-8.98
234.60	-5.93	-8.96
234.75	-5.78	-8.89
234.90	-6.00	-8.81
235.05	-5.91	-8.84
235.20	-5.95	-8.82
235.35	-5.90	-8.78
235.50	-5.81	-8.86
235.65	-5.78	-8.88
235.95	-6.10	-9.08
236.10	-5.61	-9.10
236.25	-6.01	-9.06
236.40	-6.20	-9.12
236.55	-5.56	-9.04
236.70	-6.29	-9.15
236.85	-5.85	-9.35
237.00	-5.81	-9.41
237.15	-5.54	-9.20
237.30	-6.19	-9.45
237.45	-6.27	-9.25
237.60	-6.28	-9.38
237.75	-6.16	-9.23
237.90	-6.53	-9.27
238.05	-5.72	-9.11
238.20	-5.33	-9.13
238.35	-6.93	-9.43
238.50	-7.02	-9.36
238.65	-7.06	-9.44
238.80	-6.12	-9.36
238.95	-6.36	-9.49
239.10	-7.00	-9.41
239.25	-6.70	-9.27
239.40	-6.14	-9.15
239.55	-6.60	-9.08
239.70	-6.17	-9.18
239.85	-6.28	-9.34
240.00	-7.76	-9.50
240.15	-8.62	-9.51
240.30	-8.00	-9.48
240.45	-6.88	-9.45
240.60	-5.49	-9.33
240.75	-5.42	-9.28
240.90	-6.10	-9.30
241.05	-6.26	-9.29
241.20	-6.94	-9.21
241.35	-8.17	-9.18
241.50	-6.79	-8.90
241.65	-6.13	-8.53
241.80	-5.82	-8.48
241.95	-6.15	-8.59
242.10	-7.16	-8.73
242.25	-6.83	-8.65
242.40	-6.59	-8.63
242.55	-5.75	-8.66
242.70	-5.03	-8.47
242.85	-6.18	-8.76
243.00	-6.64	-8.89
243.15	-8.00	-9.08
243.30	-9.02	-9.29
243.45	-9.33	-9.20
243.60	-9.61	-9.22
243.75	-9.37	-9.21
243.90	-9.16	-8.93
244.20	-8.56	-9.10
244.35	-9.20	-9.07
244.50	-8.91	-9.06
244.65	-7.98	-9.10
244.95	-6.70	-9.15
245.10	-7.05	-10.19
245.25	-7.73	-9.76
245.40	-8.41	-9.60
245.55	-8.84	-9.48
245.70	-8.41	-9.36
245.85	-7.40	-9.28
246.00	-6.74	-9.01
246.15	-6.90	-8.99
246.30	-6.70	-9.01
246.45	-6.64	-9.22
246.60	-7.30	-9.14
246.75	-7.45	-9.14
246.90	-6.58	-9.43
247.05	-5.88	-8.65
247.20	-5.43	-8.48
247.35	-6.06	-8.58
247.50	-6.47	-8.74
247.65	-6.82	-8.73
247.80	-6.41	-8.56
247.95	-6.54	-8.58
248.10	-6.48	-8.56
248.25	-6.88	-8.68
248.40	-5.93	-8.76
248.55	-4.22	-8.28
248.70	-3.69	-8.36
248.85	-3.58	-8.42
249.00	-3.03	-8.35
249.15	-4.17	-8.42
249.30	-4.60	-8.53
249.60	-7.80	-8.81
249.75	-7.38	-8.71
249.90	-7.75	-8.96
250.05	-7.73	-9.05
250.20	-7.98	-9.26
250.35	-7.73	-9.34
250.50	-7.82	-9.44
250.80	-8.72	-9.18
250.95	-8.49	-9.17
251.10	-8.13	-9.04
251.25	-6.79	-8.97
251.40	-6.92	-8.66
251.55	-6.76	-8.68
251.70	-7.15	-8.88
251.85	-5.82	-8.78
252.00	-6.17	-8.88
252.15	-4.75	-8.85
252.30	-3.95	-8.77
252.45	-4.03	-8.88
252.60	-3.78	-8.77
252.75	-3.61	-8.77
252.90	-3.71	-8.73
253.05	-3.83	-8.72
253.20	-4.36	-8.53
253.35	-5.00	-8.57
253.50	-4.43	-8.51
253.65	-4.48	-8.31
253.80	-4.24	-8.43
253.95	-8.60	-9.07
254.10	-10.91	-9.23
254.25	-9.60	-9.07
254.40	-6.93	-8.83
254.55	-6.82	-8.84
254.70	-6.75	-8.88
254.85	-6.74	-8.85
255.00	-7.25	-9.22
255.15	-6.72	-9.12
255.30	-4.71	-9.07

Table A.6: Flowstone *SPA 59*:

Depth [mm]	$\delta^{13}C$ [‰ PDB]	$\delta^{18}O$ [‰ PDB]	Depth [mm]	$\delta^{13}C$ [‰ PDB]	$\delta^{18}O$ [‰ PDB]	Depth [mm]	$\delta^{13}C$ [‰ PDB]	$\delta^{18}O$ [‰ PDB]
0.0	1.40	-14.24	7.1	1.33	-14.05	14.2	0.59	-14.45
0.1	1.09	-14.31	7.2	1.35	-14.05	14.3	0.43	-14.46
0.2	1.02	-14.44	7.3	1.66	-13.83	14.4	0.20	-14.66
0.3	0.89	-14.71	7.4	1.41	-13.96	14.5	0.11	-14.59
0.4	0.52	-14.90	7.5	1.26	-14.03	14.6	0.05	-14.74
0.5	0.24	-15.14	7.6	1.29	-14.11	14.7	-0.13	-14.84
0.6	0.10	-15.28	7.7	1.63	-13.97	14.8	-0.20	-14.79
0.7	-0.05	-15.30	7.8	1.80	-14.00	14.9	-0.09	-14.88
0.8	-0.18	-15.35	7.9	2.37	-13.82	15.0	-0.37	-14.83
0.9	-0.08	-15.38	8.0	2.40	-13.69	15.1	-0.34	-14.78
1.0	-0.28	-15.52	8.1	2.44	-13.68	15.2	-0.44	-14.83
1.1	-0.13	-15.43	8.2	2.36	-13.56	15.3	-0.43	-14.68
1.2	-0.13	-15.40	8.3	2.42	-13.58	15.4	-0.39	-14.68
1.3	-0.09	-15.42	8.4	2.11	-13.75	15.5	-0.45	-14.73
1.4	-0.15	-15.49	8.5	2.04	-13.82	15.6	-0.47	-14.79
1.5	-0.14	-15.39	8.6	1.90	-13.76	15.7	-0.35	-14.80
1.6	-0.20	-15.41	8.7	1.33	-14.09	15.8	-0.15	-14.60
1.7	-0.17	-15.40	8.8	1.34	-14.01	15.9	-0.01	-14.70
1.8	-0.20	-15.38	8.9	1.07	-13.96	16.0	0.16	-14.44
1.9	-0.09	-15.38	9.0	0.94	-14.12	16.1	0.22	-14.48
2.0	0.03	-15.15	9.1	0.91	-14.03	16.2	0.18	-14.55
2.1	0.04	-15.12	9.2	0.90	-14.01	16.3	0.16	-14.46
2.2	0.16	-15.17	9.3	0.78	-14.07	16.4	-0.02	-14.47
2.3	0.09	-15.15	9.4	0.78	-14.17	16.5	-0.02	-14.55
2.4	0.02	-15.13	9.5	0.79	-14.15	16.6	0.24	-14.59
2.5	-0.02	-15.27	9.6	0.69	-14.23	16.7	0.45	-14.57
2.6	-0.09	-15.15	9.7	0.69	-14.28	16.8	0.64	-14.40
2.7	0.04	-15.04	9.8	0.71	-14.29	16.9	0.74	-14.49
2.8	0.00	-15.13	9.9	0.46	-14.37	17.0	0.93	-14.35
2.9	-0.09	-15.12	10.0	0.54	-14.41	17.1	0.89	-14.39
3.0	-0.16	-15.31	10.1	0.50	-14.29	17.2	0.81	-14.31
3.1	-0.17	-15.31	10.2	0.55	-14.49	17.3	0.69	-14.37
3.2	-0.21	-15.30	10.3	0.39	-14.42	17.4	0.57	-14.47
3.3	-0.11	-15.30	10.4	0.41	-14.45	17.5	0.55	-14.40
3.4	-0.04	-15.27	10.5	0.32	-14.47	17.6	0.35	-14.44
3.5	-0.21	-15.21	10.6	0.29	-14.43	17.7	0.14	-14.73
3.6	-0.09	-15.13	10.7	0.18	-14.55	17.8	0.07	-14.56
3.7	-0.16	-15.21	10.8	0.17	-14.43	17.9	-0.04	-14.54
3.8	-0.10	-15.09	10.9	-0.02	-14.61	18.0	-0.04	-14.56
3.9	0.04	-15.04	11.0	0.13	-14.65	18.1	-0.05	-14.55
4.0	-0.12	-15.15	11.1	0.07	-14.61	18.2	-0.06	-14.53
4.1	0.03	-15.08	11.2	0.16	-14.55	18.3	0.32	-14.43
4.2	0.08	-14.98	11.3	0.09	-14.62	18.4	1.69	-13.98
4.3	0.10	-14.95	11.4	-0.04	-14.68	18.5	3.29	-13.60
4.4	0.04	-15.04	11.5	-0.11	-14.68	18.6	4.32	-13.40
4.5	-0.12	-15.17	11.6	-0.14	-14.81	18.7	3.98	-13.48
4.6	0.00	-15.09	11.7	-0.37	-14.91	18.8	7.29	-12.47
4.7	-0.13	-15.19	11.8	-0.39	-14.72	18.9	5.82	-12.77
4.8	-0.17	-15.14	11.9	-0.24	-14.82	19.0	8.38	-12.06
4.9	-0.11	-15.09	12.0	-0.17	-14.70	19.1	7.98	-11.98
5.0	-0.08	-15.02	12.1	-0.18	-14.53	19.2	7.28	-12.14
5.1	0.01	-15.04	12.2	-0.20	-14.58	19.3	7.16	-12.40
5.2	0.04	-15.06	12.3	-0.18	-14.67	19.4	7.46	-12.06
5.3	0.12	-14.75	12.4	-0.05	-14.57	19.5	7.54	-11.97
5.4	0.12	-14.77	12.5	-0.11	-14.50	19.6	6.97	-12.22
5.5	0.27	-14.63	12.6	0.02	-14.49	19.7	6.51	-12.07
5.6	0.34	-14.62	12.7	-0.09	-14.61	19.8	7.32	-12.13
5.7	0.60	-14.57	12.8	0.06	-14.62	19.9	7.05	-12.10
5.8	0.76	-14.51	12.9	0.05	-14.94	20.0	6.93	-12.18
5.9	1.00	-14.47	13.0	0.28	-14.72	20.1	6.83	-12.14
6.0	0.99	-14.42	13.1	0.37	-14.67	20.2	6.59	-12.15
6.1	1.09	-14.24	13.2	0.59	-14.49	20.3	6.25	-12.11
6.2	1.26	-14.34	13.3	0.87	-14.32	20.4	6.16	-12.04
6.3	1.15	-14.27	13.4	0.73	-14.38	20.5	6.23	-12.15
6.4	1.07	-14.43	13.5	1.09	-14.15	20.6	6.23	-12.17
6.5	1.05	-14.35	13.6	1.54	-14.14	20.7	6.25	-12.01
6.6	1.15	-14.31	13.7	1.51	-14.16	20.8	6.43	-11.62
6.7	1.20	-14.24	13.8	1.45	-14.21	20.9	5.97	-11.43
6.8	1.11	-14.30	13.9	1.13	-14.26	21.0	5.80	-11.61
6.9	1.00	-14.42	14.0	0.82	-14.28	21.1	4.14	-12.41
7.0	1.17	-14.14	14.1	0.59	-14.32	21.2	2.68	-13.49

Depth [mm]	$\delta^{13}C$ [‰ PDB]	$\delta^{18}O$ [‰ PDB]	Depth [mm]	$\delta^{13}C$ [‰ PDB]	$\delta^{18}O$ [‰ PDB]	Depth [mm]	$\delta^{13}C$ [‰ PDB]	$\delta^{18}O$ [‰ PDB]
21.3	1.37	-13.98	28.4	5.19	-11.43	35.6	-0.69	-13.33
21.4	0.32	-14.27	28.5	4.41	-11.68	35.7	-0.48	-13.24
21.5	-0.01	-14.40	28.6	3.35	-11.97	35.8	-0.75	-13.34
21.6	-0.26	-14.52	28.7	2.31	-12.27	35.9	-0.84	-13.13
21.7	-0.53	-14.73	28.8	2.70	-11.95	36.0	-0.54	-13.07
21.8	-1.10	-14.86	28.9	4.00	-11.72	36.1	-0.13	-13.00
21.9	-1.68	-15.11	29.0	4.30	-11.66	36.2	0.16	-12.79
22.0	-1.87	-15.15	29.1	4.62	-11.62	36.3	0.60	-12.52
22.1	-1.97	-15.16	29.2	4.13	-11.71	36.4	0.67	-12.50
22.2	-1.96	-15.23	29.3	3.17	-12.00	36.5	0.93	-12.35
22.3	-1.71	-15.06	29.4	2.56	-12.15	36.6	1.23	-12.26
22.4	-1.31	-14.96	29.5	3.28	-11.90	36.7	1.62	-11.85
22.5	-1.48	-14.98	29.6	4.28	-11.76	36.8	2.30	-11.56
22.6	-1.81	-14.96	29.7	4.69	-11.61	36.9	2.30	-10.86
22.7	-2.56	-15.20	29.8	5.11	-11.45	37.0	2.31	-11.06
22.8	-2.84	-15.19	29.9	5.43	-11.38	37.1	2.83	-10.99
22.9	-2.29	-14.95	30.0	5.44	-11.38	37.2	2.70	-10.52
23.0	-2.39	-15.04	30.1	4.99	-11.55	37.3	2.55	-10.08
23.1	-1.81	-14.79	30.2	4.92	-11.51	37.4	2.89	-10.36
23.2	-1.13	-14.59	30.3	5.22	-11.43	37.5	2.34	-10.35
23.3	-1.15	-14.63	30.4	6.13	-11.13	37.6	2.31	-10.86
23.4	-0.58	-14.32	30.5	7.78	-10.69	37.7	2.30	-11.09
23.5	0.10	-14.13	30.6	8.36	-10.54	37.8	2.30	-11.37
23.6	0.44	-13.94	30.7	8.80	-10.45	37.9	1.74	-11.86
23.7	0.74	-13.78	30.8	9.25	-10.40	38.0	2.46	-11.88
23.8	1.25	-13.58	30.9	9.27	-10.36	38.1	2.38	-11.94
23.9	1.67	-13.34	31.0	8.40	-10.65	38.2	2.14	-12.14
24.0	2.46	-13.18	31.1	6.54	-10.87	38.3	1.94	-12.21
24.1	2.86	-13.19	31.2	4.31	-11.41	38.4	1.40	-12.43
24.2	3.61	-13.05	31.3	2.32	-11.82	38.5	1.37	-12.27
24.3	3.85	-13.12	31.4	1.01	-12.22	38.6	1.35	-12.32
24.4	6.70	-12.18	31.5	0.45	-12.36	38.7	1.88	-12.15
24.5	8.62	-11.40	31.6	0.77	-12.26	38.8	1.93	-12.14
24.6	8.24	-11.24	31.7	1.07	-12.19	38.9	2.12	-12.21
24.7	0.96	-12.68	31.8	1.47	-12.09	39.0	2.00	-12.16
24.8	0.45	-12.94	31.9	1.29	-12.28	39.1	2.31	-12.08
24.9	0.41	-12.94	32.0	1.52	-12.15	39.2	2.29	-12.16
25.0	0.39	-13.03	32.1	1.69	-12.20	39.3	2.44	-12.02
25.1	0.38	-13.01	32.2	1.89	-12.23	39.4	2.80	-11.97
25.2	0.39	-13.04	32.3	2.20	-12.07	39.5	2.86	-11.85
25.3	0.70	-12.91	32.4	2.53	-11.84	39.6	3.28	-11.83
25.4	1.37	-12.66	32.5	2.55	-12.08	39.7	3.37	-11.76
25.5	2.36	-12.28	32.6	2.43	-12.15	39.8	3.45	-11.78
25.6	3.44	-11.96	32.7	2.19	-12.40	39.9	3.61	-11.68
25.7	4.18	-11.67	32.8	2.50	-12.16	40.0	3.74	-11.65
25.8	4.88	-11.51	32.9	1.45	-12.55	40.1	4.11	-11.54
25.9	3.73	-12.25	33.0	1.10	-12.76	40.2	4.36	-11.40
26.0	2.38	-12.27	33.1	1.20	-12.58	40.3	4.15	-11.55
26.1	2.49	-12.15	33.2	1.06	-12.79	40.4	4.06	-11.63
26.2	3.52	-11.84	33.3	0.71	-12.78	40.5	4.16	-11.64
26.3	3.73	-11.76	33.4	0.35	-12.88	40.6	3.89	-11.81
26.4	3.32	-11.79	33.5	0.05	-13.03	40.7	4.08	-11.80
26.5	2.15	-12.18	33.6	-0.10	-13.02	40.8	4.11	-11.89
26.6	1.33	-12.48	33.7	0.02	-12.77	40.9	4.06	-12.60
26.7	0.79	-12.69	33.8	-0.10	-12.92	41.0	3.83	-12.35
26.8	0.17	-12.76	33.9	-0.29	-13.14	41.1	3.58	-12.38
26.9	0.17	-12.90	34.0	-0.06	-12.89	41.2	3.58	-12.64
27.0	-0.24	-13.08	34.1	-0.74	-12.73	41.3	4.01	-12.66
27.1	0.19	-13.00	34.2	-0.57	-12.84	41.4	4.59	-12.60
27.2	1.21	-12.71	34.3	-0.84	-12.89	41.5	4.33	-12.69
27.3	2.42	-12.18	34.4	-0.40	-12.75	41.6	4.82	-12.93
27.4	4.25	-11.80	34.5	0.00	-12.72	41.7	4.90	-13.22
27.5	5.44	-11.48	34.6	0.11	-12.84	41.8	5.32	-13.33
27.6	5.44	-11.44	34.7	0.37	-12.70	41.9	6.61	-13.47
27.7	4.82	-11.74	34.8	0.76	-12.74	42.0	6.29	-13.23
27.8	4.16	-11.79	34.9	0.21	-12.90	42.1	7.47	-13.34
27.9	3.84	-11.80	35.1	-0.11	-13.05	42.2	7.54	-13.25
28.0	3.51	-12.04	35.2	-0.11	-13.10	42.3	8.15	-13.31
28.1	3.79	-11.87	35.3	-0.19	-13.10	42.4	8.41	-13.30
28.2	4.58	-11.69	35.4	-0.33	-13.29	42.5	9.05	-13.01
28.3	5.13	-11.40	35.5	-0.52	-13.31	42.6	9.43	-12.96

Depth [mm]	$\delta^{13}C$ [‰ PDB]	$\delta^{18}O$ [‰ PDB]	Depth [mm]	$\delta^{13}C$ [‰ PDB]	$\delta^{18}O$ [‰ PDB]	Depth [mm]	$\delta^{13}C$ [‰ PDB]	$\delta^{18}O$ [‰ PDB]
42.7	9.79	-12.91	50.2	1.94	-12.11	57.5	1.98	-11.64
42.8	10.06	-12.86	50.3	1.97	-12.16	57.6	2.07	-11.62
42.9	9.97	-12.85	50.4	1.92	-12.21	57.7	1.87	-11.60
43.0	10.20	-12.89	50.5	1.83	-12.28	57.8	1.71	-11.72
43.1	10.18	-12.88	50.6	2.18	-12.09	57.9	1.58	-11.67
43.2	10.34	-12.64	50.7	2.42	-12.04	58.0	1.78	-11.48
43.3	10.84	-12.46	50.8	2.49	-12.03	58.1	1.31	-11.69
43.4	11.05	-12.27	50.9	2.94	-11.54	58.2	1.29	-11.61
43.5	11.08	-12.16	51.0	3.04	-10.88	58.3	1.46	-11.46
43.6	11.00	-11.93	51.1	2.36	-10.80	58.4	1.24	-11.65
43.8	10.83	-11.76	51.2	1.99	-10.42	58.5	1.17	-11.54
43.9	10.32	-11.83	51.3	1.83	-10.20	58.6	1.10	-11.72
44.0	9.99	-11.74	51.4	1.31	-9.76	58.7	0.88	-11.80
44.1	10.37	-11.76	51.5	0.48	-9.30	58.8	0.92	-12.02
44.2	9.95	-11.74	51.6	0.55	-8.98	58.9	1.19	-11.81
44.3	9.72	-11.75	51.7	-0.04	-8.62	59.0	1.09	-11.79
44.4	9.87	-11.66	51.8	-0.67	-8.64	59.1	1.00	-11.89
44.5	9.09	-11.75	51.9	-0.50	-8.56	59.2	1.16	-11.81
44.6	8.86	-11.80	52.0	-0.75	-8.75	59.3	1.05	-11.89
44.7	8.14	-11.93	52.1	-0.88	-8.50	59.4	0.97	-11.91
44.8	8.24	-11.95	52.2	-1.13	-8.59	59.5	0.84	-12.05
44.9	7.66	-12.13	52.3	-1.03	-8.69	59.6	1.10	-11.88
45.0	7.70	-12.10	52.4	-1.19	-8.55	59.7	0.94	-12.05
45.1	7.41	-12.12	52.5	-1.07	-8.62	59.8	1.03	-12.20
45.2	6.91	-12.20	52.6	-1.38	-8.77	59.9	0.98	-12.09
45.3	6.69	-12.48	52.7	-1.43	-9.15	60.0	0.89	-12.15
45.4	6.34	-12.38	52.9	-1.47	-9.72	60.1	0.92	-12.26
45.5	6.24	-12.42	53.0	-1.21	-10.22	60.2	0.84	-12.28
45.6	6.26	-12.38	53.1	-1.08	-10.58	60.3	0.79	-12.31
45.7	6.17	-12.30	53.2	-0.53	-11.05	60.4	0.63	-12.44
45.8	6.03	-12.37	53.3	-0.22	-11.24	60.5	0.75	-12.55
45.9	6.20	-12.22	53.4	0.44	-11.62	60.6	0.50	-12.57
46.0	6.24	-12.20	53.5	0.36	-11.87	60.7	0.48	-12.57
46.1	6.09	-12.22	53.6	0.61	-12.25	60.8	0.66	-12.79
46.2	5.98	-12.15	53.7	0.52	-12.56	60.9	0.57	-12.60
46.3	5.75	-12.13	53.8	0.95	-12.64	61.0	0.41	-12.64
46.4	5.55	-12.22	53.9	0.43	-12.79	61.1	0.46	-12.61
46.5	5.13	-12.14	54.1	0.75	-12.86	61.2	0.48	-12.60
46.6	4.87	-12.29	54.2	0.97	-12.89	61.3	0.49	-12.77
46.9	4.42	-12.29	54.3	1.13	-12.98	61.4	0.49	-12.64
47.0	4.24	-12.40	54.4	1.29	-13.03	61.5	0.43	-12.91
47.1	4.10	-12.33	54.5	1.32	-13.08	61.6	0.32	-12.77
47.2	3.85	-12.39	54.6	1.57	-12.98	61.7	0.29	-13.52
47.4	3.23	-12.51	54.7	1.70	-13.03	61.9	-0.09	-13.08
47.5	2.98	-12.53	54.8	2.09	-13.04	62.0	0.02	-13.02
47.6	2.84	-12.62	54.9	1.85	-13.09	62.1	0.04	-13.08
47.7	2.72	-12.44	55.0	2.00	-13.11	62.2	-0.09	-13.47
47.8	2.78	-12.51	55.1	1.89	-13.14	62.3	-0.14	-13.27
47.9	2.81	-12.52	55.2	1.96	-13.30	62.4	0.09	-13.24
48.0	2.67	-12.50	55.3	1.98	-13.16	62.5	0.14	-13.21
48.1	2.52	-12.48	55.4	1.99	-13.24	62.6	0.19	-13.36
48.2	2.46	-12.51	55.5	2.15	-13.10	62.7	0.24	-13.46
48.3	2.12	-12.57	55.6	2.23	-13.13	62.8	-0.01	-14.01
48.4	2.13	-12.48	55.7	2.10	-13.29	62.9	0.06	-13.84
48.5	2.12	-12.52	55.8	2.16	-13.33	63.0	-0.07	-13.73
48.6	1.75	-12.54	55.9	2.15	-13.34	63.1	0.22	-13.97
48.7	1.55	-12.47	56.0	2.35	-13.46	63.2	0.68	-13.65
48.8	1.43	-12.44	56.1	2.45	-13.20	63.3	0.90	-13.58
48.9	1.45	-12.46	56.2	2.66	-13.17	63.4	1.44	-13.43
49.0	1.23	-12.38	56.3	3.25	-12.94	63.5	1.89	-13.14
49.1	1.19	-12.37	56.4	3.36	-12.67	63.6	2.66	-13.03
49.2	1.19	-12.39	56.5	3.78	-12.33	63.7	3.38	-12.63
49.3	1.40	-12.39	56.6	3.72	-12.17	63.8	4.64	-11.95
49.4	1.35	-12.28	56.7	3.58	-11.99	63.9	2.86	-12.73
49.5	1.48	-12.20	56.8	2.89	-11.79	64.0	2.44	-12.80
49.6	1.71	-12.26	56.9	2.90	-11.91	64.1	2.83	-12.75
49.7	1.86	-12.18	57.0	2.18	-12.14	64.2	2.35	-13.06
49.8	1.91	-12.12	57.1	2.51	-11.70	64.3	2.40	-12.83
49.9	1.98	-12.12	57.2	2.42	-11.52	64.4	2.38	-12.98
50.0	1.97	-12.18	57.3	2.11	-11.57	64.5	2.33	-12.93
50.1	1.95	-12.13	57.4	2.47	-11.67	64.6	2.69	-12.83

Depth [mm]	$\delta^{13}C$ [‰ PDB]	$\delta^{18}O$ [‰ PDB]	Depth [mm]	$\delta^{13}C$ [‰ PDB]	$\delta^{18}O$ [‰ PDB]	Depth [mm]	$\delta^{13}C$ [‰ PDB]	$\delta^{18}O$ [‰ PDB]
64.7	3.48	-12.45	71.8	1.53	-13.01	79.0	0.98	-13.68
64.8	2.52	-12.56	71.9	0.81	-12.99	79.1	0.73	-13.83
64.9	3.49	-12.28	72.0	1.00	-12.96	79.2	0.86	-13.93
65.0	3.53	-12.21	72.1	1.25	-12.95	79.3	1.28	-13.79
65.1	3.02	-12.39	72.2	1.32	-12.96	79.4	0.71	-13.98
65.2	3.26	-12.14	72.3	1.61	-12.80	79.5	1.00	-13.84
65.3	3.04	-12.17	72.4	1.79	-12.86	79.6	0.54	-13.84
65.4	2.96	-12.25	72.5	2.08	-12.79	79.7	0.47	-13.73
65.5	3.09	-12.33	72.6	2.35	-12.63	79.8	0.55	-13.61
65.6	2.81	-12.41	72.7	2.21	-12.63	79.9	0.26	-13.80
65.7	2.32	-12.40	72.8	2.15	-12.80	80.0	0.01	-13.96
65.8	1.95	-12.49	72.9	2.30	-12.58	80.1	0.23	-13.90
65.9	2.25	-12.51	73.0	1.83	-12.63	80.2	0.48	-14.00
66.0	2.51	-12.42	73.1	1.41	-12.66	80.3	0.71	-14.07
66.1	2.42	-12.41	73.2	1.23	-12.88	80.4	1.43	-14.03
66.2	2.29	-12.54	73.3	1.43	-12.68	80.5	2.31	-13.66
66.3	2.40	-12.48	73.4	1.24	-12.72	80.6	3.05	-13.46
66.4	2.56	-12.27	73.5	0.98	-12.91	80.7	3.17	-13.43
66.5	2.09	-12.40	73.6	0.88	-12.97	80.8	3.22	-13.41
66.6	2.24	-12.44	73.7	1.04	-12.95	80.9	2.74	-13.45
66.7	2.22	-12.39	73.8	1.39	-12.88	81.0	1.87	-13.83
66.8	2.22	-12.48	73.9	1.17	-12.98	81.1	1.63	-13.60
66.9	2.25	-12.32	74.0	1.13	-12.95	81.2	1.48	-13.51
67.0	2.01	-12.58	74.1	0.88	-13.02	81.3	1.51	-13.50
67.1	2.14	-12.34	74.3	0.92	-12.83	81.5	0.45	-13.45
67.2	2.28	-12.43	74.4	0.88	-12.90	81.6	0.20	-13.47
67.3	2.33	-12.45	74.5	0.92	-12.82	81.7	0.09	-13.17
67.4	2.26	-12.39	74.6	0.92	-12.67	81.8	-0.10	-13.24
67.5	2.13	-12.64	74.7	1.01	-12.84	81.9	-0.29	-13.40
67.6	1.99	-12.62	74.8	0.42	-13.00	82.0	-0.21	-13.21
67.7	2.29	-12.43	74.9	0.63	-12.98	82.1	-0.17	-13.30
67.8	2.58	-12.34	75.0	0.51	-12.90	82.2	-0.25	-13.47
67.9	2.61	-12.38	75.1	0.63	-12.98	82.3	-0.33	-13.55
68.0	2.34	-12.53	75.2	0.56	-13.12	82.4	-0.43	-13.69
68.1	2.35	-12.52	75.3	0.51	-13.04	82.5	-0.32	-13.76
68.2	2.37	-12.56	75.4	0.48	-12.99	82.6	-0.16	-13.89
68.3	2.57	-12.40	75.5	0.70	-12.87	82.7	0.04	-13.65
68.4	2.33	-12.62	75.6	0.77	-12.82	82.8	0.13	-13.56
68.5	2.48	-12.61	75.7	1.22	-12.71	82.9	0.40	-13.39
68.6	2.73	-12.55	75.8	1.87	-12.42	83.0	0.48	-13.13
68.7	2.58	-12.57	75.9	1.80	-12.38	83.1	0.26	-13.00
68.8	1.75	-12.81	76.0	2.12	-12.33	83.2	0.27	-13.22
68.9	2.22	-12.75	76.1	2.32	-12.26	83.3	0.72	-12.78
69.0	2.09	-12.84	76.2	2.38	-12.22	83.4	0.89	-12.82
69.1	1.89	-12.84	76.3	2.22	-12.30	83.5	0.97	-12.65
69.2	1.73	-12.88	76.4	1.89	-12.32	83.6	0.62	-12.76
69.3	1.14	-13.10	76.5	1.60	-12.63	83.7	0.61	-12.78
69.4	0.98	-13.31	76.6	1.47	-12.59	83.8	0.38	-12.87
69.5	0.92	-13.11	76.7	1.67	-12.66	83.9	0.01	-13.01
69.6	0.72	-13.06	76.8	1.62	-12.84	84.0	-0.21	-13.01
69.7	1.18	-12.93	76.9	2.22	-12.49	84.1	-0.72	-13.21
69.8	0.35	-13.10	77.0	2.08	-12.49	84.2	-0.81	-13.33
69.9	0.81	-13.04	77.1	1.71	-12.71	84.3	-1.14	-13.46
70.0	0.29	-13.14	77.2	1.87	-12.70	84.4	-1.09	-13.42
70.1	-0.13	-13.12	77.3	1.80	-12.73	84.5	-1.19	-13.51
70.2	-0.22	-13.23	77.4	1.72	-12.80	84.6	-1.62	-13.69
70.3	-0.38	-13.36	77.5	1.90	-12.85	84.7	-1.87	-13.81
70.4	-0.42	-13.60	77.6	2.33	-12.81	84.8	-1.89	-13.75
70.5	-0.51	-13.40	77.7	1.89	-12.89	84.9	-1.93	-13.83
70.6	-0.43	-13.33	77.8	2.16	-13.05	85.0	-1.86	-13.67
70.7	-0.42	-13.34	77.9	2.07	-13.03	85.1	-2.15	-13.69
70.8	0.08	-13.26	78.0	2.05	-13.06	85.2	-2.20	-13.78
70.9	-0.06	-13.37	78.1	2.29	-13.07	85.3	-2.18	-13.79
71.0	-0.19	-13.18	78.2	1.92	-13.40	85.4	-2.22	-13.88
71.1	-0.14	-13.20	78.3	1.98	-13.18	85.5	-2.35	-13.85
71.2	0.08	-13.15	78.4	1.53	-13.28	85.6	-2.19	-13.90
71.3	0.23	-12.98	78.5	1.51	-13.33	85.7	-2.14	-13.71
71.4	0.08	-13.14	78.6	1.82	-13.27	85.8	-2.19	-13.91
71.5	0.22	-13.04	78.7	1.70	-13.37	85.9	-2.13	-13.85
71.6	0.63	-12.85	78.8	0.94	-13.56	86.0	-2.16	-13.85
71.7	0.80	-12.92	78.9	0.85	-13.63	86.1	-2.17	-13.83

Depth [mm]	$\delta^{13}C$ [‰ PDB]	$\delta^{18}O$ [‰ PDB]	Depth [mm]	$\delta^{13}C$ [‰ PDB]	$\delta^{18}O$ [‰ PDB]	Depth [mm]	$\delta^{13}C$ [‰ PDB]	$\delta^{18}O$ [‰ PDB]
86.2	-2.13	-13.95	93.4	4.96	-12.35	100.5	0.76	-13.15
86.3	-2.15	-13.94	93.5	4.35	-12.53	100.6	0.81	-13.17
86.4	-2.02	-13.95	93.6	3.65	-12.64	100.7	0.96	-13.19
86.5	-2.03	-14.05	93.7	2.84	-12.80	100.8	1.08	-13.25
86.6	-2.16	-14.03	93.8	2.57	-13.03	100.9	1.32	-13.14
86.7	-2.17	-14.13	93.9	2.44	-13.10	101.0	1.41	-12.99
86.8	-1.96	-14.03	94.0	2.20	-13.22	101.1	1.28	-13.14
86.9	-1.91	-13.95	94.1	2.11	-13.30	101.2	1.25	-13.22
87.0	-1.90	-13.91	94.2	2.14	-13.20	101.3	1.36	-13.14
87.1	-1.91	-13.98	94.3	2.28	-13.23	101.4	1.49	-13.01
87.2	-1.80	-14.01	94.4	2.24	-13.14	101.5	1.68	-12.94
87.3	-1.63	-13.79	94.5	2.43	-13.01	101.6	1.66	-12.96
87.4	-1.63	-13.91	94.6	2.50	-12.84	101.7	1.90	-13.00
87.5	-1.47	-13.87	94.7	2.77	-12.65	101.8	1.63	-13.01
87.6	-1.27	-13.76	94.8	3.20	-12.25	101.9	1.87	-12.88
87.7	-1.40	-13.87	94.9	3.23	-12.37	102.0	1.87	-12.89
87.8	-1.35	-13.79	95.0	3.52	-12.25	102.1	1.62	-12.88
87.9	-1.36	-13.92	95.1	3.70	-12.20	102.2	1.80	-12.93
88.0	-1.34	-13.86	95.2	3.81	-12.14	102.3	1.56	-13.05
88.1	-1.43	-13.73	95.3	3.70	-12.18	102.4	0.98	-13.35
88.2	-1.47	-13.76	95.4	3.77	-12.13	102.5	0.89	-13.29
88.3	-1.46	-13.76	95.5	3.47	-12.28	102.6	0.29	-13.43
88.4	-1.48	-13.78	95.6	3.40	-12.31	102.7	-0.01	-13.56
88.5	-1.44	-13.78	95.7	3.42	-12.33	102.8	-0.54	-13.74
88.6	-1.39	-13.72	95.8	3.68	-12.16	102.9	-0.61	-13.87
88.7	-1.43	-13.74	95.9	3.59	-12.20	103.0	-1.26	-14.11
88.8	-1.05	-13.63	96.0	3.65	-12.04	103.1	-1.74	-14.16
88.9	-1.30	-13.67	96.1	3.64	-12.04	103.2	-1.64	-14.14
89.0	-1.29	-13.59	96.2	3.72	-12.02	103.3	-2.01	-14.20
89.1	-1.31	-13.61	96.3	3.55	-11.99	103.4	-2.40	-14.29
89.2	-1.31	-13.60	96.4	3.28	-12.12	103.5	-2.39	-14.26
89.3	-1.27	-13.64	96.5	3.55	-12.24	103.6	-2.21	-14.27
89.4	-1.26	-13.63	96.6	3.09	-12.48	103.7	-2.72	-14.28
89.5	-1.19	-13.66	96.7	3.21	-12.26	103.8	-2.18	-14.32
89.6	-1.05	-13.68	96.8	2.56	-12.49	103.9	-2.82	-14.43
89.7	-1.13	-13.69	96.9	2.77	-12.38	104.0	-2.87	-14.44
89.8	-0.74	-13.64	97.0	2.83	-12.28	104.1	-2.96	-14.46
89.9	-0.96	-13.72	97.1	2.42	-12.58	104.2	-3.00	-14.46
90.0	-0.58	-13.63	97.2	2.46	-12.56	104.3	-2.96	-14.37
90.1	-0.56	-13.67	97.3	2.36	-12.55	104.4	-3.05	-14.61
90.2	-0.45	-13.64	97.4	2.38	-12.53	104.5	-3.00	-14.59
90.3	-0.27	-13.55	97.5	2.35	-12.62	104.6	-2.99	-14.59
90.4	-0.27	-13.68	97.6	2.16	-12.69	104.7	-2.98	-14.57
90.5	-0.01	-13.64	97.7	2.01	-12.73	104.8	-3.05	-14.71
90.6	0.04	-13.75	97.8	1.73	-13.01	104.9	-3.26	-14.81
90.7	0.14	-13.62	97.9	1.82	-13.02	105.0	-3.18	-14.77
90.8	0.17	-13.75	98.0	1.77	-12.90	105.1	-3.16	-14.81
90.9	0.09	-13.80	98.1	1.77	-12.95	105.2	-3.10	-14.83
91.0	0.16	-13.85	98.2	1.72	-13.02	105.3	-3.21	-14.86
91.1	0.11	-13.91	98.3	1.60	-12.90	105.4	-3.20	-14.69
91.2	-0.01	-14.02	98.4	1.63	-12.98	105.5	-3.16	-14.68
91.4	-0.36	-14.13	98.5	1.59	-12.97	105.6	-3.20	-14.61
91.5	0.02	-14.41	98.6	1.70	-13.07	105.7	-3.15	-14.59
91.6	-0.01	-14.21	98.7	1.57	-13.02	105.8	-3.17	-14.61
91.7	0.41	-14.07	98.8	1.45	-13.00	105.9	-3.14	-14.61
91.8	1.76	-13.49	98.9	1.24	-13.03	106.0	-3.07	-14.56
91.9	1.72	-13.48	99.0	1.19	-13.01	106.1	-3.01	-14.49
92.0	2.06	-13.43	99.1	1.20	-13.04	106.2	-3.11	-14.58
92.1	2.56	-13.30	99.2	1.25	-13.01	106.3	-3.00	-14.52
92.2	3.36	-13.04	99.3	1.06	-13.03	106.4	-3.11	-14.58
92.3	4.07	-12.82	99.4	1.09	-13.15	106.5	-3.04	-14.60
92.4	4.04	-12.79	99.5	1.11	-12.77	106.6	-3.00	-14.52
92.5	4.83	-12.56	99.6	1.12	-12.92	106.7	-2.85	-14.43
92.6	5.39	-12.33	99.7	1.05	-13.05	106.8	-3.07	-14.38
92.7	5.56	-12.30	99.8	0.78	-13.12	106.9	-2.75	-14.49
92.8	5.35	-12.24	99.9	1.00	-13.04	107.0	-2.99	-14.58
92.9	5.88	-12.18	100.0	1.08	-13.04	107.1	-3.19	-14.70
93.0	5.83	-12.05	100.1	1.13	-13.07	107.2	-3.23	-14.67
93.1	5.83	-12.05	100.2	1.05	-13.19	107.3	-3.15	-14.59
93.2	5.71	-12.06	100.3	1.06	-13.09	107.4	-3.17	-14.64
93.3	5.30	-12.15	100.4	0.88	-13.11	107.5	-3.04	-14.63

Depth [mm]	$\delta^{13}C$ [‰ PDB]	$\delta^{18}O$ [‰ PDB]	Depth [mm]	$\delta^{13}C$ [‰ PDB]	$\delta^{18}O$ [‰ PDB]	Depth [mm]	$\delta^{13}C$ [‰ PDB]	$\delta^{18}O$ [‰ PDB]
107.6	-2.88	-14.55	110.6	-3.20	-14.72	113.5	-2.22	-14.91
107.7	-3.12	-14.50	110.7	-3.29	-14.64	113.6	-2.62	-15.07
107.8	-3.15	-14.57	110.8	-3.21	-14.68	113.7	-2.89	-15.09
107.9	-3.24	-14.60	110.9	-3.09	-14.66	113.8	-2.72	-15.11
108.1	-3.47	-14.80	111.0	-3.03	-14.57	113.9	-2.75	-15.18
108.2	-3.52	-14.66	111.1	-3.13	-14.68	114.0	-2.50	-15.03
108.3	-3.71	-14.92	111.2	-3.07	-14.62	114.1	-2.10	-14.99
108.4	-3.74	-14.83	111.3	-3.13	-14.67	114.2	-1.43	-14.82
108.5	-3.63	-14.90	111.4	-2.96	-14.46	114.3	-0.78	-14.64
108.6	-3.66	-14.89	111.5	-2.87	-14.54	114.4	-0.87	-14.67
108.7	-3.68	-14.91	111.6	-2.76	-14.51	114.5	-0.46	-14.59
108.8	-3.73	-14.98	111.7	-2.72	-14.58	114.6	-0.10	-14.51
108.9	-3.64	-14.89	111.8	-2.35	-14.40	114.7	-0.49	-14.62
109.0	-3.66	-14.98	111.9	-2.42	-14.47	114.8	-0.67	-14.66
109.1	-3.62	-14.93	112.0	-2.16	-14.32	114.9	-0.26	-14.50
109.2	-3.51	-14.92	112.1	-1.66	-14.25	115.0	-0.17	-14.59
109.3	-3.52	-14.89	112.2	-1.13	-13.94	115.1	-0.08	-14.49
109.4	-3.45	-14.83	112.3	-0.71	-13.81	115.2	-0.31	-14.44
109.5	-3.63	-14.98	112.4	-0.50	-13.75	115.3	-0.51	-14.46
109.6	-3.59	-14.87	112.5	-0.38	-13.66	115.4	-0.52	-14.45
109.7	-3.60	-14.85	112.6	-0.26	-13.62	115.5	-0.63	-14.43
109.8	-3.57	-14.88	112.7	-0.30	-13.62	115.6	-0.55	-14.50
109.9	-3.61	-14.86	112.8	-0.85	-13.91			
110.0	-3.58	-14.88	112.9	-0.90	-13.86			
110.1	-3.38	-14.79	113.0	-0.91	-13.93			
110.2	-3.47	-14.87	113.1	-1.35	-14.22			
110.3	-3.46	-14.85	113.2	-1.94	-14.57			
110.4	-3.31	-14.75	113.3	-2.00	-14.73			
110.5	-3.38	-14.79	113.4	-1.97	-14.85			

Table A.7: Stalagmite *H13*:

Depth [cm]	$\delta^{13}C$ [‰ PDB]	$\delta^{18}O$ [‰ PDB]	Depth [cm]	$\delta^{13}C$ [‰ PDB]	$\delta^{18}O$ [‰ PDB]	Depth [cm]	$\delta^{13}C$ [‰ PDB]	$\delta^{18}O$ [‰ PDB]
0	-7.39	-6.62	20.5	-7.90	-7.60	40.5	-4.30	-7.17
0.5	-6.22	-7.01	21	-7.59	-7.66	41	-3.69	-6.60
1	-3.78	-6.29	21.5	-6.27	-7.47	41.5	-4.92	-7.54
1.5	-4.37	-6.08	22	-4.82	-7.97	42	-4.90	-7.76
2	-6.58	-7.39	22.5	-5.82	-8.23	42.5	-4.78	-7.64
2.5	-8.69	-7.25	23	-6.24	-7.87	43	-3.54	-7.26
3	-7.76	-7.63	23.5	-6.57	-8.24	43.5	-5.01	-8.27
3.5	-8.06	-7.70	24	-3.33	-6.61	44	-3.52	-6.05
4	-7.89	-6.88	24.5	-5.39	-6.83	44.5	-3.94	-6.35
4.5	-8.89	-7.80	25	-4.66	-6.12	45	-4.12	-7.09
5	-6.82	-6.45	25.5	-4.03	-6.36	45.5	-3.33	-7.99
5.5	-4.08	-6.21	26	-4.35	-6.99	46	-2.99	-9.42
6	-6.41	-6.20	26.5	-4.14	-7.50	46.5	-3.39	-8.02
6.5	-7.44	-7.24	27	-3.86	-6.79	47	-3.00	-7.84
7	-7.00	-6.23	27.5	-4.56	-7.70	47.5	-2.56	-7.07
7.5	-7.66	-7.59	28	-5.16	-6.75	48	-3.59	-7.90
8	-8.44	-7.24	28.5	-5.29	-6.99	48.5	-4.04	-7.74
8.5	-7.34	-7.37	29	-4.84	-7.26	49	-5.96	-7.34
9.5	-7.83	-7.36	29.5	-6.51	-8.72	49.5	-5.60	-9.04
10	-6.91	-7.36	30	-6.23	-8.54	50	-5.82	-8.11
10.5	-8.03	-8.15	30.5	-3.18	-7.45	50.5	-5.22	-7.17
11	-7.98	-6.30	31	-2.38	-8.20	51	-5.91	-7.54
11.5	-7.20	-6.75	31.5	-1.22	-5.80	51.5	-5.93	-8.69
12	-6.60	-6.74	32	-3.27	-7.44	52	-5.95	-7.88
12.5	-1.56	-5.40	32.5	-1.95	-7.05	52.5	-5.66	-8.37
13	-0.37	-5.23	33	-4.01	-8.01	53	-1.94	-6.72
13.5	-1.70	-7.06	33.5	-4.01	-7.78	53.5	-1.41	-6.59
14	-0.81	-5.38	34	-4.04	-7.67	54	-3.79	-7.21
14.5	0.07	-5.72	34.5	-5.68	-8.69	54.5	-6.29	-8.93
15	-4.53	-6.92	35	-5.30	-8.99	55	-4.38	-7.44
15.5	-7.15	-8.22	35.5	-4.24	-8.97	55.5	-6.74	-7.87
16	-5.04	-7.36	36	-2.64	-7.25	56	-5.96	-7.80
16.5	-2.88	-5.11	36.5	-2.98	-6.53	56.5	-4.14	-7.04
17	-7.03	-6.06	37	-4.17	-6.59	57	-5.55	-8.56
17.5	-4.77	-5.50	37.5	-5.36	-7.72	57.5	-4.50	-8.98
18	-6.75	-7.20	38	-3.52	-6.72	58	-4.65	-8.24
18.5	-5.56	-6.28	38.5	-4.12	-6.54	58.5	-4.33	-6.86
19	-7.14	-8.16	39	-2.45	-7.19	59	-4.14	-7.77
19.5	-6.29	-7.66	39.5	-3.51	-7.04	59.5	-3.76	-7.33
20	-6.74	-6.76	40	-4.66	-7.55	60	-4.10	-6.62

Depth [cm]	$\delta^{13}C$ [‰ PDB]	$\delta^{18}O$ [‰ PDB]
60.5	-4.19	-7.40
61	-5.80	-8.29
61.5	-5.22	-7.88
62	-5.83	-8.88
62.5	-5.50	-7.84
63	-6.00	-9.32
63.5	-6.36	-8.28
64	-6.25	-8.22
64.5	-6.19	-6.92
65	-6.23	-7.87
65.5	-5.38	-7.12
66	-5.70	-7.47
66.5	-5.79	-8.26
67	-4.75	-6.53
67.5	-4.15	-8.38
68	-4.83	-6.60
68.5	-4.16	-7.21
69	-5.90	-8.23
69.5	-5.67	-7.65
70	-5.05	-8.41
70.5	-4.69	-8.24
71	-4.94	-8.43
71.5	-6.19	-7.73
72	-3.78	-9.09
72.5	-3.91	-7.97
73	-4.47	-7.72
73.5	-3.16	-7.61
74	-2.65	-7.40
74.5	-1.96	-6.55
75	-2.03	-6.53
75.5	-2.38	-6.92
76	-1.96	-8.34
76.5	-0.85	-5.75
77	-3.16	-7.92
77.5	-2.41	-6.56
78	-2.99	-6.67
78.5	-2.39	-7.05
79	-3.44	-7.53
79.5	-3.69	-7.57
80	-4.13	-7.78
80.5	-3.40	-7.77
81	-3.70	-7.39
81.5	-2.10	-6.92
82	-2.58	-7.21
82.5	-0.46	-7.40
83	-2.01	-7.25
83.5	-2.53	-8.07
84	-0.82	-7.06
84.5	-1.49	-8.97
85	-1.26	-6.90
85.5	-0.91	-7.12
86	-1.86	-7.07
86.5	-1.75	-7.91
87	-3.52	-8.64
87.5	-4.11	-8.17
88	-2.17	-7.46
88.5	-2.13	-7.28
89	-1.96	-7.85
89.5	-2.46	-8.37
90	-3.15	-9.96
90.5	-1.83	-9.16
91	-1.25	-9.12
91.5	-1.47	-8.42
92	0.37	-6.50
92.5	0.14	-7.45
93	0.14	-7.15
93.5	-1.27	-8.17
94	-1.47	-9.90
94.5	0.09	-7.11
95	-0.44	-8.28
95.5	-1.83	-8.74
96	-0.29	-8.33
96.5	0.45	-8.26
97	0.46	-7.78
97.5	0.71	-8.37
98	1.90	-6.62
98.5	1.52	-6.44
99	1.83	-7.26
99.5	0.83	-7.84
100	0.15	-9.00
100.5	0.89	-8.39
101	0.00	-8.59
101.5	1.13	-7.36
102	2.28	-7.18
102.5	0.52	-7.15
103	1.51	-6.00
103.5	0.74	-7.38
104	0.70	-8.50
104.5	1.21	-6.35
105	1.40	-7.37
105.5	1.71	-7.64
106	0.92	-7.62
106.5	1.10	-8.57
107	0.72	-9.17
107.5	0.55	-9.28
108	2.09	-7.74
108.5	2.10	-8.08
109	2.40	-7.86
109.5	1.61	-7.80
110	1.16	-8.67
110.5	1.38	-8.32
111	0.71	-8.98
111.5	1.21	-8.51
112	1.36	-8.04
112.5	1.37	-7.59
113	1.80	-8.05
113.5	2.50	-7.11
114	1.25	-7.31
114.5	0.63	-6.93
115	0.91	-7.27
115.5	0.97	-6.57
116	0.48	-7.58
116.5	0.28	-8.02
117	0.28	-7.79
117.5	0.24	-8.34
118	1.78	-7.22
118.5	0.37	-7.49
119	0.71	-8.97
119.5	1.20	-8.20
120	2.11	-6.16
120.5	-0.12	-8.18
121	1.31	-6.07
121.5	1.02	-7.31
122	1.56	-6.47
122.5	1.11	-8.14
123	0.08	-8.13
123.5	0.84	-7.31
124	2.27	-5.62
124.5	2.49	-6.94
125	1.17	-7.66
125.5	1.61	-7.15
126	2.33	-6.15
126.5	1.75	-7.47

Table A.8: Stalagmite *T1*:

Depth [cm]	$\delta^{13}C$ [‰ PDB]	$\delta^{18}O$ [‰ PDB]	Depth [cm]	$\delta^{13}C$ [‰ PDB]	$\delta^{18}O$ [‰ PDB]	Depth [cm]	$\delta^{13}C$ [‰ PDB]	$\delta^{18}O$ [‰ PDB]
0	-2.93	-6.24	41	-5.31	-10.25	81	-4.83	-10.29
1	-4.27	-8.60	42	-5.37	-10.22	82	-5.37	-10.72
2	-3.60	-9.12	43	-5.22	-10.15	83	-5.99	-11.00
3	-4.82	-9.47	44	-4.94	-9.94	84	-4.57	-10.17
4	-5.26	-9.89	45	-4.79	-9.95	85	-5.89	-10.44
5	-4.13	-9.45	46	-5.02	-9.94	86	-5.04	-10.12
6	-5.46	-9.75	47	-5.77	-10.01	87	-4.78	-9.84
7	-5.13	-9.75	48	-4.98	-9.85	88	-4.75	-10.20
8	-5.29	-10.04	49	-4.34	-9.52	89	-4.70	-10.25
9	-5.79	-10.17	50	-4.42	-9.77	90	-4.19	-10.12
10	-3.37	-9.27	51	-4.85	-10.11	91	-4.98	-10.42
11	-4.80	-9.89	52	-5.52	-10.06	92	-4.32	-10.03
12	-2.75	-8.89	53	-5.67	-10.07	93	-4.46	-10.13
13	-3.00	-9.20	54			94	-4.05	-9.90
14	-4.57	-9.81	55	-5.44	-10.00	95	-4.54	-10.38
15	-3.30	-9.15	56	-5.58	-10.06	96	-2.56	-9.42
16	-3.17	-8.99	57	-4.76	-9.78	97	-4.93	-10.64
17	-3.25	-9.33	58	-5.70	-10.21	98	-3.82	-9.67
18	-4.64	-9.65	59	-5.56	-10.49	99	-3.89	-9.83
19	-4.85	-9.82	60	-4.08	-9.56	100	-4.93	-10.31
20	-5.32	-10.00	61	-5.10	-9.91	101	-4.89	-10.25
21	-5.09	-9.92	62	-5.48	-10.11	102	-4.90	-10.39
22	-4.88	-10.03	63	-4.36	-9.48	103	-4.76	-10.19
23	-4.95	-10.03	64	-5.42	-9.71	104	-4.55	-10.05
24	-5.03	-10.27	65	-5.03	-9.66	105	-4.38	-10.33
25	-5.13	-10.15	66	-5.18	-9.82	106	-4.47	-10.44
26	-4.89	-10.02	67	-5.71	-10.52	107	-4.43	-10.36
27	-5.16	-10.47	68	-5.49	-10.31	108	-4.54	-10.45
28	-5.48	-10.62	69	-5.51	-10.22	109	-4.82	-10.40
29	-5.00	-10.42	70	-5.60	-10.18	110	-4.38	-10.12
30	-5.02	-10.35	71	-5.62	-10.24	111	-3.64	-9.94
31	-5.26	-10.47	72	-5.24	-10.41	112	-3.66	-10.05
32	-5.32	-10.54	73	-5.08	-10.31	113	-3.83	-10.20
33	-5.77	-10.81	74	-4.77	-10.23	114	-5.13	-10.99
34	-5.36	-10.66	75	-4.80	-10.23	115	-5.01	-11.08
35	-5.27	-10.24	76	-4.85	-10.13	116	-5.36	-11.02
36	-5.43	-10.40	77	-5.23	-10.48	117	-4.79	-10.89
37	-5.18	-10.24	78	-5.36	-10.58	118	-4.94	-10.94
38	-5.30	-10.31	79	-5.54	-10.59	119	-4.98	-10.95
40	-4.90	-10.08	80	-4.40	-10.31	120	-4.20	-10.61

References

Atkinson, T.C. (1977): Carbon dioxide in the atmosphere of the unsaturated zone: an important control of ground water hardness in limestones. - *Journal of Hydrology*, **35**: 111-123.

Atkinson, T.C. (1983): Growth mechanisms of speleothems in Castleguard Cave, Columbia Icefields, Alberta, Canada. - *Arctic and Alpine Research*, **15**: 523-536.

Baker, A., Ito, E., Smart, P.L. and McEwan, R.F. (1997): Elevated and variable values of ^{13}C in speleothems in a British cave system. - *Chemical Geology*, **136**: 263-270.

Bard, E., Antonioli, F. and Silenzi, S. (2002): Sea-level during the penultimate interglacial period based on a submerged stalagmite from Argentarola Cave (Italy). - *Earth and Planetary Science Letters*, **6096**: 1-12.

Beck, W.J., Richards, D.A., Edwards, R.L., Silverman, B.W., Smart, P.L., Donahue, D.J., Hererra-Osterheld, S., Burr, G.S., Calsoyas, L., Jull, T.A.J. and Biddulph, D. (2001): Extremely large variations of atmospheric 14C concentration during the last glacial period. - *Science*, **292**: 2453-2457.

Blunier, T. and Brook, E.J. (2001): Timing of millenial-scale climate change in Antarctica and Greenland during the last glacial period. - *Science*, **291**: 109-112.

Boettger, T., Junge, F.W. and Litt, T. (2000): Stable climatic conditions in central Germany during the Last Interglacial. - *Journal of Quaternary Science*, **15**: 469-473.

Bond, G., Kromer, B., Beer, J., Muscheler, R., Evans, M.N., Showers, W., Hoffman, S., Lotti-Bond, R., Hajdas, I. and Bonani, G. (2001): Persistent solar influence on North Atlantic climate during the Holocene. - *Science*, **294**: 1-6.

Bond, G., Showers, W., Cheseby, M., Lotti-Bond, R., Almasi, P., deMenocal, P., Priore, P., Cullen, H., Hajdas, I. and Bonani, G. (1997): A pervasive millenial-scale cycle in North Atlantic Holocene and glacial climates. - *Science*, **278**: 1257-1266.

Brook, G.A., Embabi, N.S., Ashour, M.M., Edwards, R.L., Cheng, H., Cowart, J.B. and Dabous, A.A. (2002): Djara Cave in the Western Desert of Egypt: morphology and evidence of Quaternary climatic change. - *Cave and Karst Science*, **29**: 57-66.

Burns, S.J., Fleitmann, D., Matter, A., Neff, U. and Mangini, A. (2001): Speleothem evidence from Oman for continental pluvial events during interglacial periods. - *Geology*, **29**: 623-626.

Burns, S.J., Matter, A., Frank, N. and Mangini, A. (1998): Speleothem-based paleoclimate record from northern Oman. - *Geology*, **26**: 499-502.

Carslaw, K.S., Harrison, R.G. and Kirkby, J. (2002): Cosmic rays, clouds, and climate. - *Science*, **298**: 1732-1737.

Cheng, H., Edwards, R.L., Hoff, J., Gallup, C.D., Richards, D.A. and Asmeron, Y. (2000): The half-lives of ^{234}U and ^{230}Th. - *Chemical Geology*, **169**: 17-33.

Christl, M., Mangini, A., Holzkämper, S. and Spötl, C. (in press): Evidence for a link between the flux of galactic cosmic rays and Earth's climate during the past 200,000 years. - *Journal of Atmospheric and Solar-Terrestrial Physics*,

Clemens, S.C., Murray, D.W. and Prell, W.L. (1996): Nonstationary phase of the Plio-Pleistocene Asian Monsoon. - *Science*, **274**: 943-948.

Dennis, P.F., Rowe, P.J. and Atkinson, T.C. (2001): The recovery and isotopic measurement of water from fluid inclusions in speleothems. - *Geochimica et cosmochimica acta*, **65**: 871-884.

Dreybrodt, W. (1980): Deposition of calcite from thin films of natural calcareous solutions and the growth of speleothems. - *Chemical Geology*, **29**: 89-105.

Dreybrodt, W. (1982): A possible mechanism for growth of calcite speleothems without participation of biogenic carbon dioxide. - *Earth and Planetary Science Letters*, **58**: 293-299.

Dulinski, M. and Rozanski, K. (1990): Formation of $^{13}C/^{12}C$ isotope ratios in speleothems: a semi-dynamic model. - *Radiocarbon*, **32**: 7-16.

Esat, T.M., McCulloch, M.T., Chappell, J., Pillans, B. and Omura, A. (1999): Rapid fluctuations in sea level recorded at Huon Peninsula during the penultimate deglaciation. - *Science*, **283**: 197-201.

Fairchild, I.J., Borsato, A., Tooth, A.F., Frisia, S., Hawkesworth, C.J., Huang, Y., McDermott, F. and Spiro, B. (2000): Controls on trace element Sr-Mg composition of carbonate cave waters: implications for speleothem climatic records. - *Chemical geology*, **166**: 255-269.

Fantidis, J. and Ehhalt, D.H. (1970): Variations of the carbon and oxygen isotopic composition in stalagmites and stalactites: evidence of non-equilibrium isotopic fractionation. - *Earth and Planetary Science Letters*, **10**: 136-144.

Florineth, D. and Schlüchter, C. (2000): Alpine evidence for atmospheric circulation patterns in Europe during the Last Glacial Maximum. - *Quaternary Research*, **54**: 295-308.

Ford, D.C. and Williams, P. (1989): Karst Geomorphology and Hydrology. Unwin Hyman Ltd., London.

Frank, N. (1997): Anwendung der Thermionen-Massenspektrometrie zur Uranreihen-Datierung pleistozäner, mitteleuropäischer Travertinvorkommen. PhD-thesis, Heidelberg Academy of Sciences.

Frank, N., Braun, M., Hambach, U., Mangini, A. and Wagner, G. (2000): Warm period growth of travertine during the Last Interglaciation in southern Germany. - *Quaternary Research*, **54**: 38-48.

Friedman, I., O´Neil, J.R. and Fleischer, M. (1977): Compilation of stable isotope fractionation factors of geochemical interest. - *U. S. Geological Survey Professional Paper*, **P 0440-KK**: 12pp.

Frogley, M.R., Tzedakis, P.C. and Heaton, T.H.E. (1999): Climate variability in northwest Greece during the Last Interglacial. - *Science*, **285**: 1886-1888.

Fronval, T. and Jansen, E. (1996): Rapid changes in ocean circulation and heat flux in the nordic seas during the Last Interglacial period. - *Nature*, **383**: 806-810.

Gallup, C.D., Cheng, H., Taylor, F.W. and Edwards, R.L. (2002): Direct determination of the timing of sea level change during Termination II. - *Science*, **295**: 310-313.

Genty, D., Diot, M.-F. and O'Yl, W. (2001): Sources of pollen in stalactite drip water in two caves in southwest France. - *Cave and Karst Science*, **28**: 59-66.

Grootes, P.M. and Stuiver, M. (1997): Oxygen 18/16 variability in Greenland snow and ice with 10^{-3} to 10^{5}-year time resolution. - *Journal of Geophysical Research*, **102**: 26,455-26,470.

Harmon, R.S., Schwarcz, H.P. and O´Neil, J.R. (1979): D/H ratios in speleothem fluid inclusions: a guide to variations in the isotopic composition of meteoric precipitation? - *Earth and Planetary Science Letters*, **42**: 254-266.

Hearty, P.J. and Neumann, A.C. (2001): Rapid sea level and climate change at the close of the Last Interglaciation (MIS 5e): evidence from the Bahama Islands. - *Quaternary Science Reviews*, **20**: 1881-1895.

Henderson, G.M. and Slowey, N.C. (2000): Evidence from U-Th dating against northern hemisphere forcing of the penultimate deglaciation. - *Nature*, **404**: 61-66.

Hendy, C.H. (1971): The isotopic geochemistry of speleothems - I. The calculation of the effects of different modes of formation on the isotopic composition of speleothems and their applicability as palaeoclimatic indicators. - *Geochimica et Cosmochimica Acta*, **35**: 801-824.

Hill, C.A. and Forti, P. (1986): Cave minerals of the world. Nat. Speleo. Soc., Huntsville, USA.

Holzkämper, S., Mangini, A., Spötl, C. and Mudelsee, M. (submitted): Timing and progression of the Last Interglacial derived from high Alpine speleothems. -

Imbrie, J., Hays, J.D., McIntyre, A., Mix, A.C., Morley, J.J., Pisias, N.G., Prell, W.L. and Shackleton, N.J. (1984): The orbital theory of Pleistocene climate: Support from a revised chronology of the marine $\delta^{18}O$ record. 269-305. In: Milankovitch and Climate. Reidel, Boston.

Ivanovich, M. and Harmon, R.S. (1992): Uranium-series Disequilibrium: Applications to Earth, Marine, and Environmental Sciences. Clarendon Press, Oxford.

Johnsen, S., Dahl-Jensen, D., Gundestrup, N.S., Steffensen, J.P., Clausen, H.B., Miller, H., Masson-Delmotte, V., Sveinbjörnsdottir, A.E. and White, J. (2001): Oxygen isotope and palaeotemperature records from six Greenland ice-core stations: Camp Century, Dye-3, GRIP, GISP2, Renland and NorthGRIP. - *Journal of Quaternary Science*, **16**: 299-307.

Kandiano, E.S., Bauch, H.A. and Müller, A. (in press): Sea surface temperature variability in the North Atlantic during the last two glacial-interglacial cycles: comparison of faunal, oxygen isotopic, and Mg/Ca-derived records. - *Palaeogeography, Palaeoclimatology, Palaeoecology*,

Kukla, G.J. (2000): The last interglacial. - *Science*, **287**: 987-988.

Kukla, G.J. (2002): Last Interglacial Climates. - *Quaternary Research*, **58**: 2-13.

Lambeck, K. and Chappell, J. (2001): Sea Level Change Through the Last Glacial Cycle. - *Science*, **292**: 679-686.

Lambeck, K., Esat, T.M. and Potter, E.-K. (2002): Links between climate and sea levels for the past three million years. - *Nature*, **419**: 199-206.

Lauritzen, S.E. and Lundberg, J. (1999): Speleothems and climate: a special issue of the holocene. - *The holocene*, **9**: 643-647.

Lea, D.W. (2001): Ice ages, the California Current, and Devils Hole. - *Science*, **293**: 59-60.

Linge, H., Lauritzen, S.-E. and Lundberg, J. (2001): Stable isotope stratigraphy of a late last interglacial speleothem from Rana, Northern Norway. - *Quaternary Research*, **56**: 155-164.

Linsley, B.K. (1996): Oxygen-isotope record of sea level and climate variations in the Sulu Sea over the past 150,000 years. - *Nature*, **380**: 234-237.

Martinson, D.G., Pisias, N.G., Hays, J.D., Imbrie, J., Moore, T.C., Jr. and Shackleton, N.J. (1987): Age dating and the orbital theory of the ice ages; development of a high-resolution 0 to 300,000-year chronostratigraphy. - *Quaternary Research*, **27**: 1-29.

Maslin, M.M. and Tzedakis, P.C. (1996): Sultry Last Interglacial gets sudden chill. - *EOS*, **77**: 353-354.

McDermott, F., Mattey, D.P. and Hawkesworth, C.J. (2001): Centennial-scale Holocene climate variability revealed by a high-resolution speleothem $\delta^{18}O$ record from SW Ireland. - *Science*, **294**: 1328-1331.

McManus, J.F., Bond, G., Broecker, W.S., Johnsen, S., Labeyrie, L. and Higgins, S. (1994): High-resolution climate records from the North Atlantic during the last interglacial. - *Nature*, **371**: 326-329.

Milankovitch, M. (1941): Kanon der Erdbestrahlung und seine Anwendung auf das Eiszeitenproblem. Königlich Serbische Akademie, Belgrad.

Mook, W.G. (1994): Principles of Isotope Hydrology. University of Groningen, Amsterdam.

Neff, U. (2001): Massenspektrometrische Th/U-Datierung von Höhlensintern aus dem Oman: Klimaarchive des asiatischen Monsuns. PhD thesis, Heidelberg Academy of Sciences.

Neff, U., Burns, S.J., Mangini, A., Mudelsee, M., Fleitmann, D. and Matter, A. (2001): Strong coherence between solar variability and the monsoon in oman between 9 and 6 kyr ago. - *Nature*, **411**: 290-293.

Niggemann, S., Mangini, A., Mudelsee, M., Richter, D.K. and Wurth, G. (2003): Sub-Milankovitch climatic cycles in Holocene stalagmites from Sauerland, Germany. - *Earth and Planetary Science Letters*, **216**: 539-547.

Niggemann, S., Mangini, A., Richter, D.K. and Wurth, G. (2002): A paleoclimate record of the last 17,600 years in stalagmites from the B7-cave, Sauerland, Germany. - *Quaternary Science Reviews*, **22**: 555-567.

O´Neil, J.R., Clayton, R.N. and Mayeda, T.K. (1969): Oxygen Isotope Fractionation in Divalent Metal Carbonates. - *The Journal of Chemical Physics*, **51**: 5547-5558.

Overpeck, J., Anderson, D., Trumbore, S. and Prell, W. (1996): The southwest Indian Monsoon over the last 18000 years. - *Climate Dynamics*, **12**: 213-225.

Petit, J.R., Jouzel, J., Raynaud, D., Barkov, N.I., Barnola, J.-M., Basile, I., Bender, M., Chappellaz, J., Davis, M., Delaygue, G., Delmotte, M., V.M., K., Legrand, M., Lipenkov, V.Y., Lorius, C., Pepin, L., Ritz, C., Saltzman, E. and Stievenard, M. (1999): Climate and atmospheric history of the past 420,000 years from the vostok ice core, antarctica. - *Nature*, **399**: 429-436.

Priestley, M.B. (1981): Spectral Analysis and Time Series. Academic Press, London.

Rahmstorf, S. (2002): Ocean circulation and climate during the past 120,000 years. - *Nature*, **419**: 207-214.

Rahmstorf, S. (2003): Timing of abrupt climate change: a precise clock. - *Geophysical Research Letters*, **30**: 1510, doi: 10.1029/2003GL017115.

Ram, M. and Stolz, M.R. (1999): Possible solar influences on the dust profile of the GISP2 ice core from Central Greenland. - *Geophysical Research Letters*, **26**: 1043-1046.

Richards, D.A. and Dorale, J.A. (2003): Uranium-series chronology and environmental applications of speleothems. 407-460. In: Uranium-series geochemistry. The Mineralogical Society of America, Washington D.C.

Richards, D.A., Smart, P.L. and Edwards, R.L. (1994): Maximum sea levels for the last glacial period from U-series ages of submerged speleothems. - *Nature*, **367**: 357-360.

Rind, D. (2002): The Sun´s role in climate variations. - *Science*, **296**: 673-677.

Rioual, P., Andrieu-Ponel, V., Rietti-Shati, M., Battarbee, R.W., de Beaulieu, J.-L., Cheddadi, R., Reille, M., Svobodova, H. and Shemesh, A. (2001): High-resolution record of climate stability in France during the Last Interglacial period. - *Nature*, **413**: 293-296.

Roberts, M.S., Smart, P.L. and Baker, A. (1998): Annual trace element variations in a Holocene speleothem. - *Earth and Planetary Science Letters*, **154**: 237-246.

Robinson, L.F., Henderson, G.M. and Slowey, N.C. (2002): U-Th dating of marine isotope stage 7 in Bahamas slope sediments. - *Earth and Planetary Science Letters*, **6104**: 1-13.

Rozanski, K., Araguas-Araguas, L. and Gonfiantini, R. (1993): Isotopic patterns in modern global precipitation. - *in Climate Change in Continental Isotopic Records, Geophys. Monogr. Ser.*, **78**: 1-36.

Sanchez-Goni, M.F., Eynaud, F., Turon, J.L. and Shackleton, N.J. (1999): High resolution palynological record off the Iberian margin: direct land-sea correlation for the Last Interglacial complex. - *Earth and Planetary Science Letters*, **171**: 123-137.

Schulz, M., Berger, W.H., Sarnthein, M. and Grootes, P.M. (1999): Amplitude variations of 1470-year climate oscillations during the last 100,000 years linked to fluctuations of continental ice mass. - *Geophysical Research Letters*, **26**: 3385-3388.

Schulz, M. and Mudelsee, M. (2002): REDFIT: estimating red-noise spectra directly from unevenly spaced paleoclimatic time series. - *Computers & Geosciences*, **28**: 421-426.

Schulz, M. and Stattegger, K. (1997): SPECTRUM: spectral analysis of unevenly spaced paleoclimatic time series. - *Computers & Geosciences*, **23**: 929-945.

Schwarcz, H.P. (1986): Geochronology and isotopic geochemistry of speleothems. 271-303. In: Handbook of environmental isotope geochemistry. Elsevier, Amsterdam.

Shackleton, N.J. (2000): The 100,000-year ice-age cycle identified and found to lag temperature, carbon dioxide, and orbital eccentricity. - *Science*, **289**: 1897-1902.

Shackleton, N.J., Chapman, M., Sanchez-Goni, M.F., Pailler, D. and Lancelot, Y. (2002): The classic marine isotope substage 5e. - *Quaternary Research*, **58**: 14-16.

Shackleton, N.J., Ludwig, K.R., Simmons, K.R., Winograd, I.J., Szabo, B.J., Landwehr, J.M. and Riggs, A.C. (1993): Last interglacial in Devils Hole. - *Nature*, **362**: 596.

Shackleton, N.J. and Opdyke, N.D. (1973): Oxygen isotope and paleomagnetic stratigraphy of equatorial Pacific core V28-238: oxygen isotope temperatures and ice volumes on a 105 and 106 year scale. - *Quaternary Research*, **3**: 39-55.

Shackleton, N.J., Sanchez-Goni, M.F., Pailler, D. and Lancelot, Y. (2003): Marine Isotope Substage 5e and the Eemian Interglacial. - *Global and Planetary Change*, **36**: 151-155.

Shopov, Y.Y., Ford, D.C. and Schwarcz, H.P. (1994): Luminescent micro-banding in speleothems: high-resolution chronology and paleoclimate. - *Geology*, **22**: 407-410.

Spötl, C. and Mangini, A. (2002): Stalagmite from the Austrian Alps reveals Dansgaard-Oeschger events during isotope stage 3: Implications for the absolute chronology of Greenland ice cores. - *Earth and Planetary Science Letters*, **203**: 507-518.

Spötl, C., Mangini, A., Burns, S.J., Frank, N. and Pavuza, R. (in press): Speleothems from the high-Alpine Spannagel Cave, Zillertal Alps (Austria). Kluwer, Dordrecht.

Spötl, C., Mangini, A., Frank, N., Eichstädter, R. and Burns, S.J. (2002): Start of the Last Interglacial period at 135 ka: Evidence from a high Alpine speleothem. - *Geology*, **30**: 815-818.

Stirling, C.H., Esat, T.M., Lambeck, K. and McCulloch, M.T. (1998): Timing and duration of the Last Interglacial: evidence for a restricted interval of widespread coral reef growth. - *Earth and Planetary Science Letters*, **160**: 745-762.

Stirling, C.H., Esat, T.M., McCulloch, M.T. and Lambeck, K. (1995): High-precision U-series dating of corals from western Australia and implications for the timing and duration of the Last Interglacial. - *Earth and Planetary Science Letters*, **135**: 115-130.

Stuiver, M. and Braziunas, T.F. (1993): Sun, ocean, climate and atmospheric $^{14}CO_2$; an evaluation of causal and spectral relationships. - *The Holocene*, **3**: 289-305.

Thouveny, N., de Beaulieu, J.-L., Bonifay, E., Creer, K.M., Guiot, J., Icole, M., Johnsen, S., Jouzel, J., Reille, M., Williams, T. and Williamson, D. (1994): Climate variations in Europe over the past 140 kyr deduced from rock magnetism. - *Nature*, **371**: 503-506.

Turner, C. (2002): Problems of the duration of the Eemian Interglacial in Europe North of the Alps. - *Quaternary Research*, **58**: 45-48.

Turner, C. and West, R.G. (1968): The subdivision and zonation of interglacial periods. - *Eiszeitalter und Gegenwart*, **19**: 93-101.

Wedepohl, H.K. (1995): The composition of the continental crust. - *Geochimica et Cosmochimica Acta*, **59**: 1217-1232.

Weyhenmeyer, C.E., Burns, S.J., Waber, N.H., Aeschbach-Hertig, W., Kipfer, R., Loosli, H.H. and Matter, A. (2000): Cool Glacial Temperatures and Changes in Moisture Source recorded in Oman Groundwaters. - *Science*, **287**: 842-845.

Wilson, M.A., Curran, H.A. and White, B. (1998): Paleontological evidence of a brief global sea-level event during the Last Interglacial. - *Lethaia*, **31**: 241-250.

Winograd, I.J., Coplen, T.B., Landwehr, J.M., Riggs, A.C., Ludwig, K.R., Szabo, B.J., Kolesar, P.T. and Revesz, K.M. (1992): Continuous 500,000-year climate record from vein calcite in Devils Hole, Nevada. - *Science*, **258**: 255-259.

Winograd, I.J., Landwehr, J.M., Ludwig, K.R., Coplen, T.B. and Riggs, A.C. (1997): Duration and structure of the past four interglaciations. - *Quaternary Science Reviews*, **48**: 141-154.

Acknowledgment

This work has been supported by many people from various departments, and its accomplishment would not have been possible without their help.

First of all I want to thank my supervisor PROF. DR. A. MANGINI. His office's door has always been open, and his confidence in his ideas and my data (or the other way around) has been very fruitful. I can also recommend him for camel–trophies and bike races!

Thanks to PROF. DR. W. AESCHBACH-HERTIG, who jumped in as the second supervisor. I had no doubt that he would be very suitable for and interested in my work's topic.

Special thanks goes to PROF. DR. C. SPÖTL. He provided the extraordinary samples from *Spannagel Cave*, excellent stable isotope profiles, and quick responses to all questions I had. The "expedition" to his living room, the *Spannagel Cave*, has been one of the highlights of my PhD.

Furthermore I thank PROF. DR. DR. H.-P. UERPMANN and his family for the unforgettable time that I had in the United Arab Emirates. It was very informative and also pleasant. Sorry, that I couldn't find any Holocene samples (yet)!

PROF. DR. H.J. PACHUR organized and guided our desert–expedition to Egypt in 2003. His great experience and interesting tales made this trip to an exciting, but safe adventure.

DR. M. MUDELSEE, the „Spectral–Man". Thanks for all the gorgious spectral analyses you have made! They developed to a major contribution to my work.

A big compliment goes to the "Paleos" – it was a great working group to work and to live with, and I hope that we'll keep contact… No room to note and thank them all, but a special thank goes to my DEKLIM–colleague DENIS SCHOLZ ("Scholzkämper") – how often he had to listen to my tales and to cheer them by uncountable drinks??? Strong emphasis also for RENE EICHSTÄDTER, who introduced me into the secrets of TIMS–measurements in his very own way, and who always remembered me, when it was 12 o'clock ("Geh' ma?") – Thank you! Furthermore I want to thank (British!) PETYA BLUMBACH for improving some parts of the manuscript's (American!) English.

At last I want to thank my family, who accompanied and supported my studies in both financial and mental respect.